# The Evaporation and Aerosol Formation Mechanism of Solutes in Molten Metals

by

José Benavides

B.S., Mechanical Engineering (1994)
The University of Texas at Austin

Submitted to the Department of Materials Science and Engineering
in partial fulfillment of the requirements for the Degree of Master of Science
in Materials Science and Engineering

at the

Massachusetts Institute of Technology

September 1997

Signature of Author ..............................................................................
Department of Materials Science and Engineering
August 8, 1997

Certified by ..............................................................................
Merton C. Flemings
Toyota Professor of Materials Science and Engineering
Thesis Supervisor

Accepted by ..............................................................................
Linn W. Hobbs
John F. Elliott Professor of Materials
Chair, Departmental Committee on Graduate Students

# The Evaporation and Aerosol Formation Mechanism of Solutes in Molten Metals

by

José Benavides

Submitted to the Department of Materials Science and Engineering on August 8, 1997
in partial fulfillment of the requirements for the Degree of Master of Science
in Materials Science and Engineering

## ABSTRACT

Experiments to determine the evaporation rates and aerosol formation mechanisms of several solutes in molten copper at atmospheric pressure have been carried out. 1 wt % or less of an impurity (Cd, Zn, and Bi) was added to molten copper at 1200 °C and allowed to evaporate while bubbling 0.75 and 1.5 L/min of argon through the melt. Samples of the melt and of the resulting aerosol were periodically taken and analyzed to determine their impurity content and particle size distribution, respectively.

A theoretical model to predict the evaporation rates of solutes from molten metals was developed and compared to the experimental results. Evaporation into the gas bubbles and through the melt surface were modelled separately. The results indicate that the solutes evaporate with first order kinetics and their concentrations in the melt decrease exponentially with time. For the conditions tested, it was found that equilibrium is achieved in the bubbles for all the solutes considered in molten copper. Excellent correlation between experiment and theory was found in the case of cadmium at both flow rates. The model has been extended to other solutes and also to molten Fe-3%C at 1600 °C as a solvent.

A theoretical prediction of the final diameter of average mass of cadmium aerosols was developed and compared to the experimental findings. The formation of cadmium aerosols evaporating from molten copper is believed to occur by nucleation and subsequent coagulation. Some cadmium also coagulates with large copper particles formed as a result of bubble breakage at the melt surface. As the concentration of cadmium in the melt decreases, there is less evaporating cadmium available to nucleate and coagulate, so the diameter of average mass of the aerosol decreases.

Thesis Supervisor: Merton C. Flemings
Title: Toyota Professor of Materials Science and Engineering

## Table of Contents

# List of Figures

# List of Tables

## Acknowledgments

I would like to thank Dr. Gokhan Senel for his invaluable support and collaboration throughout the whole project.

I have to acknowledge the Idaho National Engineering and Environmental Laboratory (INEEL) for their financial support of the project. Thanks also to Molten Metal Technology (MMT) for their advice in the initial stages and their help with materials.

I would also like to express my gratitude to Prof. M. Flemings for allowing me to work on this project which I found very interesting and which I'm sure will help me in my career, and for his valuable input. Similarly I want to acknowledge Professors A. Sarofim and J. Tester for their helpful advice in all the project.

Many thanks to all of Prof. Flemings's research group (Doug, John, Anacleto, Yusuf, Ittipon, Matthieu, and all the others) for all your help, and also to Chris, Prof. Kattamis, Prof. Pal, and last but not least, Miguelito.

## 1. INTRODUCTION

Wastes are highly variable in composition and physical state. Specifically, Department of Energy (DOE) wastes present special challenges to processing because they are heterogeneous and contain volatile organics, hazardous metals (particularly Pb and Hg) and radionuclides (Pt, Ce, St, Te, Cs, and lanthanides). As an example of the heterogeneity of the DOE mixed wastes, one estimate characterized them as containing 28% inorganic sludge, 13% soil/dirt, 9% bulk metals, 7% cemented inorganic sludge, 7% lead shielding, 6% plastics, 5% organic sludge, 5% paper, 3% cemented organic sludge, 3% glass, 2% uranium compounds, and 1% beryllium.

An integrated thermal treatment study by Feizollahi et. al. [1] on the evaluation of the applicability of various technologies to DOE wastes suggested that molten metal processing has the greatest applicability with the lowest overall projected life cycle costs. The use of molten metal processing of mixed wastes has the advantages of destroying organic hazardous components and the partitioning of the inorganic residue between metal, ceramic, and aerosol phases. The variation of the temperature and composition of the metal and ceramic phases permits a wide range of latitude in the distribution of toxic metals such as lead and radionuclides. The objectives are to maximize the volume reduction of the disposal waste, to recycle the elements of value, and to reduce the concentrations of toxic contaminants in the bulk residues to the point that they can be delisted.

In molten metal processing, a waste stream is injected into a bath of molten metal

(Figure 1). Inorganic components of the waste are partitioned between the metal, ceramic, and gas phases. An inert gas (in this case argon) is bubbled through the bath to facilitate the mass transfer from metal to gas phases and to agitate the melt.

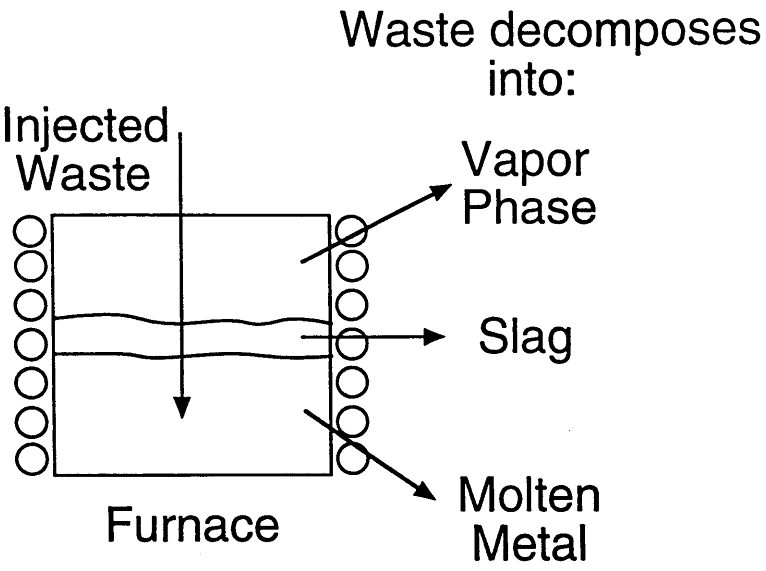

Figure 1. Partitioning of wastes in molten metal processing.

In order to develop an improved understanding of the partitioning of the inorganic residue between the different phases, the transfer of metallic impurities from the metal to the gas phase and the mechanism of formation of the aerosol produced during processing will be investigated.

Many studies about the removal of impurities from molten metals have been done, although most involve gaseous instead of metallic impurities, gas impinging instead of bubbling, and/or vacuum conditions instead of atmospheric pressure. A good overview of vacuum refining of copper is given by Ozberk and Guthrie [2]. A variety of impurities such as As, Bi, Pb, S, and O are covered, and gas phase mass transfer is found to dominate the kinetics of the process except at very low pressures. Ohno [3] has also written several papers on the vacuum refining of copper. There are several other studies regarding evaporation of impurities from steel under vacuum. For example, Ward and Aurini [4] found that at high temperatures (above 1430 °C) liquid phase mass transfer controls the removal of Mn, while at lower temperatures surface evaporation becomes dominant. In another study, Ward [5] concluded that, as in liquid copper, gas phase mass transfer dominates the evaporation of Mn from steel except for very low pressures, where liquid phase mass transfer and surface evaporation become important. In general, these studies agree that the vaporization of metallic impurities follows first-order kinetics with respect to their percentage in the melt.

Other studies have been done by impinging inert gas or plasma jets on the liquid metal surface [6, 7, 8]. In the case of Zn evaporating from molten steel or copper, Ito, et. al. [6], and Hino, et. al. [8], found that the controlling mechanism was Zn diffusion in the bulk liquid metal.

At a more fundamental level, a review paper by Richardson [9] explores the kinetics of reactions between gases and liquid metals.

## 2. EXPERIMENTAL WORK

### 2.1. Experimental Setup

The experimental setup mainly consists of a 10-pound capacity induction furnace and a 20 kW power supply unit. There is also a sampling probe and a cascade impactor.

A temperature control unit, mass flow meter, vacuum pump, and argon and nitrogen lines complete the system. A photograph and a schematic diagram of the setup are shown in Figures 2 and 3.

The induction furnace consists of a heating coil, containment crucible, graphite susceptor, main crucible, and several fittings and joints on the top and bottom plates (Figure 4). A quartz cylinder placed between the coil and the containment crucible is used to seal the system. The graphite susceptor outside the main crucible reduces the excessive inductive stirring effect. Argon gas is injected through a submerged lance at a flow rate varying between 0.75 to 1.5 L/min. The temperature of the furnace is controlled and monitored via two K-type thermocouples. One is dipped into the molten metal and the other is inserted into a hole drilled in the graphite susceptor.

The offgases are condensed in the sample collection probe with 27 L/min of nitrogen quench gas and 3 L/min of additional nitrogen injected radially through a porous sintered tube to avoid particle deposition on the walls of the probe. The condensed particles are then size-segregated from >18 μm down to 0.016 μm in a Micro-Orifice Uniform Deposit (MOUDI) cascade impactor.

## 2.2. Evaporation Experiments

Several evaporation experiments were carried out. A single 1/4" O.D. orifice lance was used to bubble argon through the molten metal in all of these experiments, because of availability, practicality, and to limit bubble coalescence. In these runs, 1 wt % of an impurity was dropped into a molten copper bath and allowed to evaporate, while samples

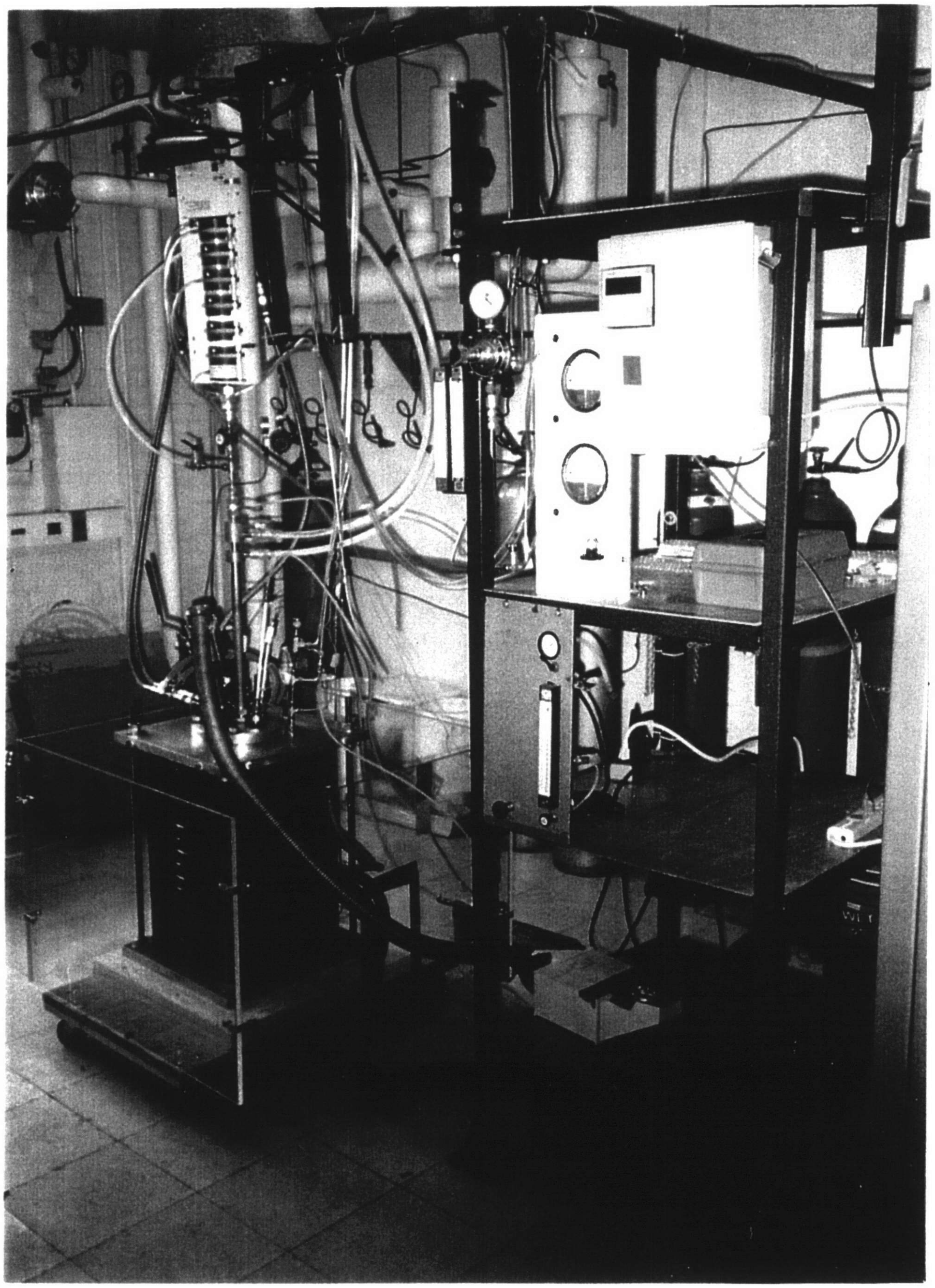

Figure 2. Photograph of the experimental setup.

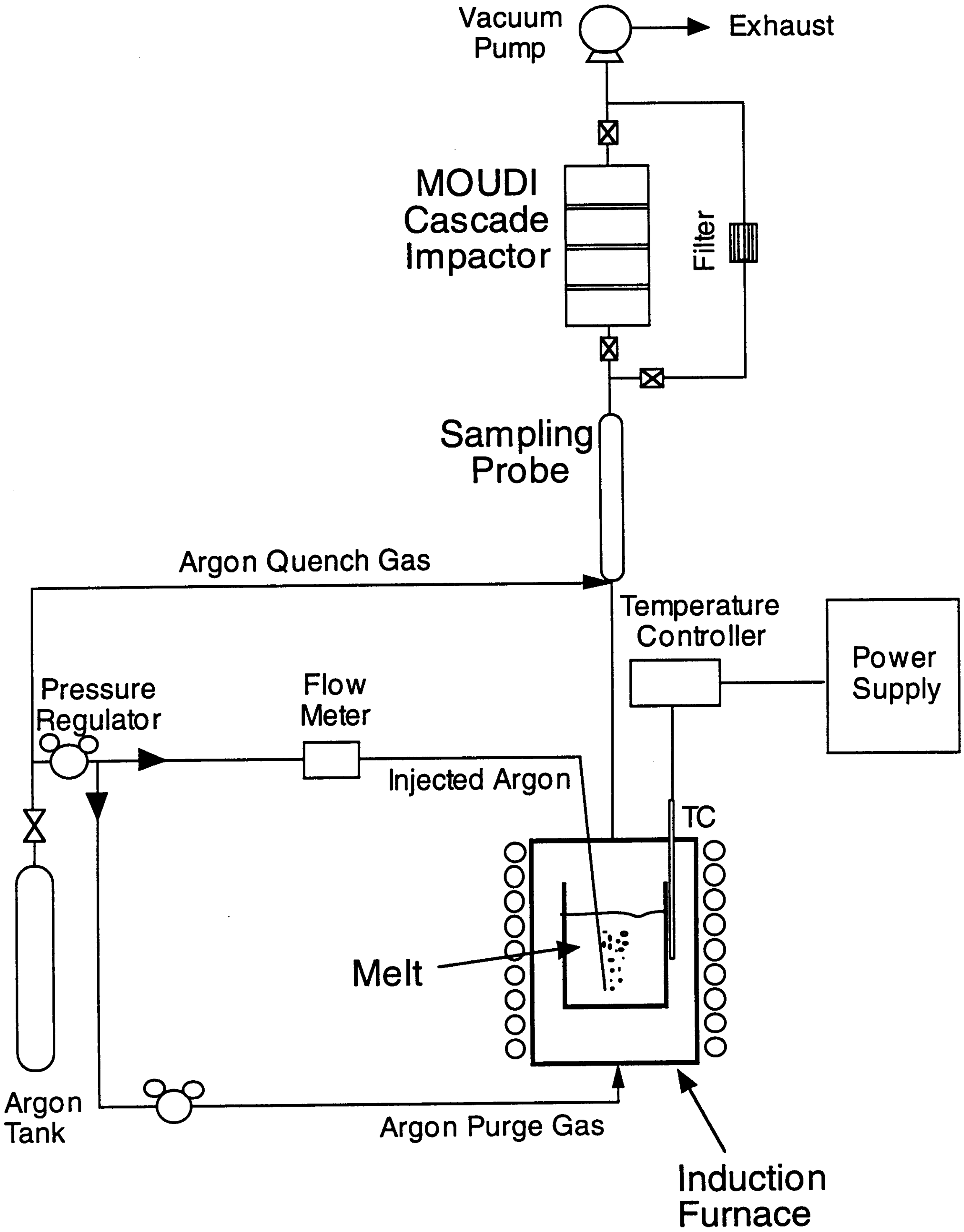

Figure 3. Schematic diagram of the experimental setup.

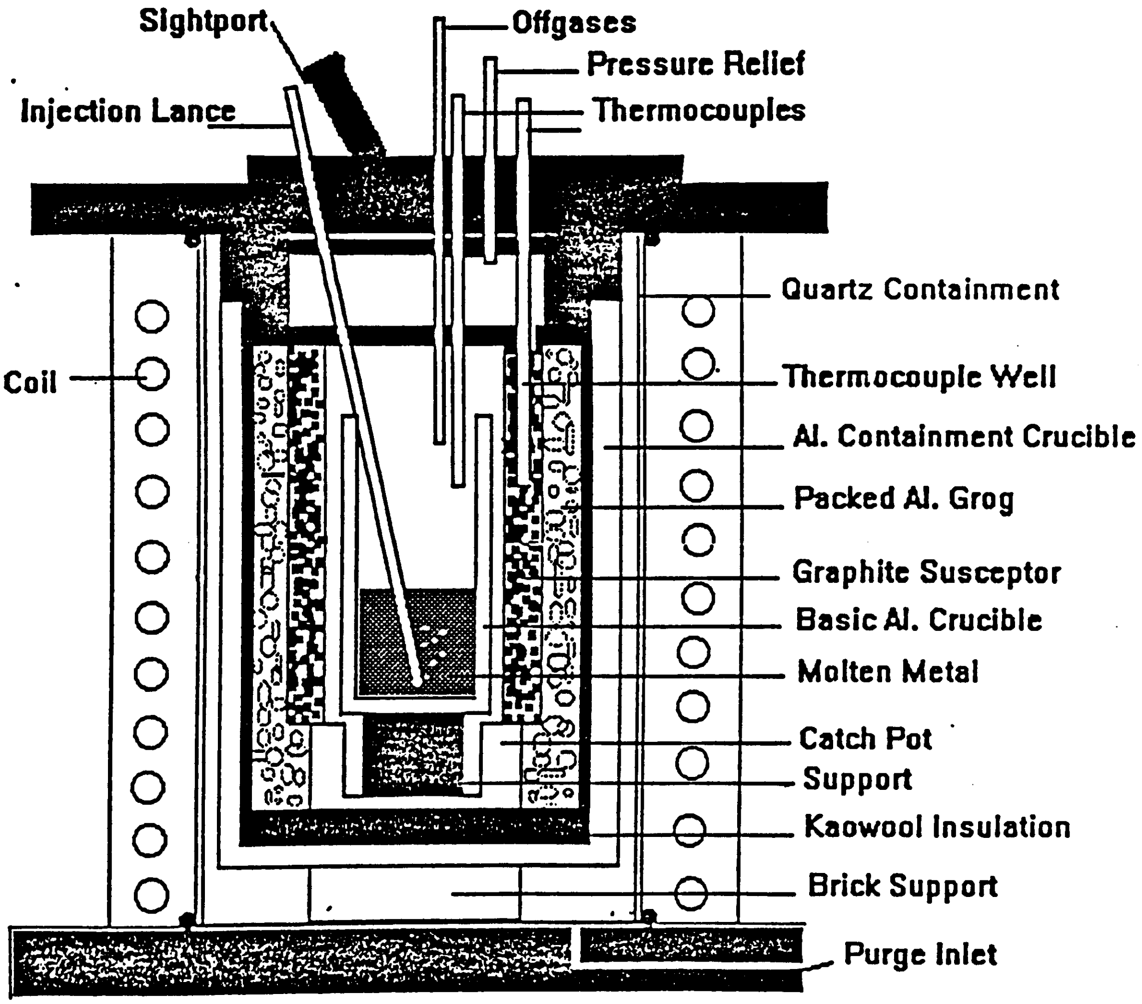

Figure 4. Schematic of induction furnace.

of the melt were taken at certain intervals of time. For this purpose, J-shaped quartz tubes were dipped into the melt and removed after they had filled up with copper. The melt samples were analyzed for their impurity concentration with Inductively Coupled Plasma/Mass Spectroscopy (ICP/MS) as described in section 2.4. The evaporating gases were captured with a condenser placed in the offgases line.

Cadmium, zinc and bismuth were used as the impurities in the copper melt experiments. All the impurities used were supplied by Alfa Aesar and their minimum purity was about 99.9%. Similarly, electrolytic tough pitch copper (min 99.9 % Cu, NSRW Inc.) was used. In some cases, these runs were repeated by using a 5 cm slag layer at the top of the melt to avoid evaporation from the melt surface, as will be explained in section 3.1.4. The composition of the slag used was 22 % $Al_20_3$, 22 % $SiO_2$, 42 % CaO, and 14 % $B_2O_5$ (all reagent grade, Alfa Aesar). Regarding the argon used, its oxygen content was less than 0.1 ppm by volume (grade 5, BOC Gases, Inc.).

## 2.3. Aerosol Sampling Experiments

Several experiments were done in which cadmium vapors emanating from a copper melt were sampled and condensed, and the resulting aerosols were size-segregated. The starting cadmium concentration added to the copper was 0.2-0.7% because of the limited loading capacity of the substrates in the cascade impactor. During a non-sampling period, the aerosol was sent to the exhaust line after passing through the sampling probe. When a sample was to be taken, the impactor was brought on-line to size-segregate the aerosol after coming out of the probe. The pressure drop through the impactor was monitored to check that the total flow was 30 L/min.

In the impactor, five rotating stages having 50 % cut sizes of 18, 3.2, 1.8, 0.32, and 0.056 μm were used. Each of these stages collects virtually 100% of all particles bigger than its cut size and 50% of the particles that are of the cut size. A glass fiber afterfilter (Millipore APFA04700) captured all remaining particles down to about 0.016 μm. Thin aluminum foils were used as impaction substrates on the stages. In order to prevent particle bounce, the foils were sprayed with a thin layer of silicone grease and then baked for 2 hours at 65 °C to evaporate any volatiles in the silicone.

Since the samples contained copper and some carbon in addition to the cadmium itself, they were analyzed with ICP/MS for the cadmium content as described in section 2.4. In some samples the copper content was also analyzed to look for evidence of a certain aerosol formation mechanism, as will be explained in section 3.2. The carbon is thought to come from various sources inside the furnace, such as the graphite susceptor, graphite crucible, and graphite-impregnated insulators.

### 2.4. Characterization of Samples

Prior to analyzing the copper melt samples, they were dissolved completely in 20 ml of diluted (about 60% by volume) $HNO_3$. All samples were then diluted in sufficient amount so as to avoid clogging of the ICP/MS instrument nebulizer. Aerosol samples only required 10 ml of diluted $HNO_3$ and less subsequent dilution due to their smaller mass as compared to melt samples.

The ICP/MS instrument used for this work was an ELAN Model 250 manufactured by Sciex. The data were automatically collected and evaluated using an

ELAN 5000 software by Perkin Elmer. The operating parameters for the ICP/MS equipment were an RF incident power of 1.25 kW and coolant, auxiliary, and nebulizer argon flows of 21, 3, and 1.17 L/min, respectively. The mass calibration was carried out before each analysis using a multielement standard solution containing Pb, Cd, Cu, and Mg. All data were obtained by operating in the peak hop mode, and analytes were quantified by the external standard method.

Some cadmium aerosol samples were observed using a JEOL Scanning Electron Microscope at 0.8 kV and at magnifications ranging from 250X to 80,000X. Results will be presented in section 2.5.2.

## 2.5. Results and Discussion

### 2.5.1. Evaporation Rates

Evaporation experiments have been carried out for cadmium, zinc, and bismuth from copper melts. Since it was seen that flow rates above 1.5 L/min cause too much splashing inside the furnace, especially when a slag layer is used, this flow rate was chosen as an upper limit for the experiments.

Plots of the impurity concentration in the melt versus time are presented and discussed in the following paragraphs. An exponential regression of the form

$$\frac{[\%X]}{[\%X]_o} = \exp(-K_e t) \qquad (1)$$

is fitted to the data points in each case, giving values for $[\% X]_o$ , the initial impurity concentration, and for $K_e$ , the overall evaporation coefficient. $[\% X]_o$ has to be determined in this way because it is very difficult to control in the experiments, as some of the impurity dropped into the melt evaporates instantaneously before it is homogenized in the solution.

Figures 5 and 6 present the evaporation curves for cadmium from copper at flow rates of 0.75 L/min and 1.5 L/min, respectively. At the 0.75 L/min flow rate, five separate experiments were conducted, and the values of $K_e$ obtained were 0.0199, 0.0149, 0.0215, 0.0194, and 0.0216 $\text{min}^{-1}$. These coefficients give very similar curves, and an "average" experimental curve is also plotted with an average value of $K_e$, 0.0195 $\text{min}^{-1}$. For the 1.5 L/min case, four different runs are plotted as well, with their $K_e$'s being 0.0392, 0.0197, 0.0264, and 0.0234 $\text{min}^{-1}$. They are also very similar curves, and their average $K_e$ is 0.0272 $\text{min}^{-1}$. As would be expected because of the higher flow rate, this value is higher than that for the 0.75 L/min case, which means that the evaporation is faster.

Figure 7 plots the evaporation of zinc from copper at 0.75 L/min. The experimental value of $K_e$ is 0.00461 $\text{min}^{-1}$. The copper-zinc-slag case at the same flow rate is presented in Figure 8. Here, $K_e$ = 0.00173 $\text{min}^{-1}$, which is again lower than the copper-zinc case because evaporation from the melt surface is prevented.

Finally, Figure 9 shows the evaporation of bismuth from copper at 0.75 L/min with a slag layer. In this case, $K_e$ = 0.000483 $\text{min}^{-1}$.

### 2.5.2. Aerosol Particle Size Distributions

Cadmium aerosols formed after evaporation from copper were sampled at different points in time in three independent runs at 0.75 L/min. The percent of the total cadmium

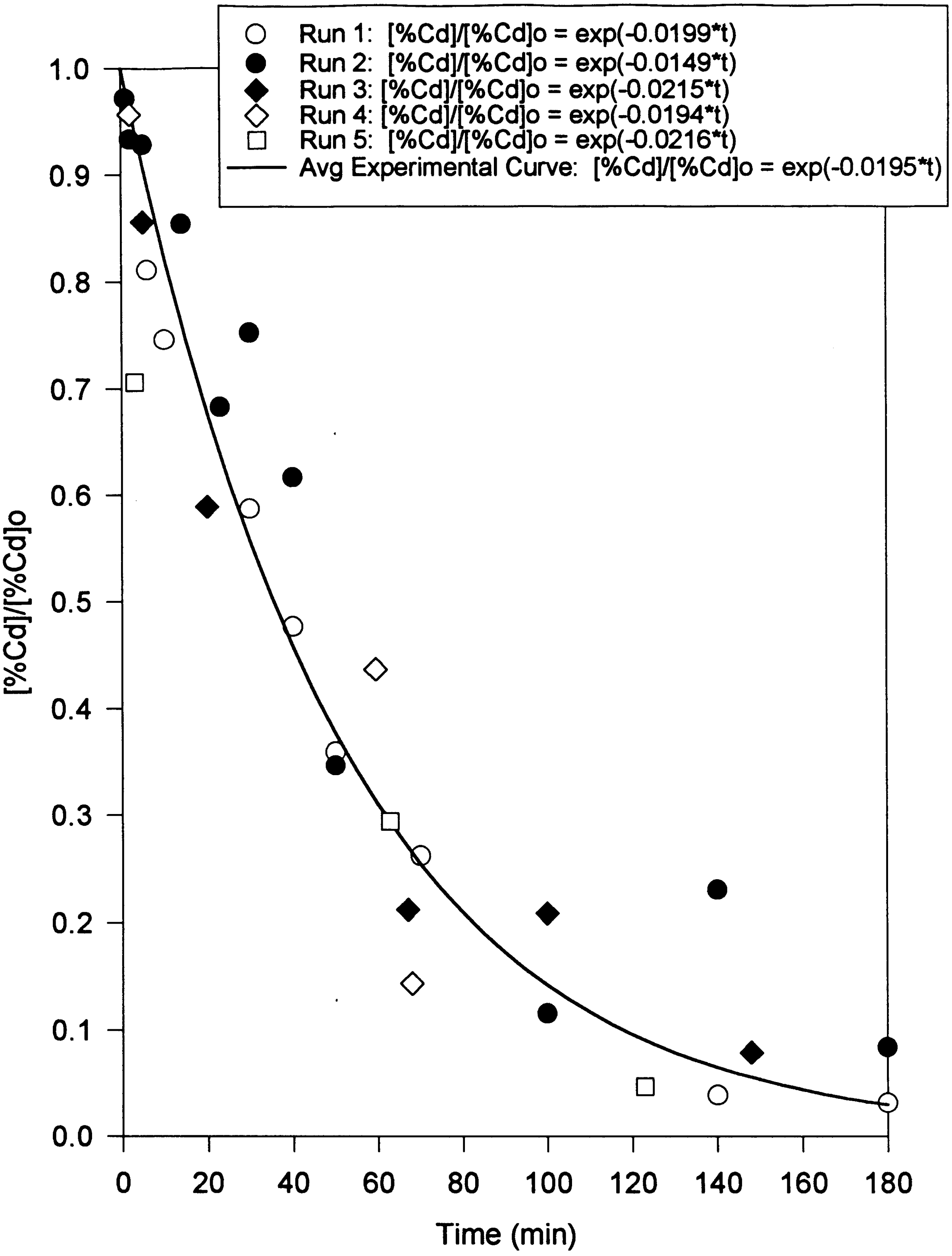

Figure 5. Evaporation of cadmium from copper.
(T=1473 K, gas flow = 0.75 L/min, single 1/4" OD gas lance)

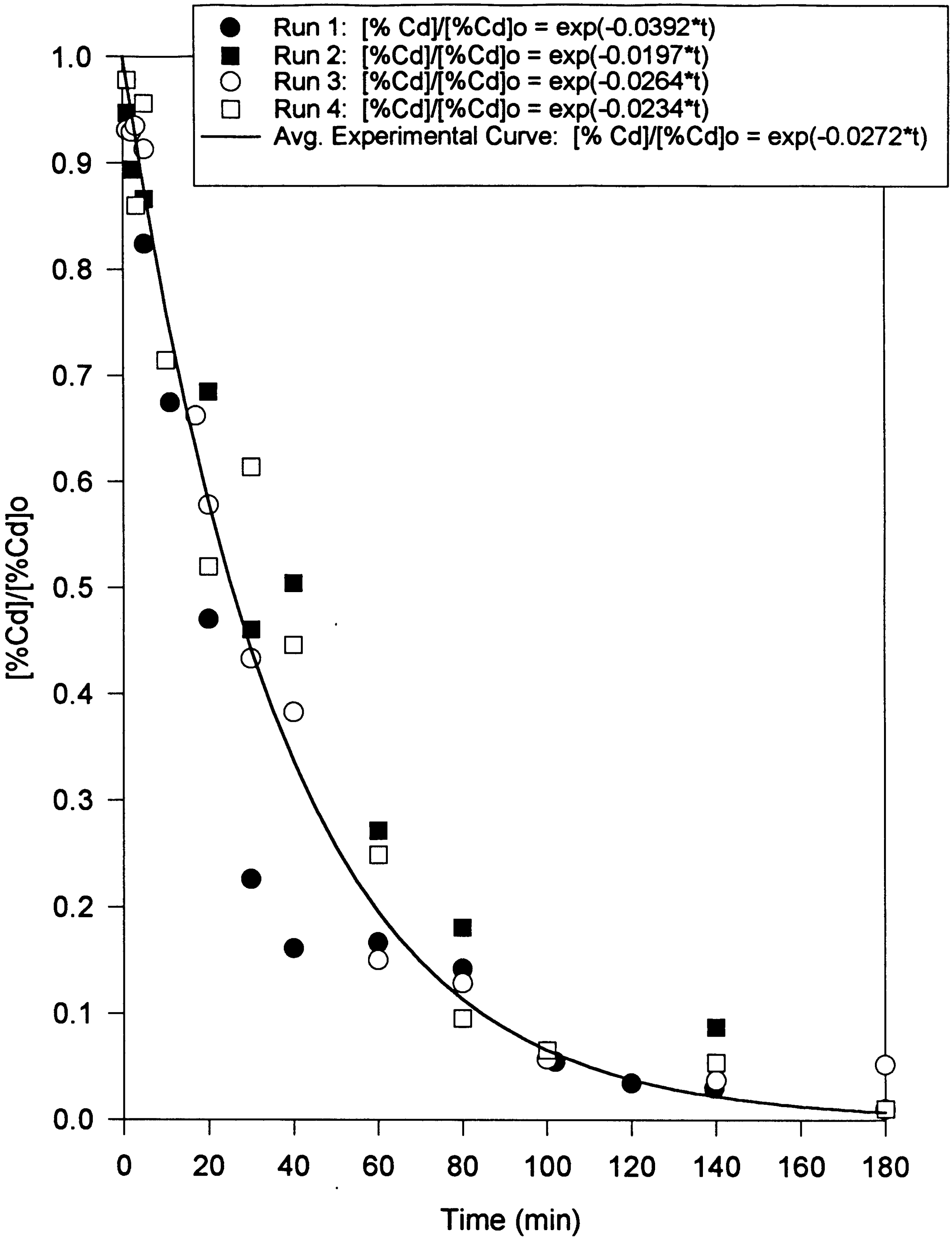

Figure 6. Evaporation of cadmium from copper.
(T=1473 K, gas flow = 1.5 L/min, single 1/4" OD gas lance)

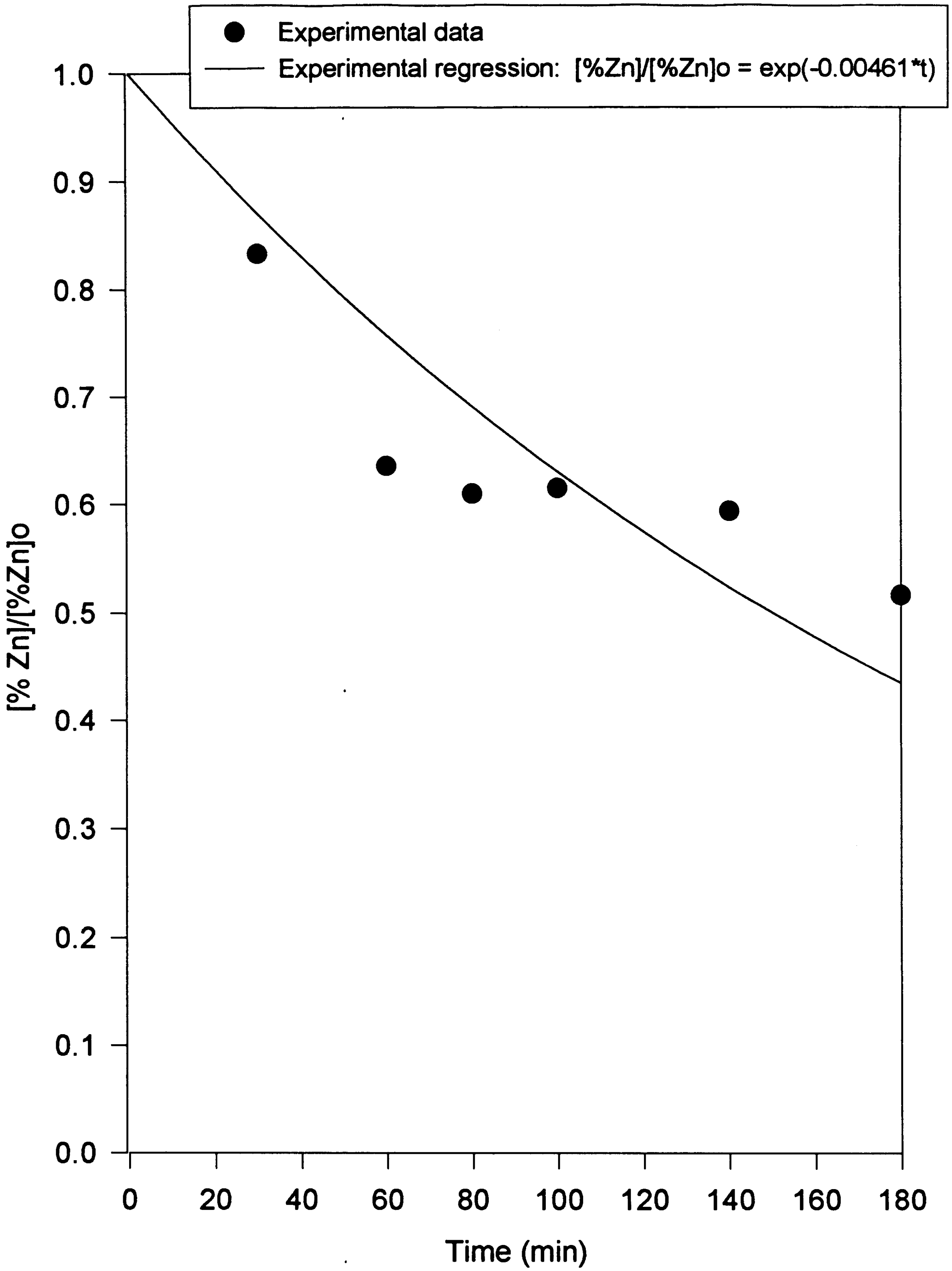

Figure 7. Evaporation of zinc from copper.
(T=1473 K, gas flow = 0.75 L/min, single 1/4" OD orifice)

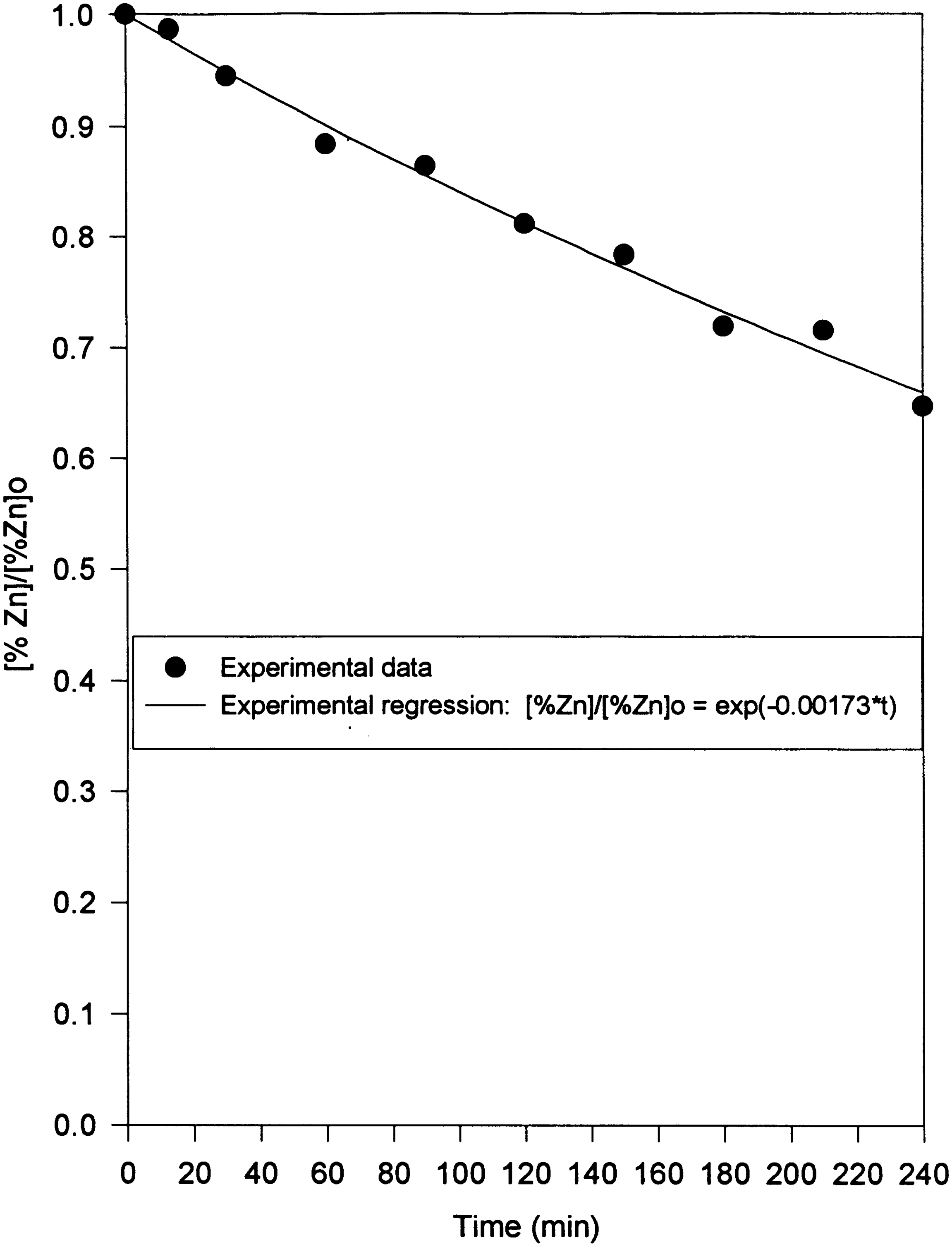

Figure 8. Evaporation of zinc from copper with a slag layer.
(T=1473 K, gas flow =0.75 L/min, single 1/4" OD orifice)

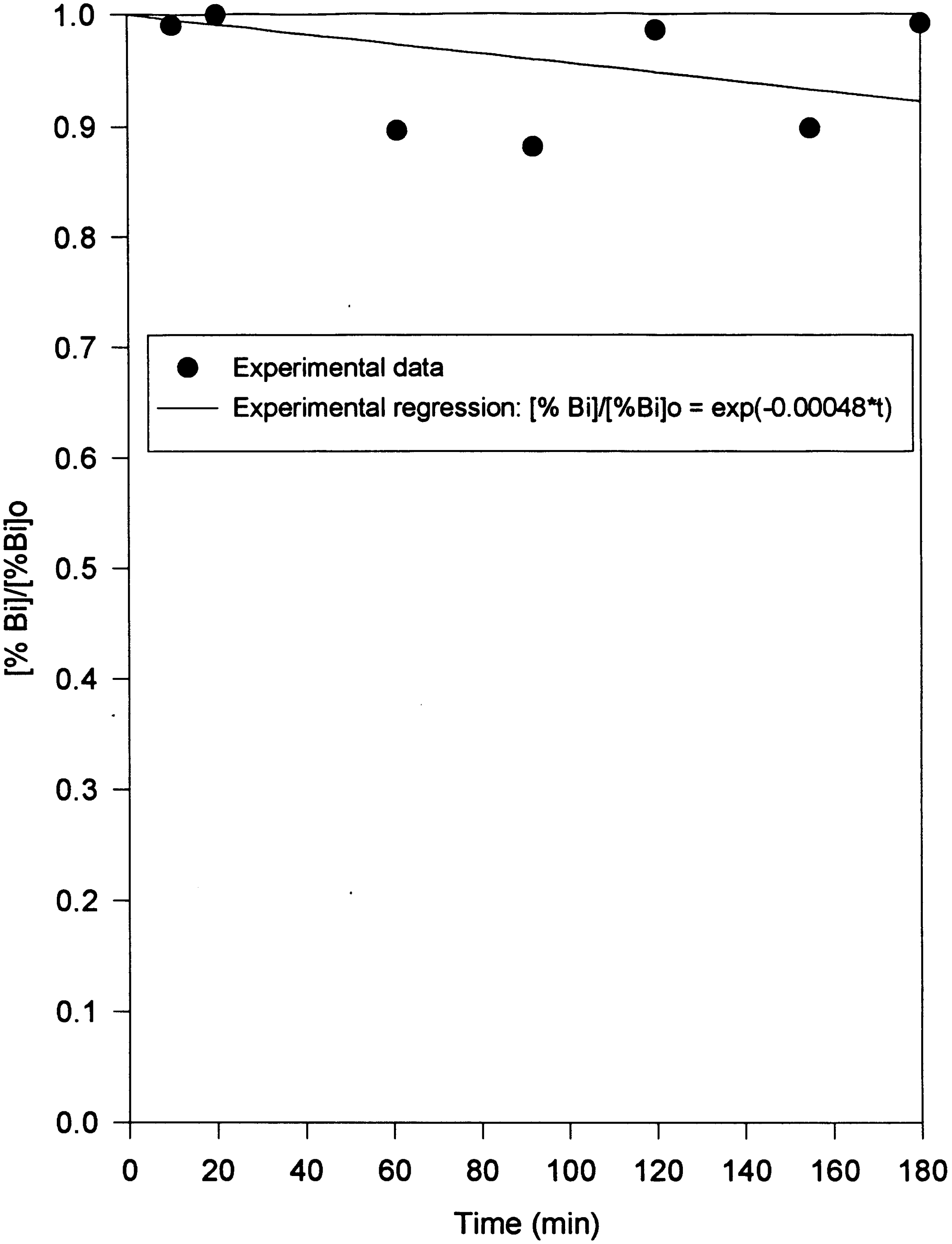

Figure 9. Evaporation of bismuth from copper with a slag layer.
(T=1473 K, Q=0.75 L/min, single 1/4" OD orifice)

collected in each size range is plotted vs. *[% Cd]* in the melt in Figures 10-12. In the first run there is a sharp concentration of particles in the +0.32/-1.8 μm size range which recedes when the cadmium concentration in the melt is about 0.01%. At this point the amounts in the +0.056/-0.32 μm and +0.016/-0.056 μm size ranges grow. Towards the end of the run (at about 0.0063% Cd in the melt), it is seen that the amount in the +0.056/-0.32 μm range starts to decrease while the +0.016/-0.056 μm range continues to increase. As seen in the next two runs, it can be hypothesized that this same trend would continue if this experiment had been run for a longer time. The percentage of particles collected at 18 μm is rather stable throughout the run at 10-20%.

In the second run, the distribution starts out as being bimodal with peaks at +0.32/-1.8 μm and 18 μm. The magnitude of the 18 μm peak stays constant at around 46%. The +0.32/-1.8 μm peak again diminishes as in the first run, giving rise to a relatively high +0.056/-0.32 μm peak at about 0.023% Cd in the melt and to a high +0.016/-0.056 μm peak at about 0.006% Cd in the melt and onwards.

The third run also starts out with peaks at 0.32 and 18 μm. By the time the cadmium concentration in the melt reaches 0.0069%, the distribution in the lower sizes again changes significantly, with the +0.32/-1.8 μm peak decreasing and the +0.056/-0.32 μm peak increasing. At about 0.004% Cd, the +0.016/-0.056 μm peak becomes the dominating one in the smaller sizes, while the +0.056/-0.32 μm peak starts to decrease. As to the magnitude of the 18 μm peak, it ranges between 17 and 23%, except for the sample taken at 0.0069% Cd, where it is 33%.

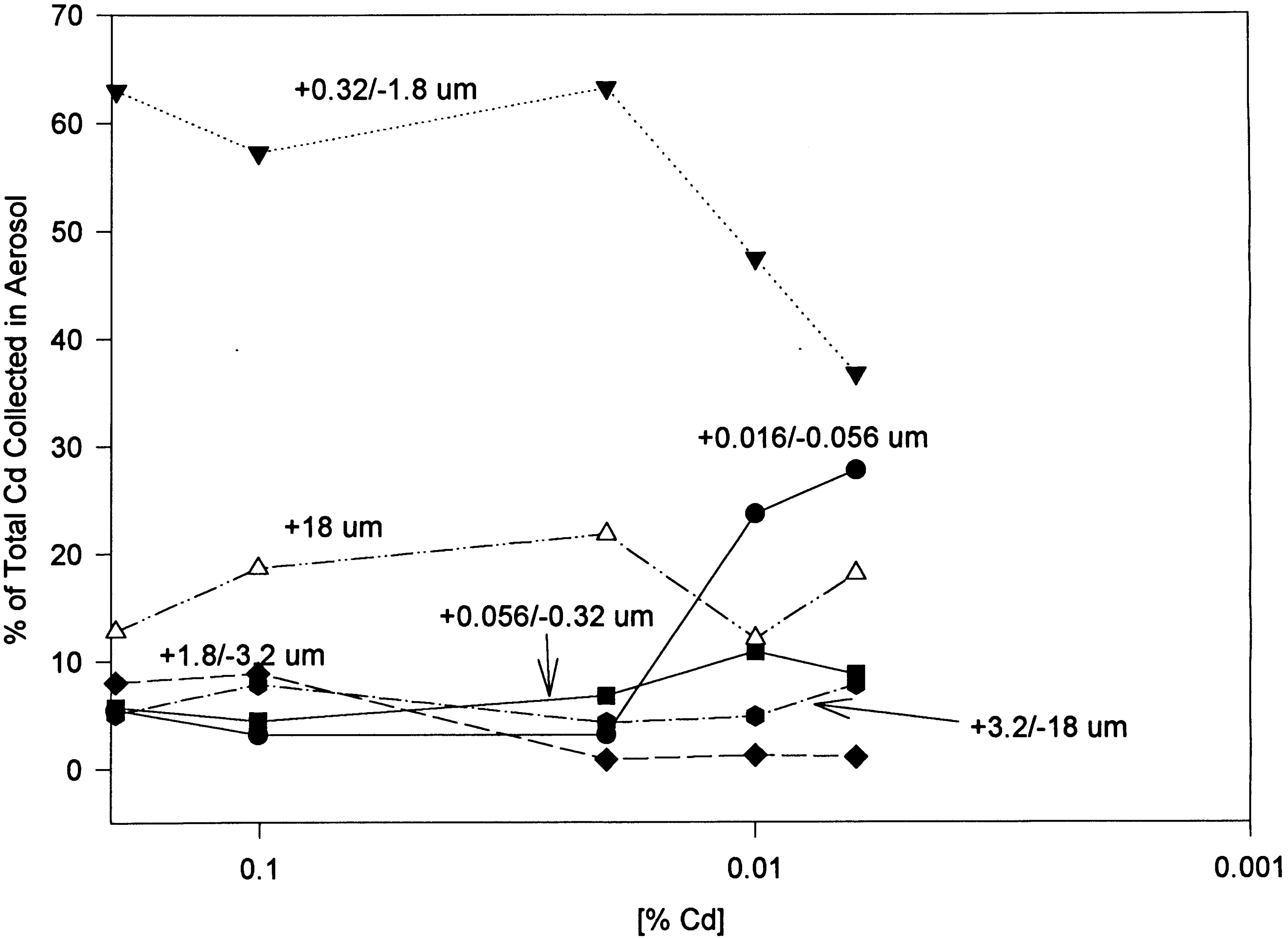

Figure 10. Variation of relative amounts of cadmium particle sizes with [% Cd] in the melt (Run 1).

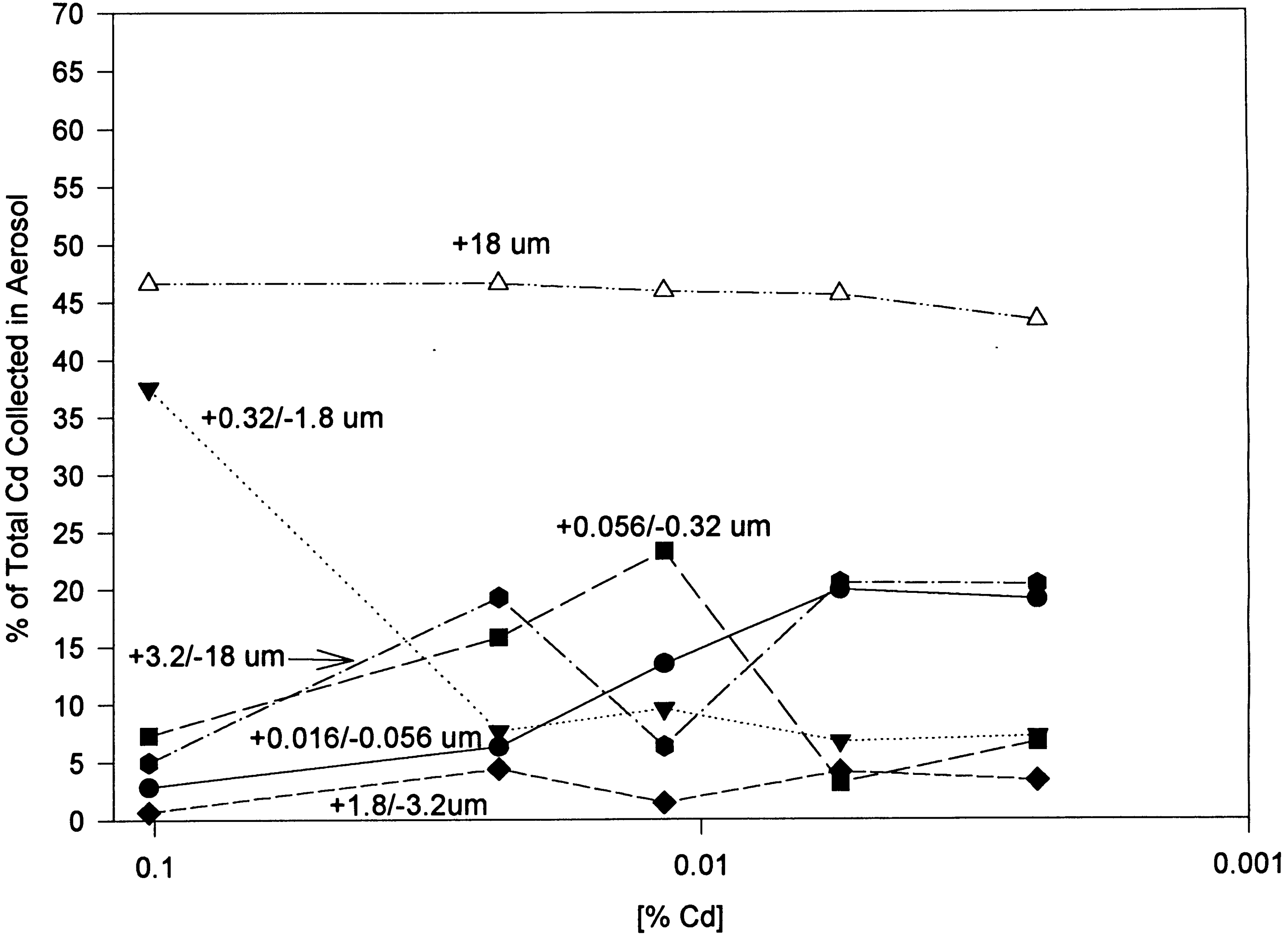

Figure 11. Variation of relative amounts of cadmium particle sizes with [% Cd] in the melt (Run 2).

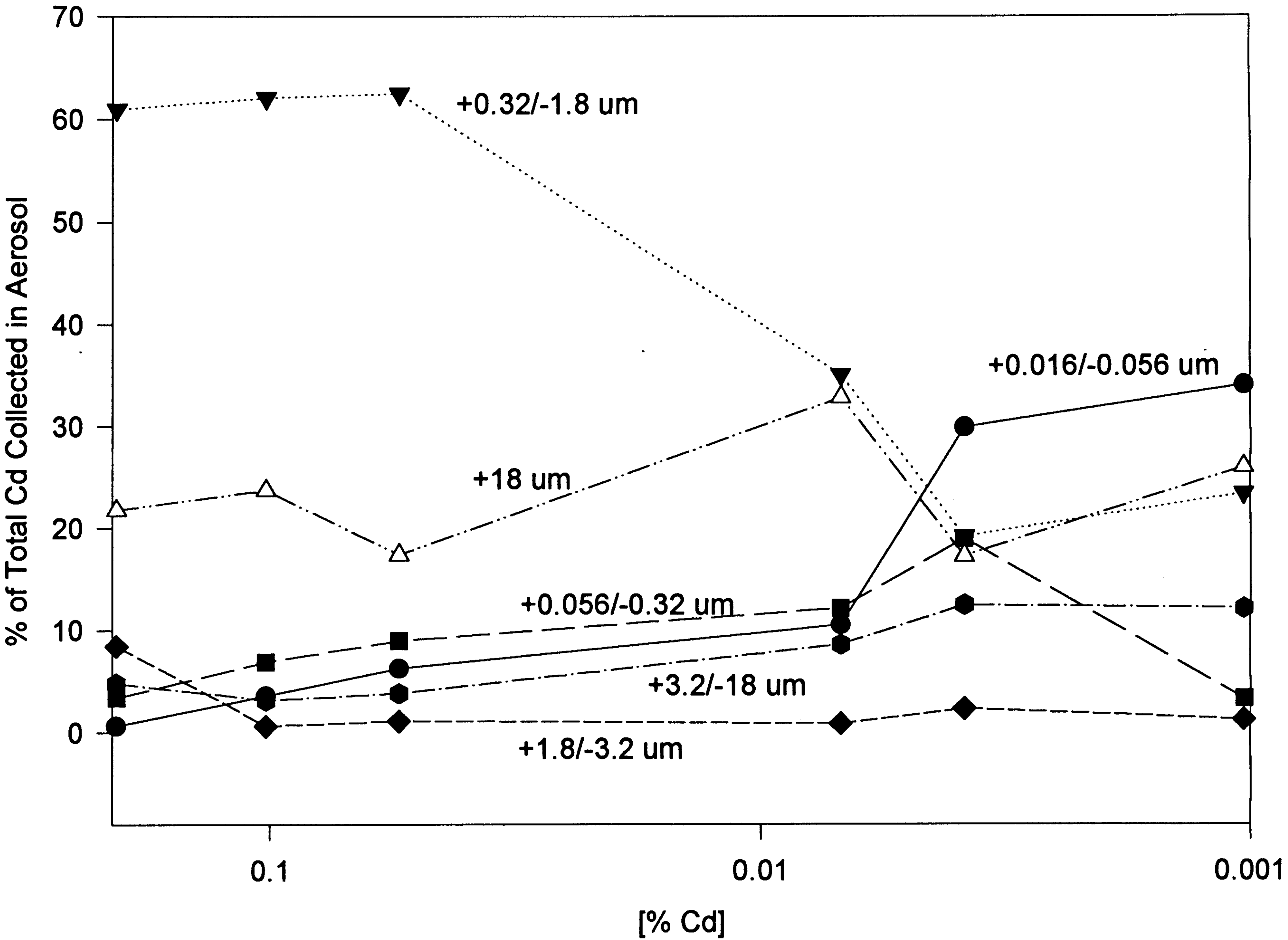

Figure 12. Variation of relative amounts of cadmium particles sizes with [% Cd] in the melt (Run 3).

Thus, it can be seen from these results that, while the amount of cadmium collected in the >18 μm size range tends to remain relatively constant, the relative amounts of the smaller sizes change during the runs. At higher Cd concentrations in the melt, the +0.32/-1.8 μm size tends to predominate, while at lower Cd concentrations the +0.056/-0.32 μm and then the +0.016/-0.056 μm sizes start to peak. The change appears to begin when the Cd concentration in the melt is about 0.007-0.02%.

Regarding the relative amounts of copper and cadmium found in each size range, Table 1 is a summary of the results. Often too little material was collected in the +1.8/-3.2 μm cut size, so the percentage of Cd in that range is generally uncertain, although in two samples it was found to be > 99%. It can be seen that the percentage of cadmium increases with decreasing particle size. At +0.32/-1.8 μm and smaller sizes, the deposits are almost exclusively composed of cadmium. These results will be explained in section 3.2.

Table 1. Relative Amounts of Cadmium and Copper Found in Each Particle Size Range in Three Copper-Cadmium Experiments

| **Cut Size** | **Run 1** | **Run 2** | **Run 3** |
|---|---|---|---|
| **18 μm** | 50-75% Cd | 10-30% Cd | 40-75% Cd |
| **3.2 μm** | 78-87% Cd | 40-70% Cd | 70-90% Cd |
| **1.8 μm** | uncertain | uncertain | uncertain |
| **0.32 μm** | >99.5% Cd | >99.5% Cd | >99% Cd |
| **0.056 μm** | >99.5% Cd | >99.5% Cd | >99% Cd |
| **0.016 μm** | >99.5% Cd | >99.5% Cd | >99% Cd |

SEM micrographs were taken of some samples to determine the morphology of the collected particles. A sample in the beginning and one in the end of a run were chosen and the micrographs are shown in Figures 13-15. The large particles (Figures 13a, 13b, and 14a) have very irregular shapes and show evidence of having many small particles adhering to them. Since elements with higher atomic numbers appear brighter, the small particles are thought to be cadmium while the large ones are probably copper. Supporting this is the fact that a small regular hexagon is seen in Figures 14a and 14b, indicating that they are probably single Cd crystals (Cd has an HCP crystal structrure). The other small polygonal shapes seen are probably hexagonal structures in different orientations.

In the small particle ranges, particles are seen as single units without adhesions. It appears that in the beginning of the run there is a slightly higher proportion of non-spherical (square, trapezoidal, etc.) particles than in the end, as shown in Figures 14b and 15a.

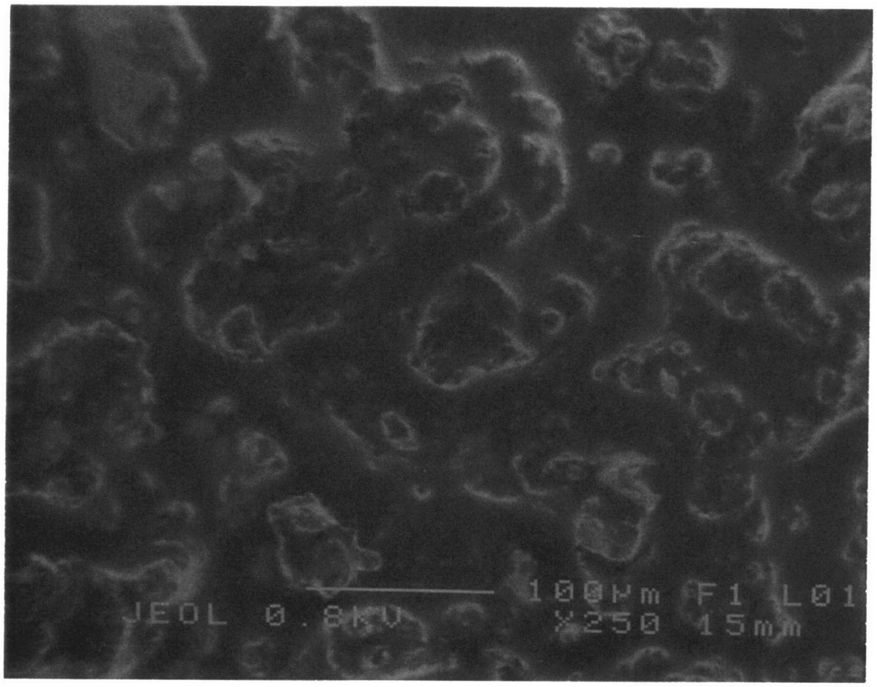

(a) size range: +18 µm

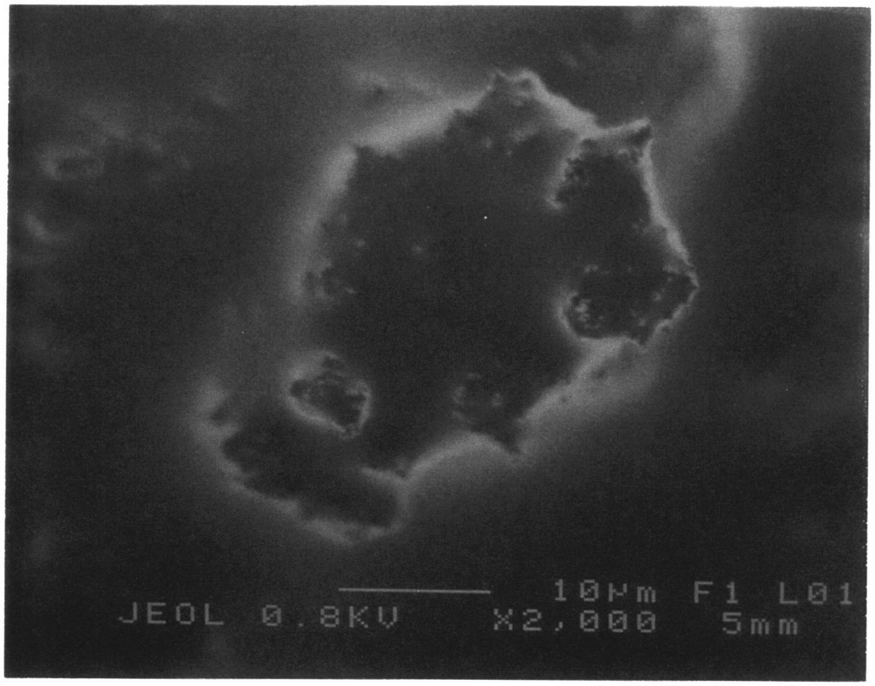

(b) size range: +18 µm

Figure 13. SEM micrographs of aerosol sample taken at the beginning of a run.

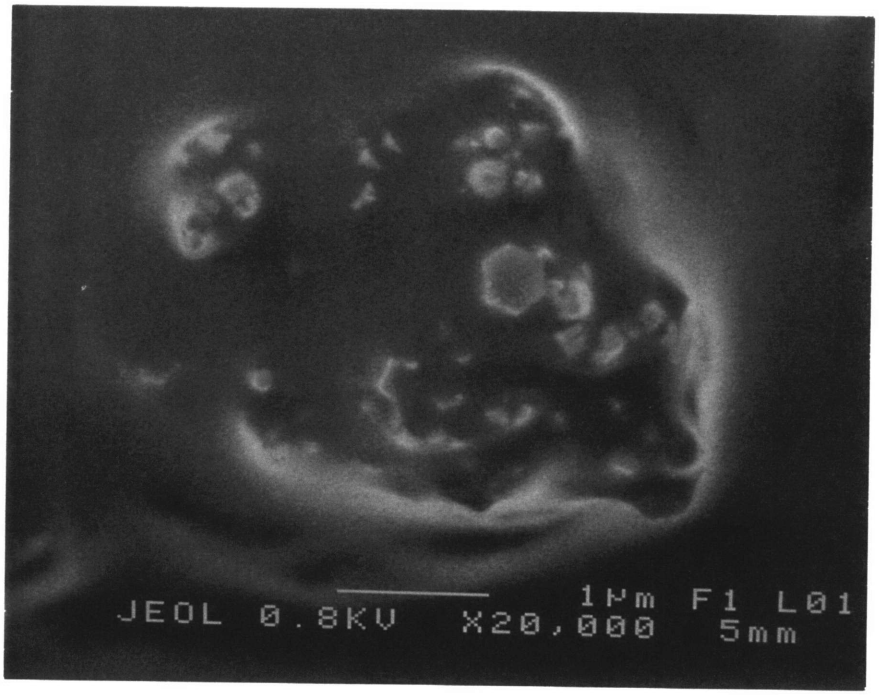

(a) size range: +3.2/-18 µm

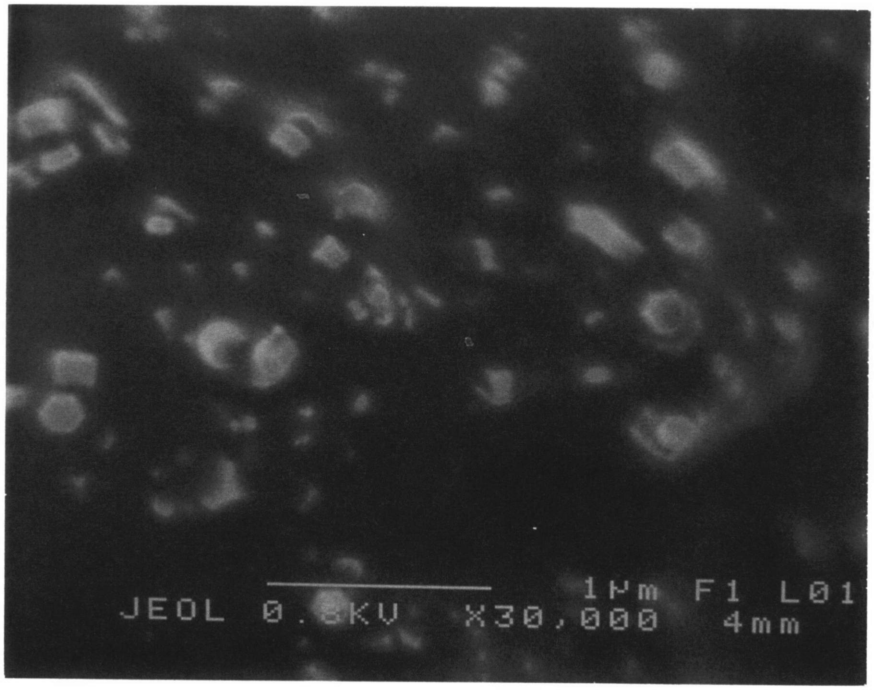

(b) size range: +0.32/-1.8 µm

Figure 14. SEM micrographs of aerosol sample taken at the beginning of a run.

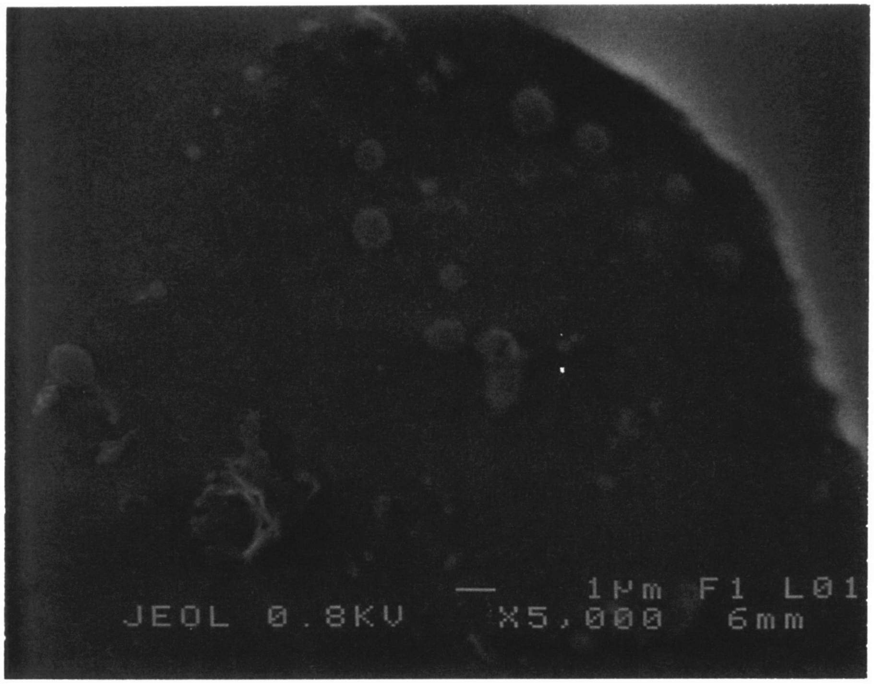

(a) size range: +0.32/-1.8 μm

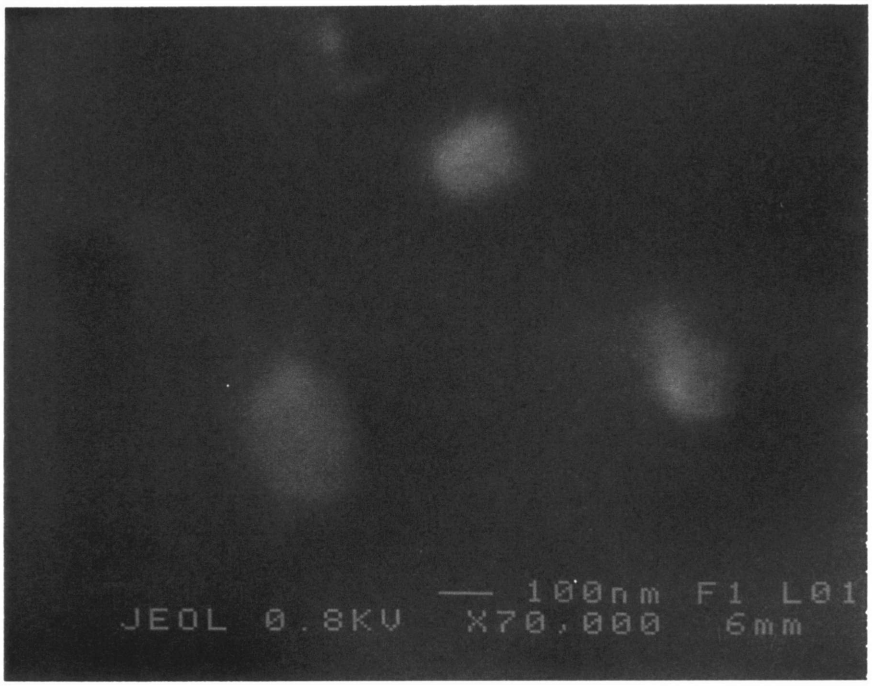

(b) size range: +0.32/-1.8 μm

Figure 15. SEM micrographs of aerosol sample taken at the end of a run.

# 3. THEORY

## 3.1. Evaporation Rates

### 3.1.1. Physical Model

Figure 16 is a picture of the physical model considered in the calculation of the evaporation rates of solutes from a bubbled molten metal bath. The first evaporation mechanism considered is that from the molten metal to the bubbles and the second is through the surface of the melt. These mechanisms occur simultaneously, and each of them has a series of steps, starting in the liquid metal and ending with the condensation of the solute. Rapid movement due to bubbling and inductive stirring in the molten metal, and convective stirring in the gas phase, make transport in the liquid and gaseous bulk very fast and thus unlikely to be rate determining. Similarly, condensation can occur on a large area and it is aided by thermal convection currents inside the furnace (which will be explained later), so it should not restrict the rate of the process. As to the resistance presented by the interface reaction, it is important for low pressure operation, but its contribution to the overall mass transfer process at higher pressures is negligible. This is because at higher pressures the mean free path of the evaporating atoms is small ($6.3 \times 10^{-8}$ m for argon at 1 atm), rendering the interface reaction resistance insignificant as compared to the resistance in the gas boundary layer. Therefore, it will be assumed that the concentrations of X in the liquid and gas phases at the interface are in equilibrium.

The above considerations suggest that the rate of evaporation by each of the above mentioned mechanisms can be limited by diffusion of the solute in either the melt boundary layer or the gas boundary layer. The solute concentrations in both of these boundary

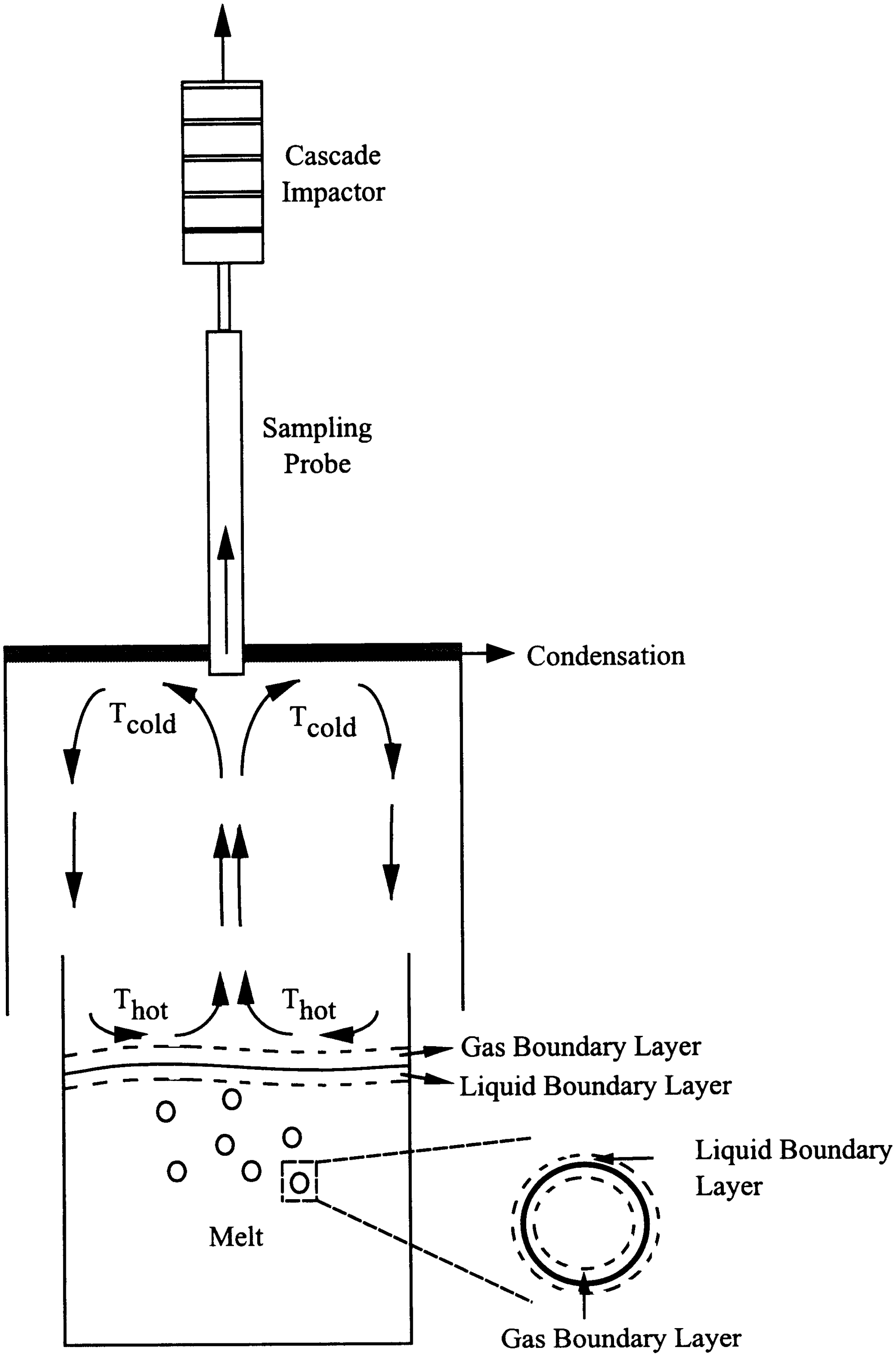

Figure 16. Schematic of the physical model used.

layers as approximated in the model used are shown in Figure 17, where $y_X$ and $x_X$ are the mole fractions of X in the gas phase and melt, respectively, $\delta$ is the thickness of each boundary layer, and the subscripts "l", "g", and "i" represent liquid, gas, and interface, respectively. These concentration profiles apply for the melt surface and for each bubble in the melt.

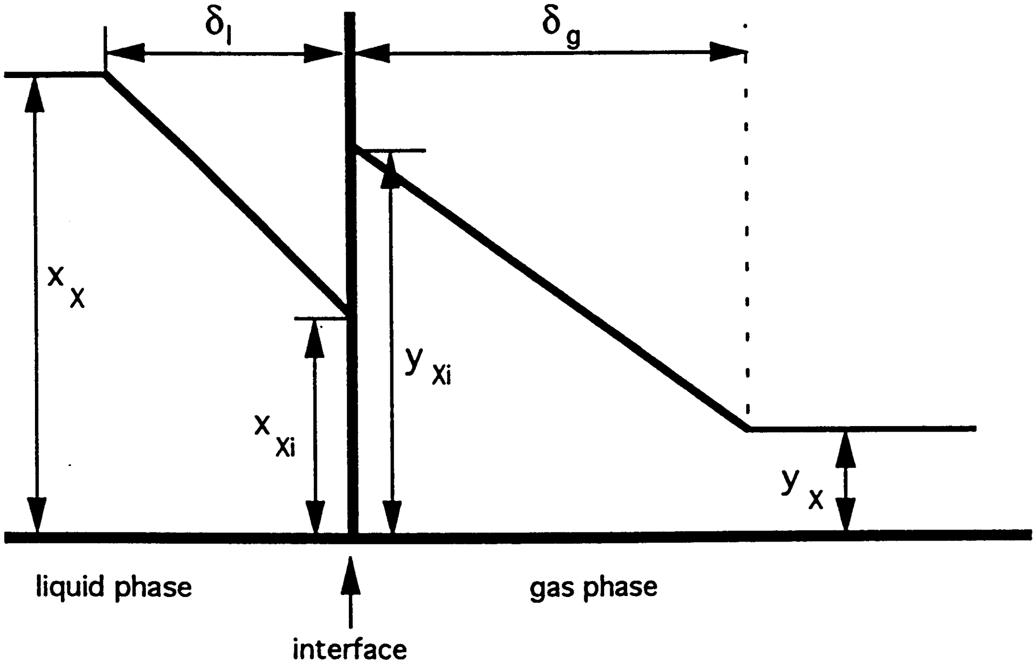

Figure 17. Concentrations of solute X in the gas and liquid phases.

### 3.1.2. Overall Mass Transfer Rates

One important assumption in this model is that the solutes considered are present in sufficiently low concentrations in the molten metal so that they can be taken as infinitely dilute. The basic mass balance equation applying to the solute can be expressed as follows:

$$\begin{pmatrix} Mass\_flux \\ evaporating \\ from\_melt \end{pmatrix} = \begin{pmatrix} Mass\_flux \\ to\_bubbles \end{pmatrix} + \begin{pmatrix} Mass\_flux \\ through \\ melt\_surface \end{pmatrix} \tag{2}$$

Assuming that the metal bath is well mixed by bubbling and convective stirring so that the solute concentration in the bulk liquid is uniform, this equation translates to

$$\frac{-M_l d[\%X]}{100 MW_X dt} = \frac{K_{ol,b}\rho_l A_b([\%X]-[\%X]_{eq,b})}{100 MW_X} + \frac{K_{ol,ms}\rho_l A_{ms}([\%X]-[\%X]_{eq,ms})}{100 MW_X} \tag{3}$$

where the variables are defined as follows:

$[\%X]_{eq}$: hypothetical solute concentration in the melt in equilibrium with the partial pressure $P_X$ in the bulk gas phase,
$MW_X$ : molecular weight of X
$M_l$ : mass of the melt
$K_{ol}$ : overall mass transfer coefficient based on liquid side concentrations (will be discussed later)
$A$ : area

and the subscripts "b" and "ms" refer to the bubbles and the melt surface, respectively.

In order to facilitate the computation of the flux of X going to the bubbles, the first term on the right hand side of equation (3) will be expressed as:

$$Q\left(\frac{P_X^{exit}}{P_{Ar}}\right) \tag{4}$$

where $Q$ is the flow rate of argon in mol/s and $P_x^{exit}$ is the solute partial pressure in the bubble when it bursts at the surface of the melt. To relate $P_x^{exit}$ to $[\%X]$, the concept of "efficiency of gas purging" [10] will be introduced. This is the ratio of the actual exit partial pressure of the solute to its equilibrium exit partial pressure in the bubble, and it is defined by the following equation, assuming only monatomic evaporation takes place:

$$Z = 1 - \exp(-\phi_A) = \frac{P_X^{exit}}{f_X[\%X]K_{eq}} \tag{5}$$

Here $\phi_A$ is called the dimensionless contact area, which determines the extent to which equilibrium is reached in the bubbles:

$$\phi_A = \frac{K_{ol,b}\rho_l A_b P_{Ar}}{100 MW_x Q f_X K_{eq}} \tag{6}$$

When $\phi_A$ is 3 or more, it can be considered that the equilibrium partial pressure of the solute is reached in the bubbles. The derivation of the expressions for $Z$ and $\phi_A$ is included in Appendix , as well as a justification for neglecting polyatomic evaporation.

Inserting $Z$ into expression (4), the bubble evaporation term becomes

$$\frac{QZf_X K_{eq}[\%X]}{P_{Ar}} \tag{7}$$

For the cases when $P_X << P_{Ar}$, this expression can be evaluated easily by assuming $P_{Ar}=P_{tot}=1$ atm. For all other cases, such as those of bismuth, lead, and zinc evaporating from iron, $P_X$ has to be evaluated at each point in the bath by solving the following integral which is derived in Appendix A:

$$\int_0^{P_X} \frac{dP}{(f_X K_{eq}[\%X] - P)(1-P)^2} = \frac{K_{ol,b}\rho_l A_b h}{100 MW_X Q H f_X K_{eq}} \tag{8}$$

Here $h$ is the distance from the bottom of the bath, assuming an even bubble distribution throughout the height of the melt, $H$. Thus, $[\% X]_{eq,b}$ varies with position of the bubble in the melt and also with time, because the concentration of X in the melt varies with time as well. This makes the mathematical analysis rather complicated, although it can be simplified by considering an average solute pressure in the bubble. This value is taken as the solute pressure in the bubbles in the middle of the melt (at $h=H/2$). This procedure requires that the values of $P_X$, $[\% X]_{eq,b}$ , and $[\%X]$ be calculated at discrete time intervals in a stepwise manner using software such as Maple.

Regarding the second term on the right of equation (3), which accounts for evaporation from the melt surface, the only unknown quantity is $[\% X]_{eq,ms}$ . This is the hypothetical solute concentration in the melt that would be in equilibrium with the solute partial pressure $P_{X,top}$ in the bulk gas above the melt. As will be explained later, it is assumed that this gas is so well stirred by the convection currents together with the bulk flow coming from the bursting bubbles that $P_{X,top}$ is uniform in the gas above the melt except for a small boundary layer over the melt surface. It has been found experimentally that the value of $P_{X,top}$ is very low and neglecting it increases the overall theoretical evaporation rate by about 3-5%, depending on the solute. However, the theoretical results remain within +/-10% of the actual evaporation rates. Thus, $P_{X,top}$ (and so $[\%X]_{eq,ms}$) will be neglected when obtaining theoretical curves for all the solutes.

Combining equations (3) and (7), and assuming $P_X << P_{Ar}$, the solution to the resulting equation is

$$\frac{[\%X]}{[\%X]_o} = \exp\left[\left(-\frac{100 MW_X QZ f_X K_{eq}}{M_l P_{Ar}} - \frac{K_{ol,ms}\rho_l A_{ms}}{M_l}\right)t\right] \qquad (9)$$

### 3.1.3. Overall Mass Transfer Coefficients

The expression used for the overall mass transfer coefficient $K_{ol}$ is the following (detailed derivation found in Appendix B):

$$\frac{1}{K_{ol}}=\frac{1}{k_l}+\frac{1}{\left(\frac{100P_{tot}K_{eq}MW_X f_X}{\rho_l RT}\right)k_g}=\frac{1}{k_l}+\frac{1}{k_g'} \tag{10}$$

As shown, $K_{ol}$ is composed of liquid and gas phase mass transfer resistances represented by $1/k_l$ and $1/k_g'$ , respectively. In what follows, the calculation of $k_l$ and $k_g$ will be discussed. In the case of $k_g$, different physical situations lead to different expressions ($k_{g,b}$ and $k_{g,ms}$) in the cases of evaporation of X into the bubbles and from the melt surface, respectively. Thus, there will be two expressions for $K_{ol}$, which will be referred to as $K_{ol,b}$ and $K_{ol,ms}$ .

#### 3.1.3.1. Liquid Phase Mass Transfer Coefficient

The liquid phase mass transfer coefficient can be estimated by using the surface renewal model, also known as the Higbie model or penetration theory [11]. The surface renewal model postulates that a liquid element in the bulk comes in contact with the liquid/gas interface for a short time period, during which unsteady state diffusion occurs between the liquid element and the surface. At the end of this time period, the liquid element is swept away from the surface and replaced by a new element from the bulk. The equations describing the model are based on the assumption that the contact time is so short that the concentration gradient in the element does not penetrate to the side of the element away from the surface. In terms of the liquid phase mass transfer coefficient, $k_l$, Higbie's theory is reduced to the following form:

$$k_l = 2\sqrt{\frac{D_{X-l}}{t\pi}} \tag{11}$$

where $D_{X-l}$ is the diffusivity of X in the melt and $t$ is the time of contact of the liquid element with the surface layer. For a bubble of diameter $d_b$ approaching the surface with a velocity $U_b$, the contact time would be

$$t = \frac{d_b}{U_b} \tag{12}$$

Expressions for $D_{X\text{-}l}$, $d_b$, and $U_b$ are given in Appendix B.

### 3.1.3.2. Gas Phase Mass Transfer Coefficient for the Bubbles

The gas phase mass transfer coefficient for the bubbles is

$$k_{g,b} = \frac{D_{X-g}}{\delta_{g,b}} \tag{13}$$

The expression used for $D_{X\text{-}g}$ is discussed in Appendix B.

To estimate the value of $\delta_{g,b}$, two approaches can be taken. The first considers a gas flowing over a surface and equates the friction on the surface due to viscous flow to the inertial force of a mass element in the boundary layer [12]. After integrating the resulting expression over a characteristic length (in this case $d_b$), an average boundary layer thickness is obtained:

$$\delta_{g,b} = \frac{2}{3}\frac{d_b}{\sqrt{\mathrm{Re}}} \tag{14}$$

The other approach is given by Geddes [13], using the following formula:

$$\delta_{g,b} = \frac{D_{X-Ar}t(1-y_X)}{d_b}\left(0.083 + 6.58\frac{D_{X-Ar}t}{d_b^2}\right)^{-1} \tag{15}$$

where $t$ is the contact time used in Higbie's theory. The values obtained by the two approaches were very similar (about 2 mm) and an average was used in all calculations.

### 3.1.3.3. Gas Phase Mass Transfer Coefficient for the Melt Surface

At the melt surface, a physical situation different from that in the bubbles is encountered. Convection currents are driven by the temperature difference between the melt surface and the inner surface of the top plate of the furnace (see Figure 18). The latter is the coldest part in contact with the gas carrying the solute. When the hot gas reaches the "cold" plate, a significant amount of the solute it is carrying condenses on the plate, which lowers the partial pressure of the solute in the gas at the top. The same convection currents mix this gas with the rest so that the same low solute partial pressure is achieved near the melt surface, just above the gas boundary layer. This in turn drives additional mass transfer of solute from the melt surface into the gas.

This situation can be modelled as a natural convection process between two horizontal surfaces at different temperatures. Using a correlation recommended by McAdams [14] and assuming that $Sh = Nu$, the following equation was obtained to calculate the gas phase mass transfer coefficient for the melt surface, $k_{g,ms}$:

$$Sh = \frac{k_{g,ms} L}{D_{X-Ar}} = 0.54(Gr\,\mathrm{Pr})^{1/4} = 0.54\left(\frac{L^3 \rho_{Ar}^2 g \beta_{Ar} (T_{Ar,hot} - T_{Ar,cold})}{\mu_{Ar}^2} \frac{C_{p,Ar} \mu_{Ar}}{k_{Ar}}\right)^{1/4} \qquad (16)$$

where $L$ is taken as 9/10 of the average diameter of the furnace interior, $g$ is the acceleration of gravity, $C_{p,Ar}$ is the heat capacity of the gas, $k_{Ar}$ its thermal conductivity, $\beta_{Ar}$ its thermal coefficient of volume expansion, $\rho_{Ar}$ its density, and $\mu_{Ar}$ is its viscosity. All gas properties are taken at $T = 0.5(T_{Ar,hot} - T_{Ar,cold})$. Further details are presented in Appendix B.

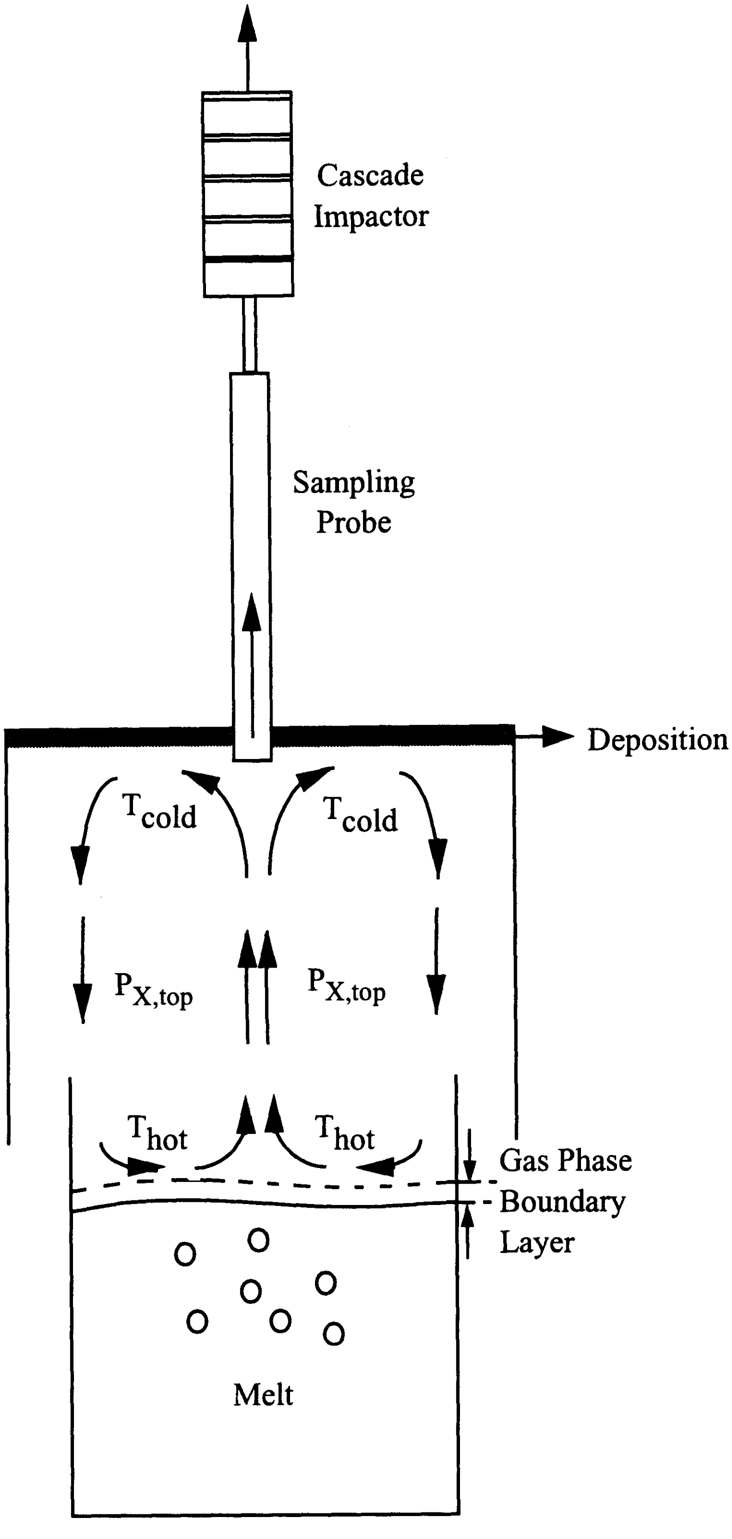

Figure 18. Thermal convection currents above the melt surface.

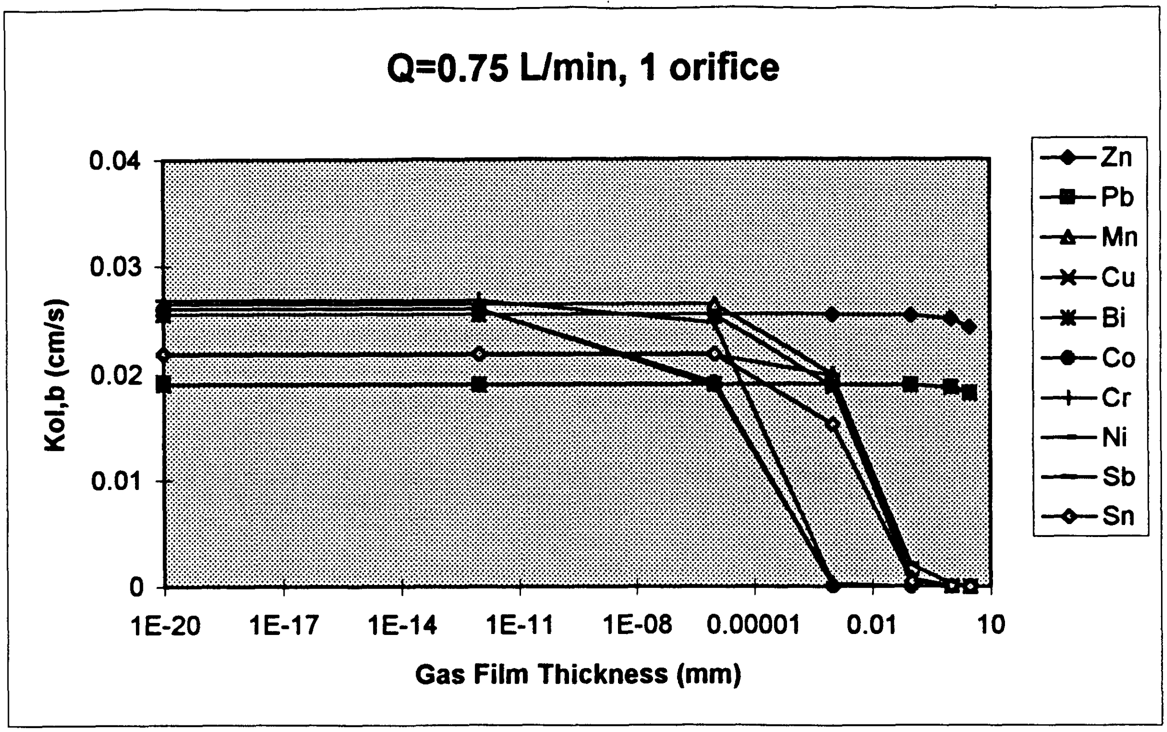

(1a)

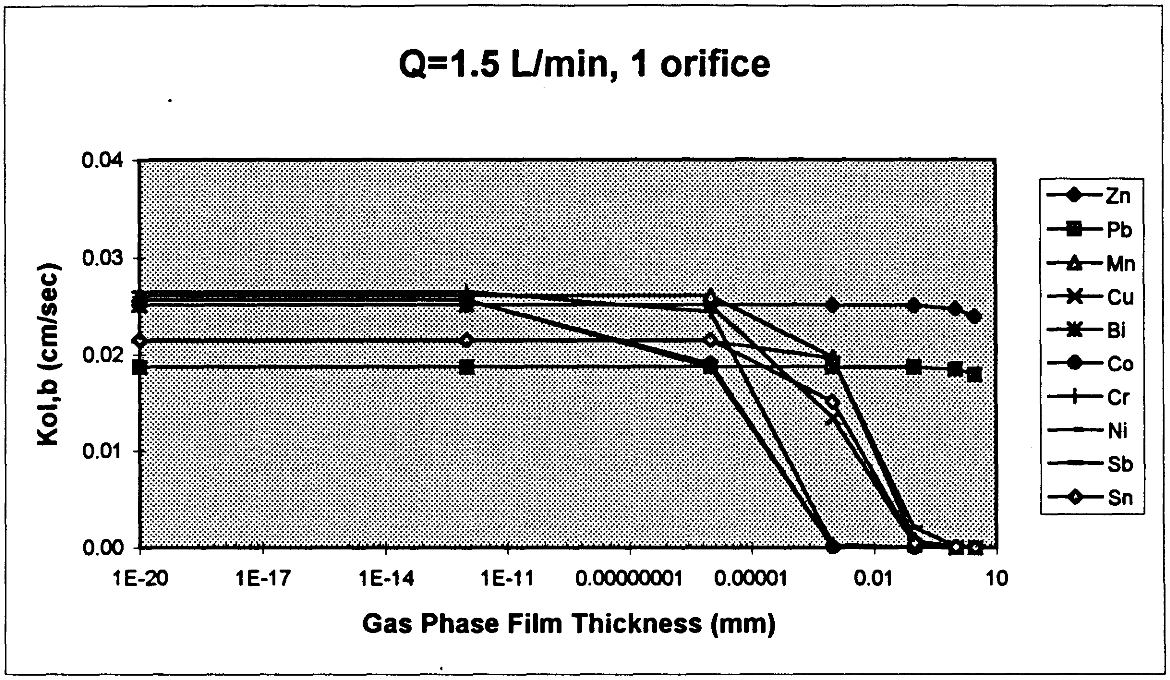

(1b)

Figure 19. Effect of the gas phase film thickness on the overall mass transfer coefficient in the bubbles in an iron melt.

### 3.1.4. Results and Discussion

With the theory given in the previous sections, the evaporation rates of several solutes in iron and copper melts are calculated. The required physical constants such as viscosity, surface tension, and density are obtained from common handbooks such as CRC [15]. Activity coefficients, vapor pressure data, and interaction coefficients are gotten from Sigworth and Elliott [16, 17], Hultgren et al. [18], and Kubaschewski et al. [19], and free energies of reaction are obtained from Turkdogan [20] and the software program HSC [21].

In the evaluation of the overall mass transfer coefficient for the bubbles ($K_{ol,b}$), a critical parameter to assess is the thickness of the gas boundary layer ($\delta_b$), which affects the gas phase mass transfer coefficient for the bubbles ($k_{g,b}$). This parameter was calculated to be about 2 mm by the two approaches presented in section 3.1.3.2. As a reference, Li et al. [22] estimated it at 3 mm for superficial gas impinging. Its effect on $K_{ol,b}$ becomes important when it is less than 1 mm, as shown in Figures 19 and 20 for iron and copper melts, respectively.

For the evaluation of $k_{g,ms}$, a gas temperature difference of 300 K was used for copper melts, which was experimentally determined. For iron melts, a temperature difference of 500 K was assumed due to their higher temperature.

Liquid phase mass transfer (represented by $k_l$) was found to control the evaporation of Zn, Pb, and Bi from molten iron through the bubbles and the top surface (see Figures 21-24). Gas phase mass transfer (represented by $k'_g$) determined the evaporation rate of the rest of the elements (also through both mechanisms) considered in each melt. In all cases, the relative importance of the liquid side resistance decreases in

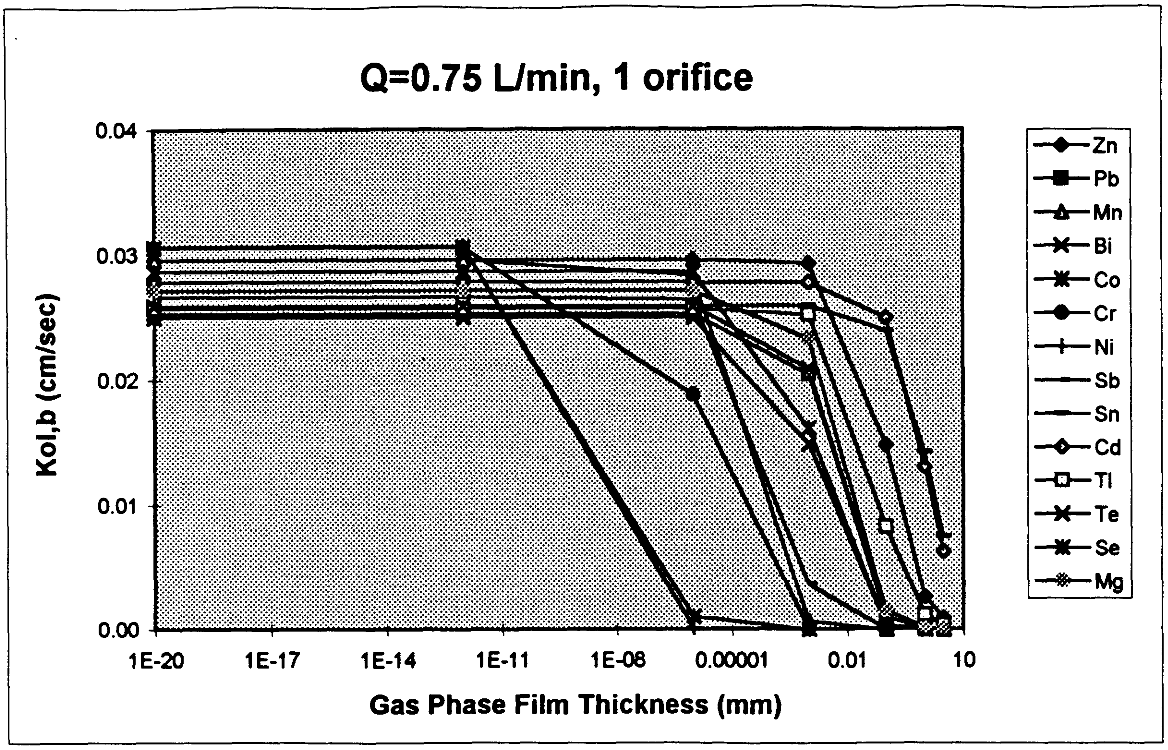

(2a)

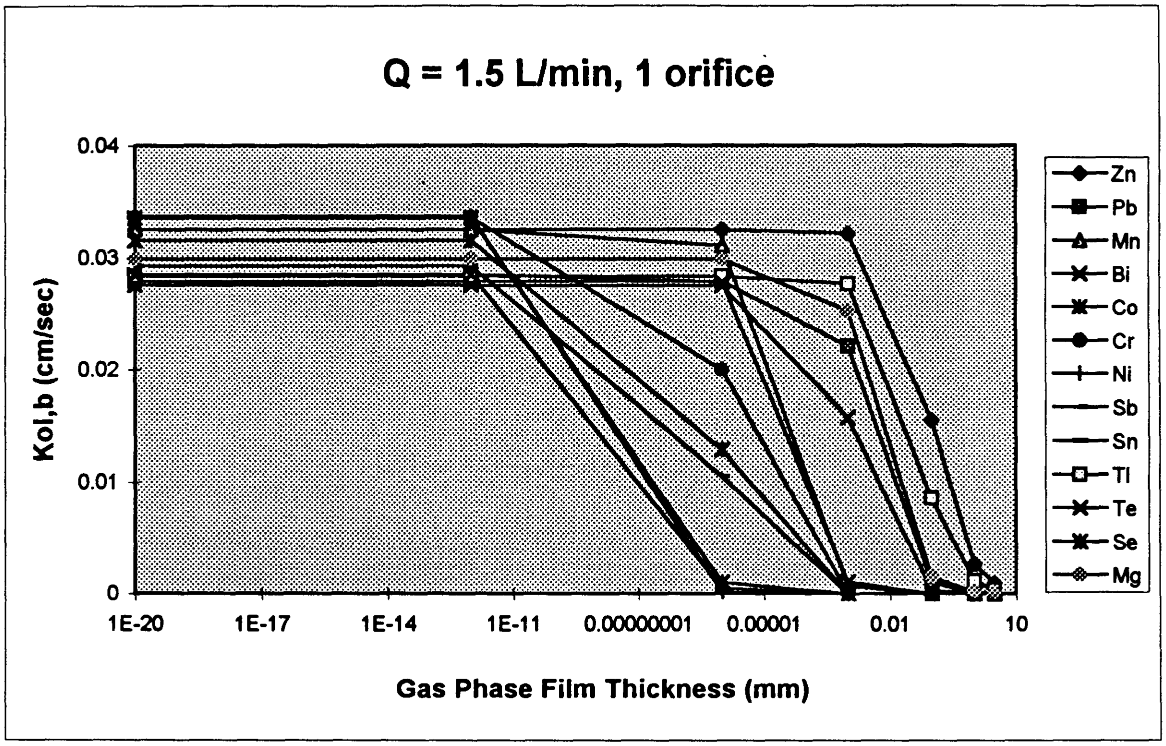

(2b)

Figure 20. Effect of the gas phase film thickness on the overall mass transfer coefficient in the bubbles in a copper melt.

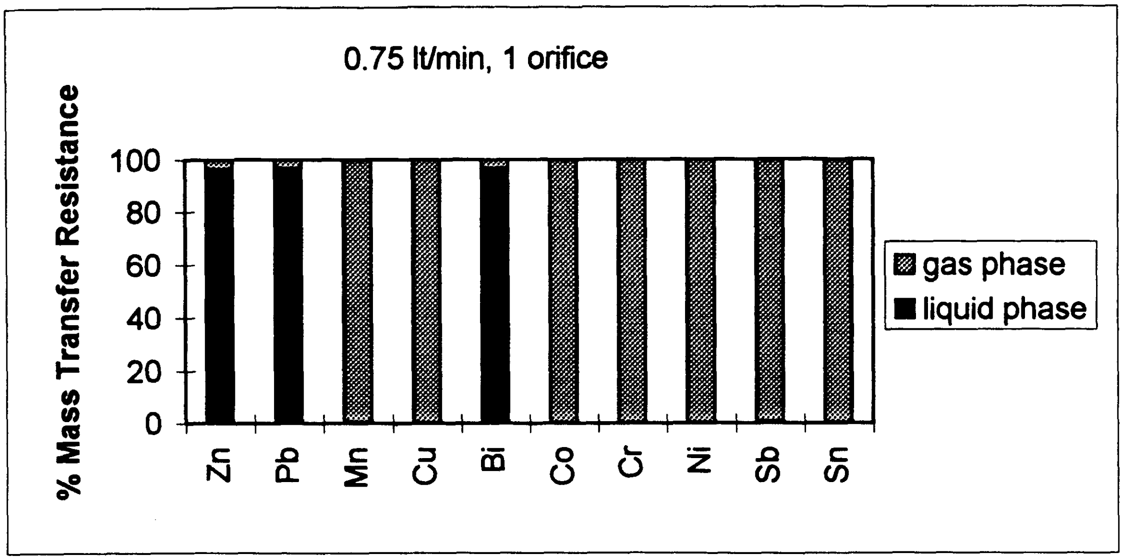

Figure 21. Contribution of the gas and liquid phases to the total mass transfer resistance in the bubbles in an iron melt.

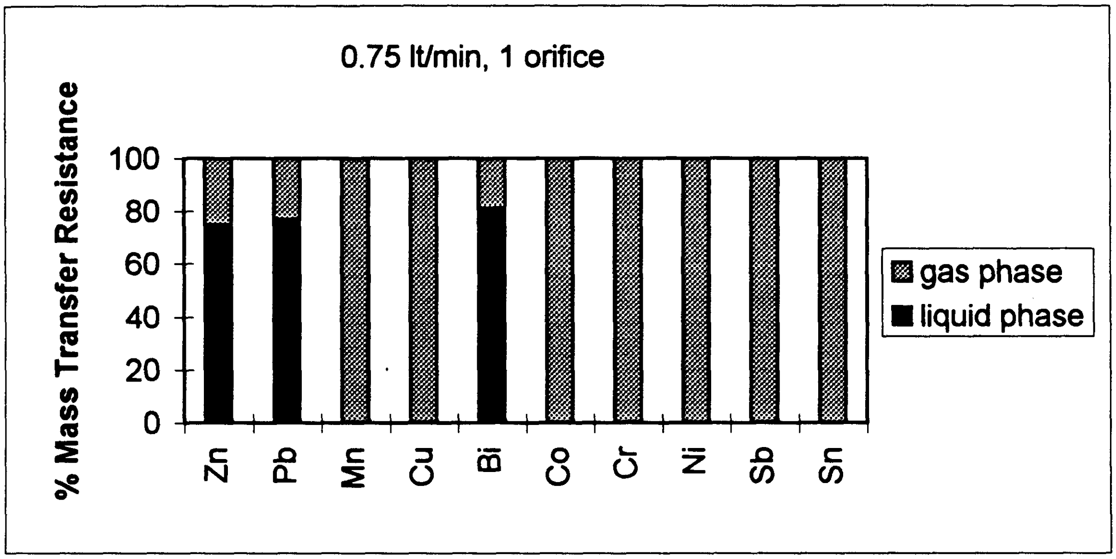

Figure 22. Contribution of the gas and liquid phases to the total mass transfer resistance in the melt surface in an iron melt.

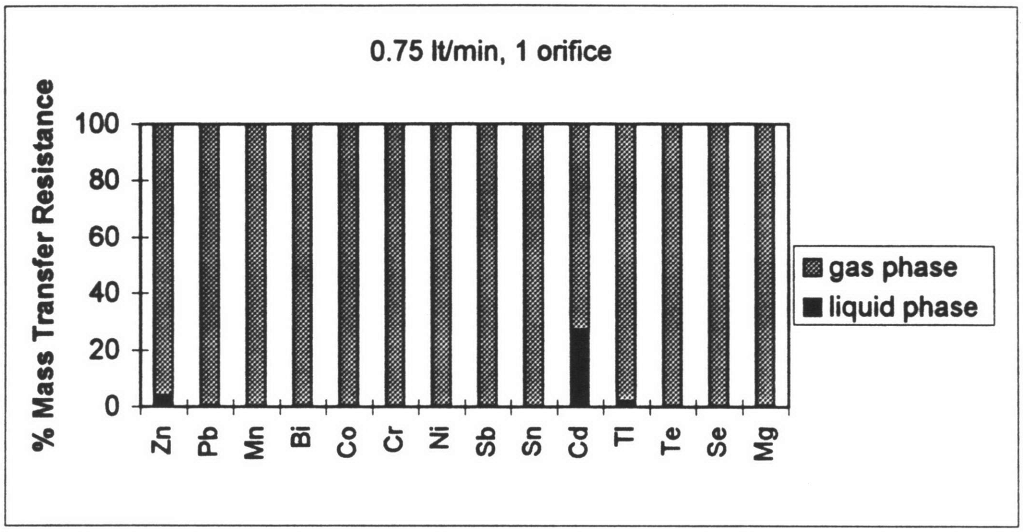

Figure 23. Contribution of the gas and liquid phases to the total mass transfer resistance in the bubbles in a copper melt.

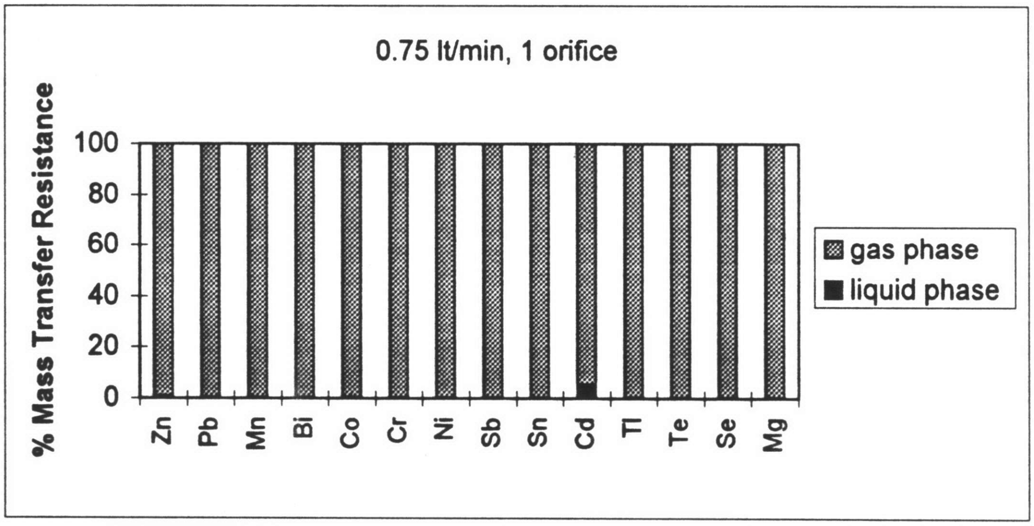

Figure 24. Contribution of the gas and liquid phases to the total mass transfer resistance in the melt surface in a copper melt.

the melt surface mechanism as compared to the bubbles, as the gas boundary layer above the melt surface is about seven times thicker than that in the bubbles. Although these charts consider a flow rate of 0.75 L/min, those for 1.5 L/min are very similar. As mentioned before, contribution of the interface mass transfer coefficient to the overall mass transfer coefficient can be considered negligible due to its high magnitude as compared to $k'_g$.

Whenever $k'_g$ is important in determining the evaporation rate, the product of vapor pressure times activity coefficient becomes critical, as these variables affect $k'_g$ significantly. The higher the value of the $\gamma P_{vap}$, the greater the increase of the liquid side resistance with respect to the gas side resistance. In copper melts, this product tends to be much lower than in iron melts partly because of the lower temperature involved (1473 K in copper vs. 1873 K in iron). This may explain the high contribution of $k'_g$ to the overall mass transfer resistance in copper melts. Thus, copper (at 1473 K) reduces the vaporization rate of most solutes (especially the ones that evaporate fastest in Fe), but it permits the conduction of experiments at a lower temperature. As an example, the liquid phase control of the evaporation rates of Zn, Pb, and Bi in molten Fe-3%C is due to the extremely high $\gamma P_{vap}$ products that these elements have at 1873 K. In iron, these products are 580, 985, and 929, respectively, while in copper (at 1473 K) they are 1.5, 0.1, and 0.03, which explains why the gas phase controls their evaporation in the latter case.

The effects of the argon injection rate and orifice diameter of the submerged lance on the individual and overall mass transfer coefficients were also studied. The argon injection rate was varied from 0.75 to 1.5 L/min and the orifice diameter from 1/4 to 3/4 inches. These ranges represent the practical operation limits of the existing induction furnace system. The results are shown in Tables 2 and 3 for iron and copper, respectively. It can be noted that the variation of $k_l$ and $k'_g$ is not very significant as far as their effect on $K_{ol}$ is concerned for all the elements considered. Thus, whenever either one is rate-determining it remains so, even if the above parameters are varied within the mentioned ranges.

It is not surprising to note that mass transfer coefficients are slightly lower when a 3/4" orifice is used instead of a 1/4" orifice. This is because, since larger bubbles are formed, the bubble contact time and gas boundary layer thickness increase and $k_l$ and $k_{g,b}$ decrease. Since the total bubble surface area also decreases, it is expected that the overall evaporation rate will also decrease.

When the flow rate is increased to 1.5 L/min, the mass transfer coefficients also decrease because of the reasons outlined above. However, the increase in total gas present inside the melt and in bubble surface area compensate this effect and so the overall evaporation rate actually increases.

The contribution of each evaporation mechanism to the total evaporation rate was also determined and is shown in Figures 25-28 for iron and copper melts at 0.75 and 1.5 L/min. It is clear that the bubble evaporation mechanism gains importance at the higher flow rate for the reasons mentioned above. It should also be noted that the relative contribution of melt surface evaporation slightly increases in iron melts. This is in part due to the higher convective mass transfer rates caused by the greater temperature difference in the gas above these melts.

# Table 2. Variation of Individual and Overall Mass Transfer Coefficients with Flow Rate and Orifice Number in an Iron Melt

| Total Flow (L/min) | | | | | 0.75 | | | | | 0.75 |
|---|---|---|---|---|---|---|---|---|---|---|
| Film Thickness (mm) | | | | | 2.1 | | | | | 2.4 |
| Bubble Diameter (mm) | | | | | 20 | | | | | 24 |
| Orifice Diam. (in) | | | | | 0.25 | | | | | 0.75 |
| Solute | kl (cm/s) | k'g,b (cm/s) | k'g,ms (cm/s) | Kol,b (cm/s) | Kol,ms (cm/s | kl (cm/s) | k'g,b (cm/s) | k'g,ms (cm/s) | Kol,b (cm/s) | Kol,ms (cm/s) |
| Zn | 0.0282 | 0.7377993 | 0.08412974 | **0.0271574** | **0.0211178** | 0.0253 | 0.662736 | 0.08412974 | **0.0243944** | **0.01946642** |
| Pb | 0.0210 | 0.5828586 | 0.07011844 | **0.0202879** | **0.01617171** | 0.0189 | 0.523559 | 0.07011844 | **0.0182238** | **0.01487545** |
| Mn | 0.0293 | 3.758E-05 | 4.7298E-06 | **3.753E-05** | **4.7291E-06** | 0.0263 | 3.38E-05 | 4.7298E-06 | **3.371E-05** | **4.729E-06** |
| Cu | 0.0282 | 1.351E-05 | 2.1077E-06 | **1.35E-05** | **2.1076E-06** | 0.0254 | 1.21E-05 | 2.1077E-06 | **1.213E-05** | **2.1076E-06** |
| Bi | 0.0210 | 0.586142 | 0.09146238 | **0.02025** | **0.0170619** | 0.0188 | 0.526508 | 0.09146238 | **0.0181898** | **0.01562253** |
| Co | 0.0288 | 3.438E-08 | 5.3647E-09 | **3.438E-08** | **5.3647E-09** | 0.0259 | 3.09E-08 | 5.3647E-09 | **3.088E-08** | **5.3647E-09** |
| Cr | 0.0297 | 1.476E-07 | 2.3025E-08 | **1.476E-07** | **2.3025E-08** | 0.0267 | 1.33E-07 | 2.3025E-08 | **1.325E-07** | **2.3025E-08** |
| Ni | 0.0288 | 3.174E-08 | 4.952E-09 | **3.174E-08** | **4.952E-09** | 0.0259 | 2.85E-08 | 4.952E-09 | **2.851E-08** | **4.952E-09** |
| Sb | 0.0240 | 0.0001062 | 1.6578E-05 | **0.0001058** | **1.6567E-05** | 0.0216 | 9.54E-05 | 1.6578E-05 | **9.501E-05** | **1.6566E-05** |
| Sn | 0.0242 | 2.376E-05 | 3.7082E-06 | **2.374E-05** | **3.7077E-06** | 0.0217 | 2.13E-05 | 3.7082E-06 | **2.133E-05** | **3.7076E-06** |

| Total Flow (L/min) | | | | | 1.5 | | | | | 1.5 |
|---|---|---|---|---|---|---|---|---|---|---|
| Film Thickness (mm) | | | | | 2.4 | | | | | 2.5 |
| Bubble Diameter (mm) | | | | | 24 | | | | | 30 |
| Orifice Diam. (in) | | | | | 0.25 | | | | | 0.75 |
| Solute | kl (cm/s) | k'g,b (cm/s) | k'g,ms (cm/s) | Kol,b (cm/s) | Kol,ms (cm/s | kl (cm/s) | k'g,b (cm/s) | k'g,ms (cm/s) | Kol,b (cm/s) | Kol,ms (cm/s) |
| Zn | 0.0251 | 0.6571963 | 0.08412974 | **0.0241905** | **0.01934111** | 0.0241 | 0.629983 | 0.08412974 | **0.0231888** | **0.01871842** |
| Pb | 0.0187 | 0.5191826 | 0.07011844 | **0.0180715** | **0.01477732** | 0.0179 | 0.497684 | 0.07011844 | **0.0173232** | **0.01429011** |
| Mn | 0.0261 | 3.347E-05 | 4.7298E-06 | **3.343E-05** | **4.729E-06** | 0.0250 | 3.21E-05 | 4.7298E-06 | **3.204E-05** | **4.7289E-06** |
| Cu | 0.0252 | 1.203E-05 | 2.1077E-06 | **1.203E-05** | **2.1076E-06** | 0.0241 | 1.15E-05 | 2.1077E-06 | **1.153E-05** | **2.1076E-06** |
| Bi | 0.0187 | 0.5221072 | 0.09146238 | **0.0180377** | **0.0155141** | 0.0179 | 0.500487 | 0.09146238 | **0.0172908** | **0.01497688** |
| Co | 0.0256 | 3.062E-08 | 5.3647E-09 | **3.062E-08** | **5.3647E-09** | 0.0246 | 2.94E-08 | 5.3647E-09 | **2.936E-08** | **5.3647E-09** |
| Cr | 0.0265 | 1.314E-07 | 2.3025E-08 | **1.314E-07** | **2.3025E-08** | 0.0254 | 1.26E-07 | 2.3025E-08 | **1.26E-07** | **2.3025E-08** |
| Ni | 0.0257 | 2.827E-08 | 4.952E-09 | **2.827E-08** | **4.952E-09** | 0.0246 | 2.71E-08 | 4.952E-09 | **2.71E-08** | **4.952E-09** |
| Sb | 0.0214 | 9.464E-05 | 1.6578E-05 | **9.422E-05** | **1.6565E-05** | 0.0205 | 9.07E-05 | 1.6578E-05 | **9.032E-05** | **1.6565E-05** |
| Sn | 0.0215 | 2.117E-05 | 3.7082E-06 | **2.115E-05** | **3.7076E-06** | 0.0206 | 2.03E-05 | 3.7082E-06 | **2.027E-05** | **3.7076E-06** |

## Table 3. Variation of Individual and Overall Mass Transfer Coefficients with Flow Rate and Orifice Number in a Copper Melt

| Total Flow (lt/min) | | | | | 0.75 | | | | | 0.75 |
|---|---|---|---|---|---|---|---|---|---|---|
| Film Thickness (mm) | | | | | 2 | | | | | 2.1 |
| Bubble Diameter (mm) | | | | | 18 | | | | | 22 |
| Orifice Diam. (in) | | | | | 0.25 | | | | | 0.75 |
| Solute | kl (cm/s) | k'g,b (cm/s) | k'g,ms (cm/s) | Kol,b (cm/s) | Kol,ms (cm/s | kl (cm/s) | k'g,b (cm/s | k'g,ms (cm/s) | Kol,b (cm/s) | Kol,ms (cm/s) |
| Zn | 0.0344 | 0.0014481 | 0.00022274 | **0.0013897** | **0.00022131** | 0.0339 | 0.001425 | 0.00022274 | **0.0013678** | **0.00022128** |
| Pb | 0.0295 | 5.208E-05 | 8.0098E-06 | **5.198E-05** | **8.0076E-06** | 0.0290 | 5.13E-05 | 8.0098E-06 | **5.117E-05** | **8.0075E-06** |
| Mn | 0.0344 | 3.362E-07 | 5.1718E-08 | **3.362E-07** | **5.1718E-08** | 0.0339 | 3.31E-07 | 5.1718E-08 | **3.31E-07** | **5.1718E-08** |
| Bi | 0.0291 | 1.792E-05 | 2.7561E-06 | **1.791E-05** | **2.7559E-06** | 0.0286 | 1.76E-05 | 2.7561E-06 | **1.763E-05** | **2.7558E-06** |
| Co | 0.0355 | 5.356E-10 | 8.2385E-11 | **5.356E-10** | **8.2385E-11** | 0.0350 | 5.27E-10 | 8.2385E-11 | **5.272E-10** | **8.2385E-11** |
| Cr | 0.0355 | 2.409E-08 | 3.706E-09 | **2.409E-08** | **3.706E-09** | 0.0350 | 2.37E-08 | 3.706E-09 | **2.372E-08** | **3.706E-09** |
| Ni | 0.0357 | 8.804E-11 | 1.3541E-11 | **8.804E-11** | **1.3541E-11** | 0.0351 | 8.67E-11 | 1.3541E-11 | **8.666E-11** | **1.3541E-11** |
| Sb | 0.0310 | 7.98E-09 | 1.2274E-09 | **7.98E-09** | **1.2274E-09** | 0.0305 | 7.85E-09 | 1.2274E-09 | **7.854E-09** | **1.2274E-09** |
| Sn | 0.0302 | 2.501E-10 | 3.8464E-11 | **2.501E-10** | **3.8464E-11** | 0.0297 | 2.46E-10 | 3.8464E-11 | **2.461E-10** | **3.8464E-11** |
| Cd | 0.0323 | 0.0120294 | 0.00185025 | **0.008768** | **0.00175012** | 0.0318 | 0.011841 | 0.00185025 | **0.0086304** | **0.00174861** |
| Tl | 0.0299 | 0.0005993 | 9.2173E-05 | **0.0005875** | **9.189E-05** | 0.0295 | 0.00059 | 9.2173E-05 | **0.0005783** | **9.1886E-05** |
| Te | 0.0301 | 5.556E-07 | 8.5462E-08 | **5.556E-07** | **8.5462E-08** | 0.0297 | 5.47E-07 | 8.5462E-08 | **5.469E-07** | **8.5462E-08** |
| Se | 0.0333 | 1.061E-08 | 1.6325E-09 | **1.061E-08** | **1.6325E-09** | 0.0328 | 1.04E-08 | 1.6325E-09 | **1.045E-08** | **1.6325E-09** |
| Mg | 0.0316 | 7.951E-05 | 1.223E-05 | **7.931E-05** | **1.2225E-05** | 0.0311 | 7.83E-05 | 1.223E-05 | **7.807E-05** | **1.2225E-05** |

| Total Flow (lt/min) | | | | | 1.5 | | | | | 1.5 |
|---|---|---|---|---|---|---|---|---|---|---|
| Film Thickness (mm) | | | | | 2.2 | | | | | 2.3 |
| Bubble Diameter (mm) | | | | | 23 | | | | | 27 |
| Orifice Diam. (in) | | | | | 0.25 | | | | | 0.75 |
| Solute | kl (cm/s) | k'g,b (cm/s) | k'g,ms (cm/s) | Kol,b (cm/s) | Kol,ms (cm/s | kl (cm/s) | k'g,b (cm/s | k'g,ms (cm/s) | Kol,b (cm/s) | Kol,ms (cm/s) |
| Zn | 0.0326 | 0.0013703 | 0.00022274 | **0.001315** | **0.00022123** | 0.0310 | 0.001304 | 0.00022274 | **0.0012509** | **0.00022115** |
| Pb | 0.0279 | 4.928E-05 | 8.0098E-06 | **4.919E-05** | **8.0075E-06** | 0.0265 | 4.69E-05 | 8.0098E-06 | **4.679E-05** | **8.0073E-06** |
| Mn | 0.0326 | 3.182E-07 | 5.1718E-08 | **3.182E-07** | **5.1718E-08** | 0.0310 | 3.03E-07 | 5.1718E-08 | **3.027E-07** | **5.1718E-08** |
| Bi | 0.0275 | 1.696E-05 | 2.7561E-06 | **1.695E-05** | **2.7558E-06** | 0.0262 | 1.61E-05 | 2.7561E-06 | **1.612E-05** | **2.7558E-06** |
| Co | 0.0336 | 5.068E-10 | 8.2385E-11 | **5.068E-10** | **8.2385E-11** | 0.0320 | 4.82E-10 | 8.2385E-11 | **4.822E-10** | **8.2385E-11** |
| Cr | 0.0336 | 2.28E-08 | 3.706E-09 | **2.28E-08** | **3.706E-09** | 0.0320 | 2.17E-08 | 3.706E-09 | **2.169E-08** | **3.706E-09** |
| Ni | 0.0337 | 8.331E-11 | 1.3541E-11 | **8.331E-11** | **1.3541E-11** | 0.0321 | 7.93E-11 | 1.3541E-11 | **7.925E-11** | **1.3541E-11** |
| Sb | 0.0293 | 7.551E-09 | 1.2274E-09 | **7.551E-09** | **1.2274E-09** | 0.0279 | 7.18E-09 | 1.2274E-09 | **7.183E-09** | **1.2274E-09** |
| Sn | 0.0285 | 2.366E-10 | 3.8464E-11 | **2.366E-10** | **3.8464E-11** | 0.0272 | 2.25E-10 | 3.8464E-11 | **2.251E-10** | **3.8464E-11** |
| Cd | 0.0306 | 0.0113829 | 0.00185025 | **0.0082968** | **0.00174476** | 0.0291 | 0.010828 | 0.00185025 | **0.0078927** | **0.00173968** |
| Tl | 0.0283 | 0.0005671 | 9.2173E-05 | **0.0005559** | **9.1874E-05** | 0.0269 | 0.000539 | 9.2173E-05 | **0.0005289** | **9.1859E-05** |
| Te | 0.0285 | 5.258E-07 | 8.5462E-08 | **5.258E-07** | **8.5462E-08** | 0.0271 | 5E-07 | 8.5462E-08 | **5.002E-07** | **8.5462E-08** |
| Se | 0.0316 | 1.004E-08 | 1.6325E-09 | **1.004E-08** | **1.6325E-09** | 0.0300 | 9.55E-09 | 1.6325E-09 | **9.554E-09** | **1.6325E-09** |
| Mg | 0.0299 | 7.524E-05 | 1.223E-05 | **7.505E-05** | **1.2225E-05** | 0.0285 | 7.16E-05 | 1.223E-05 | **7.14E-05** | **1.2225E-05** |

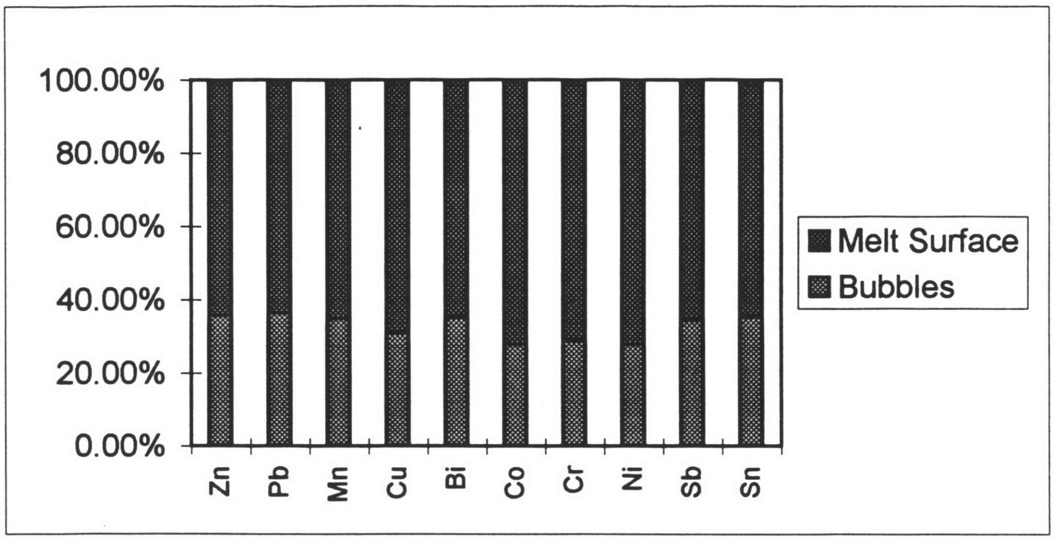

Figure 25. Contribution of individual mechanisms to the overall evaporation of solutes from molten iron. (T= 1873 K, gas flow = 0.75 L/min, single 1/4" OD orifice)

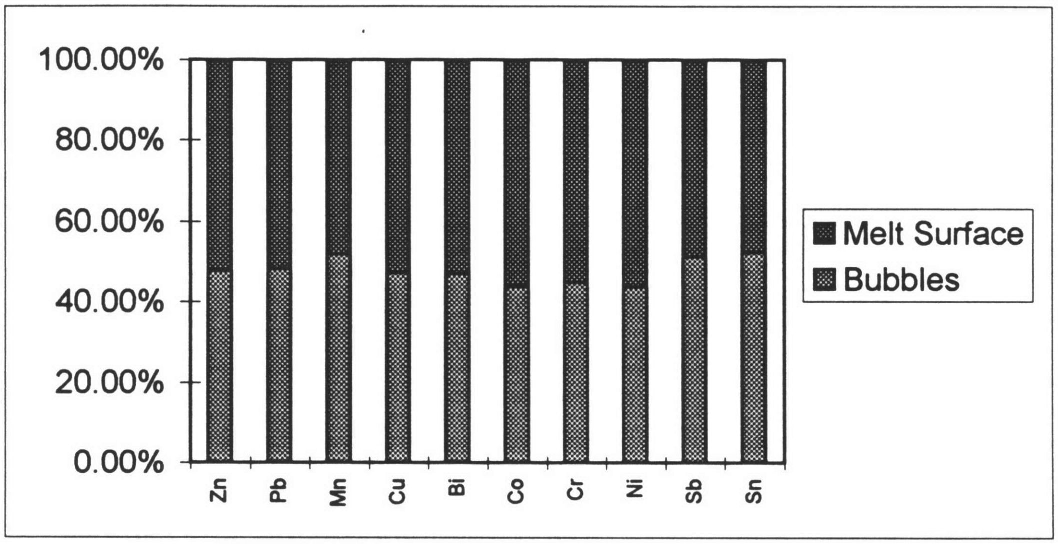

Figure 26. Contribution of individual mechanisms to the overall evaporation of solutes from molten iron. (T= 1873 K, gas flow = 1.5 L/min, single 1/4" OD orifice)

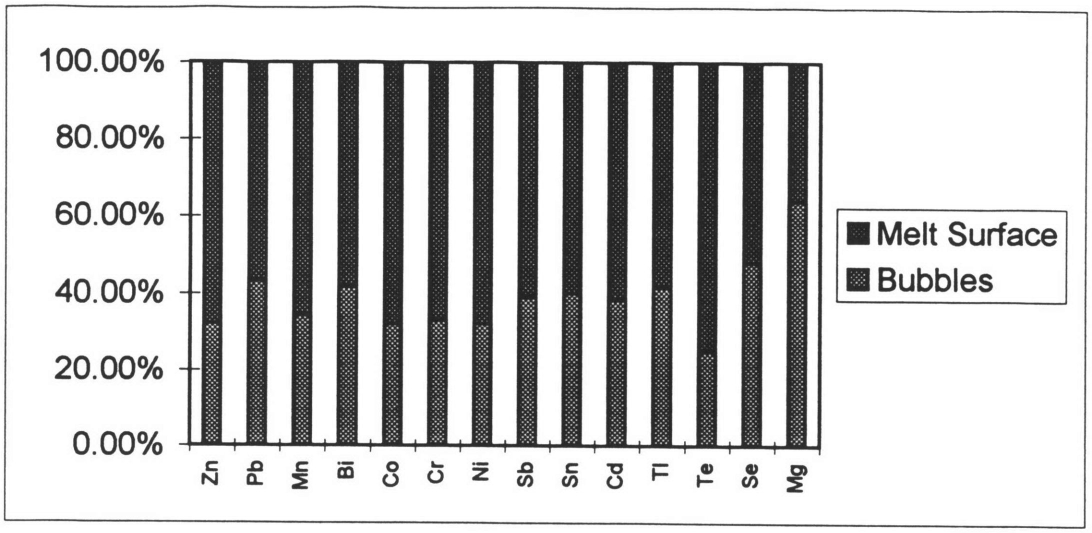

Figure 27. Contribution of individual mechanisms to the overall evaporation of solutes from molten copper. (T= 1473 K, gas flow = 0.75 L/min, single 1/4" OD orifice)

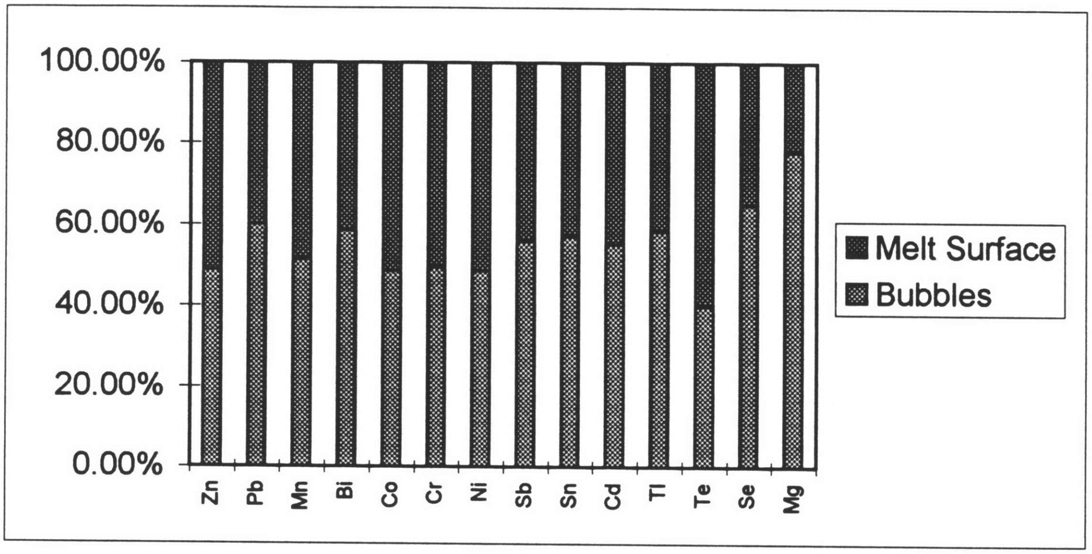

Figure 28. Contribution of individual mechanisms to the overall evaporation of solutes from molten copper. (T= 1473 K, gas flow = 1.5 L/min, single 1/4" OD orifice)

The evaporation of impurities from iron and copper melts has been reported in several studies in the literature [2, 3, 5, 6, 8, 24, 25]. However, most of these studies were carried out under vacuum conditions or with gas impinging. A recent study by Li [22] under atmospheric pressure reported a value of $k_l$ in agreement with those found by these calculations. In addition, several studies have reported that gas phase mass transfer is generally the rate-determining step for many elements in copper melts [23, 24, 25].

The calculated values of $K_{ol}$, $K_{eq}$ , and the previously mentioned mass transfer equations were used to obtain the evaporation rates at 0.75 and 1.5 L/min of all the solute elements considered. These are plotted in Figures 29-36. In an iron melt, Bi, Pb, and Zn evaporate very rapidly, due to their high $\gamma P_{vap}$ products. Since these products are much lower in copper, their evaporation rates decrease dramatically as well. In both iron and copper melts, the higher gas flow rate gives higher evaporation rates due to the reasons discussed above. This effect is more noticeable in copper melts because the bubbles contribute more to the total rate of evaporation in these cases.

The evaporation of the solute through the melt surface can be virtually eliminated by covering the melt with a slag layer in which the solute has a very low solubility. In the cases where equilibrium is achieved in the bubbles (i.e., when $\phi_A > 3$), the experiments would provide the value of $K_{eq}$, the equilibrium constant. All other cases would give the value of $K_{ol,b}$, the overall mass transfer coefficient for the bubbles. In an identical experiment without the slag (in which both evaporation into the bubbles and through the top surface occur), the mass transfer coefficient for the melt surface, $K_{ol,ms}$, could be evaluated.

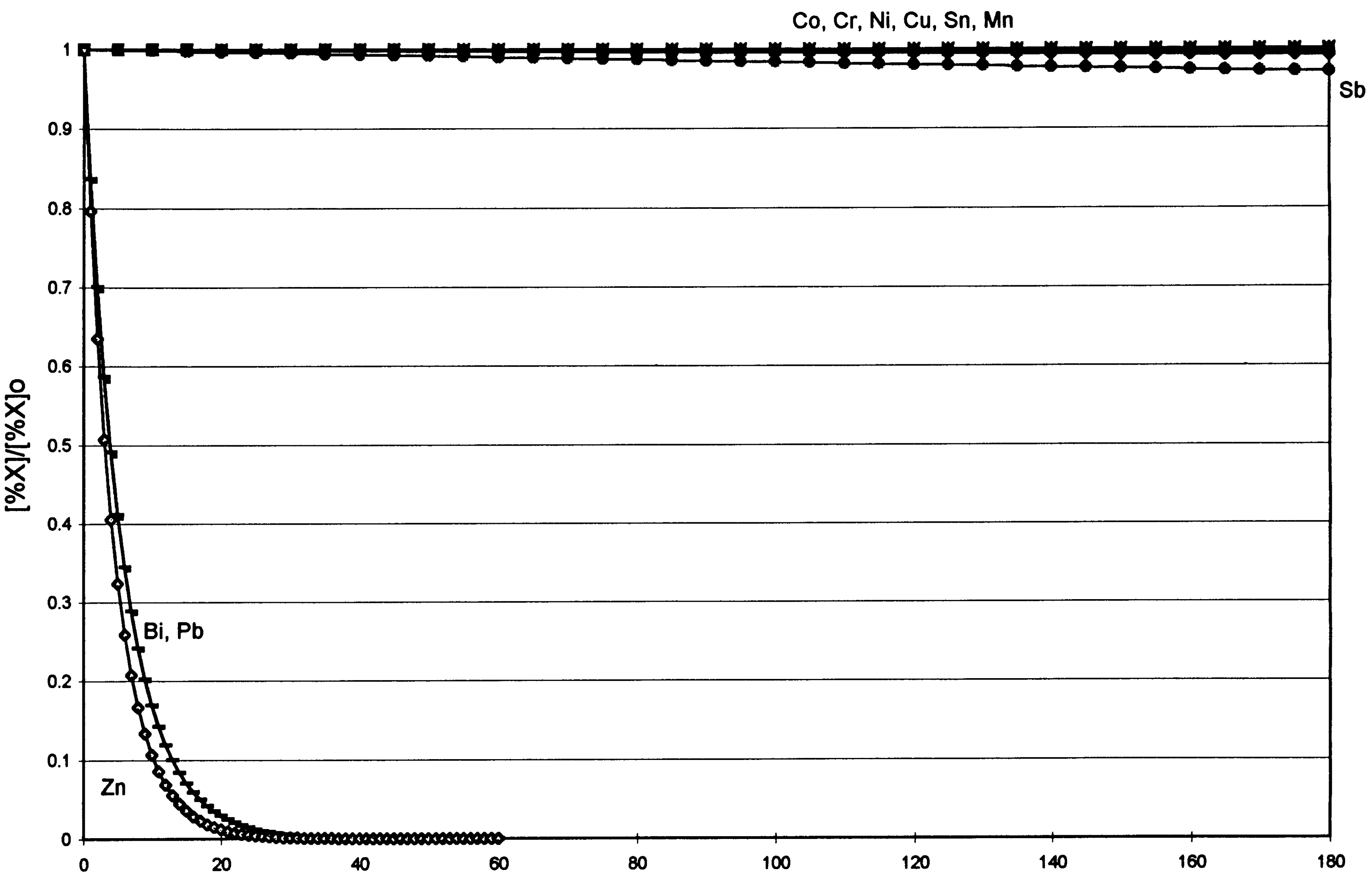

Figure 29. Evaporation of solutes from iron.
(T=1873 K, Q=0.75 L/min, single 1/4" OD orifice)

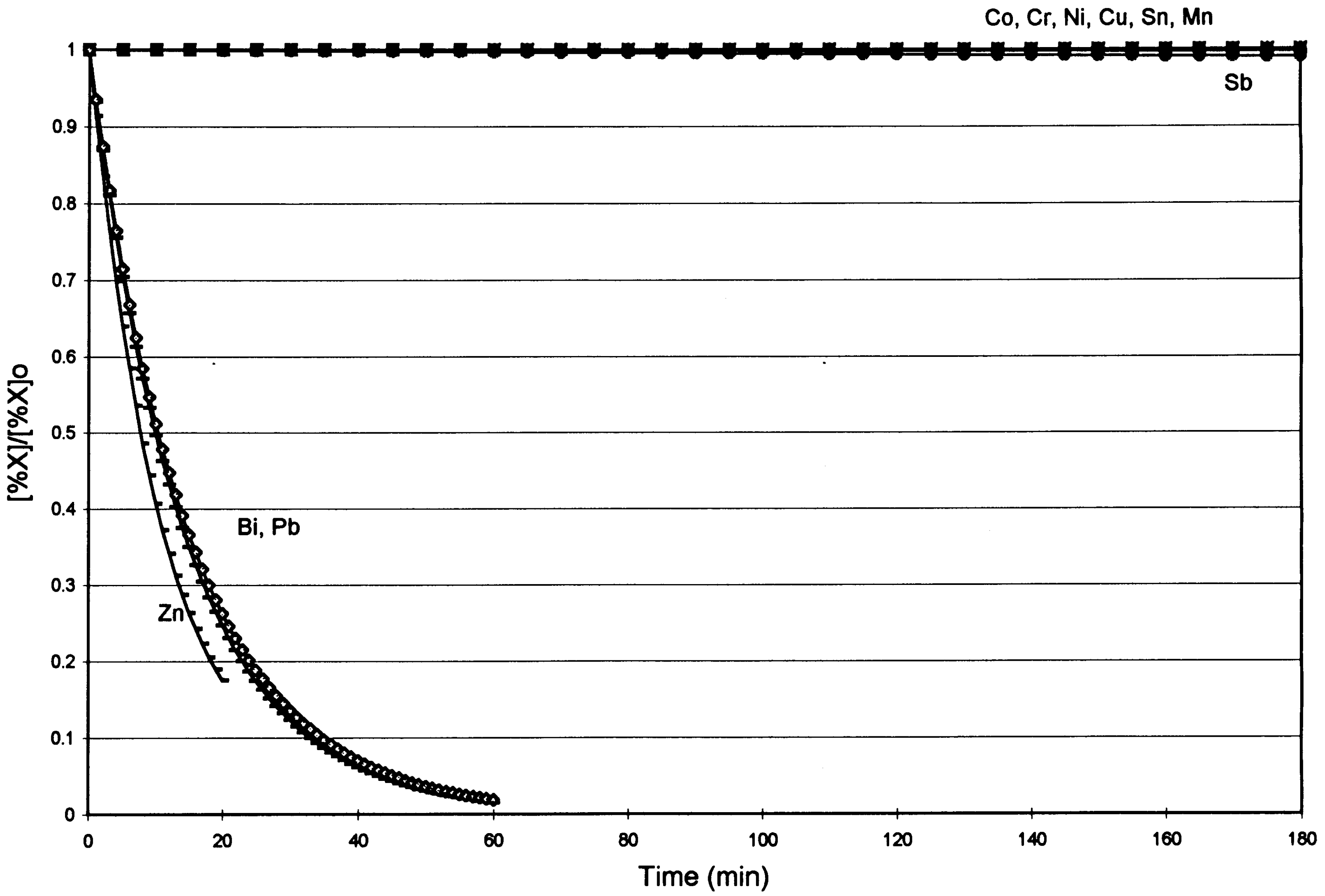

Figure 30. Evaporation of solutes from iron with a slag layer.
(T=1873 K, Q=0.75 L/min, single 1/4" OD orifice)

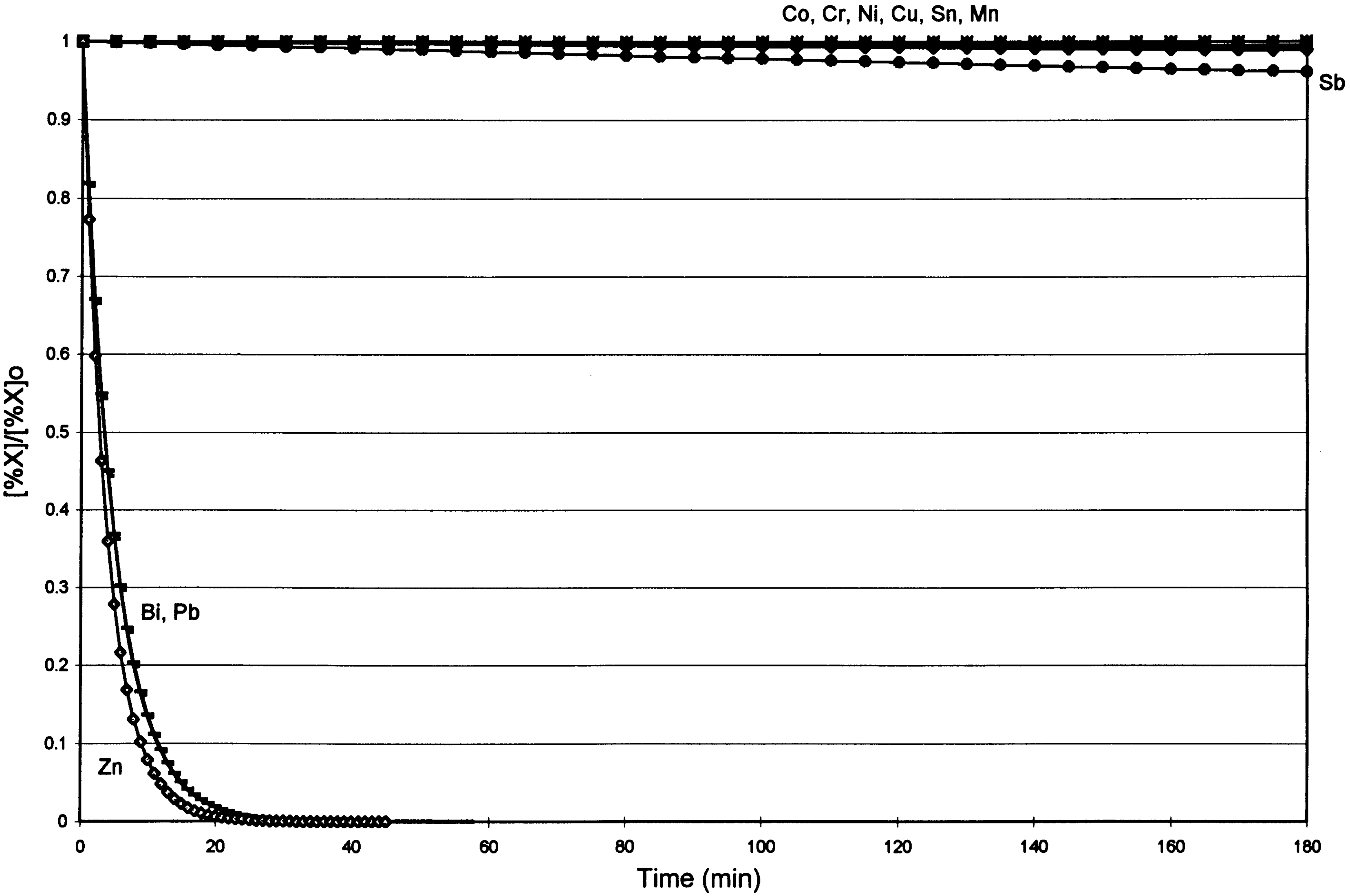

Figure 31. Evaporation of solutes from iron.
(T=1873 K, Q=1.5 L/min, single 1/4" OD orifice)

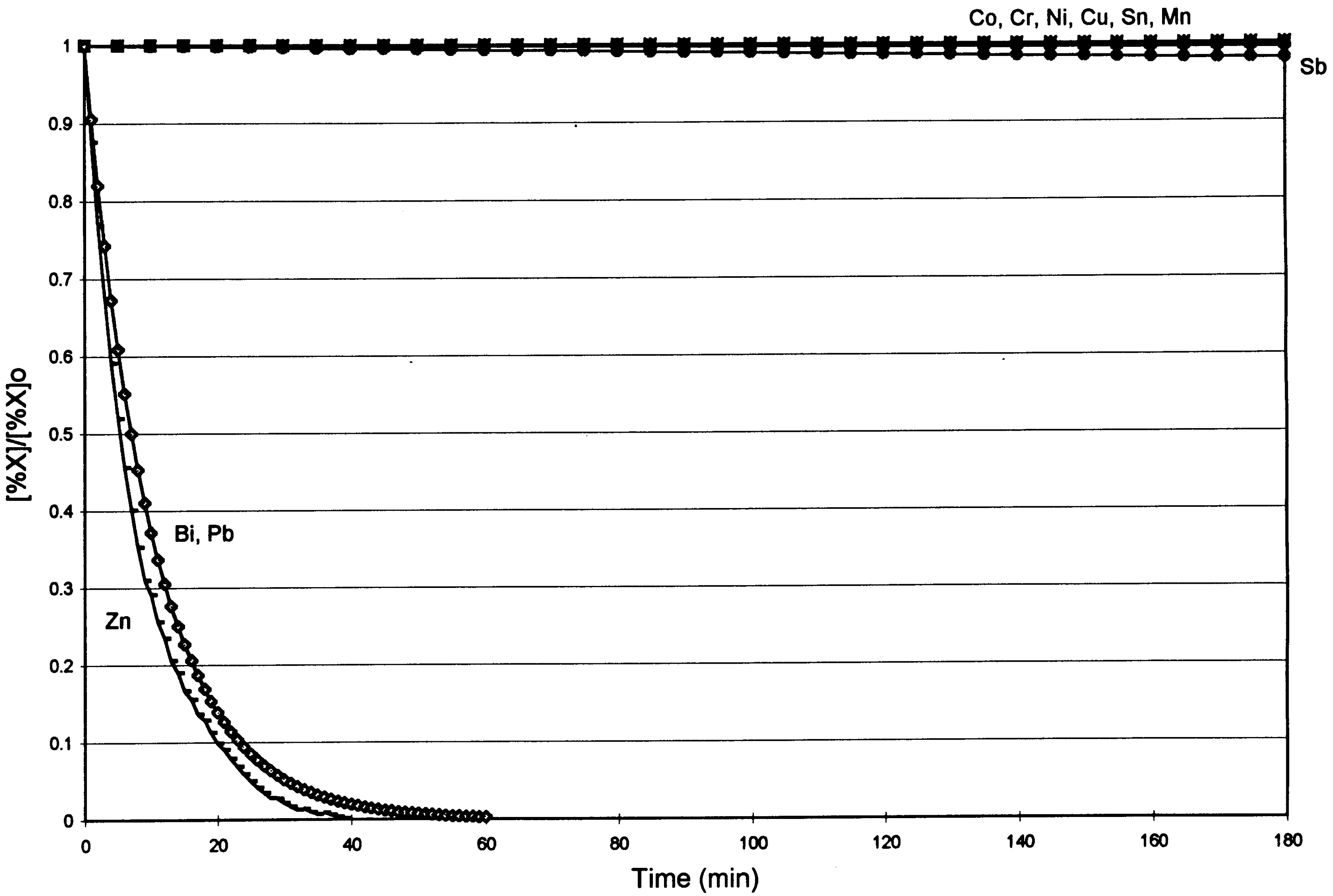

Figure 32. Evaporation of solutes from iron with a slag layer.
(T=1873 K, Q=1.5 L/min, single 1/4" OD orifice)

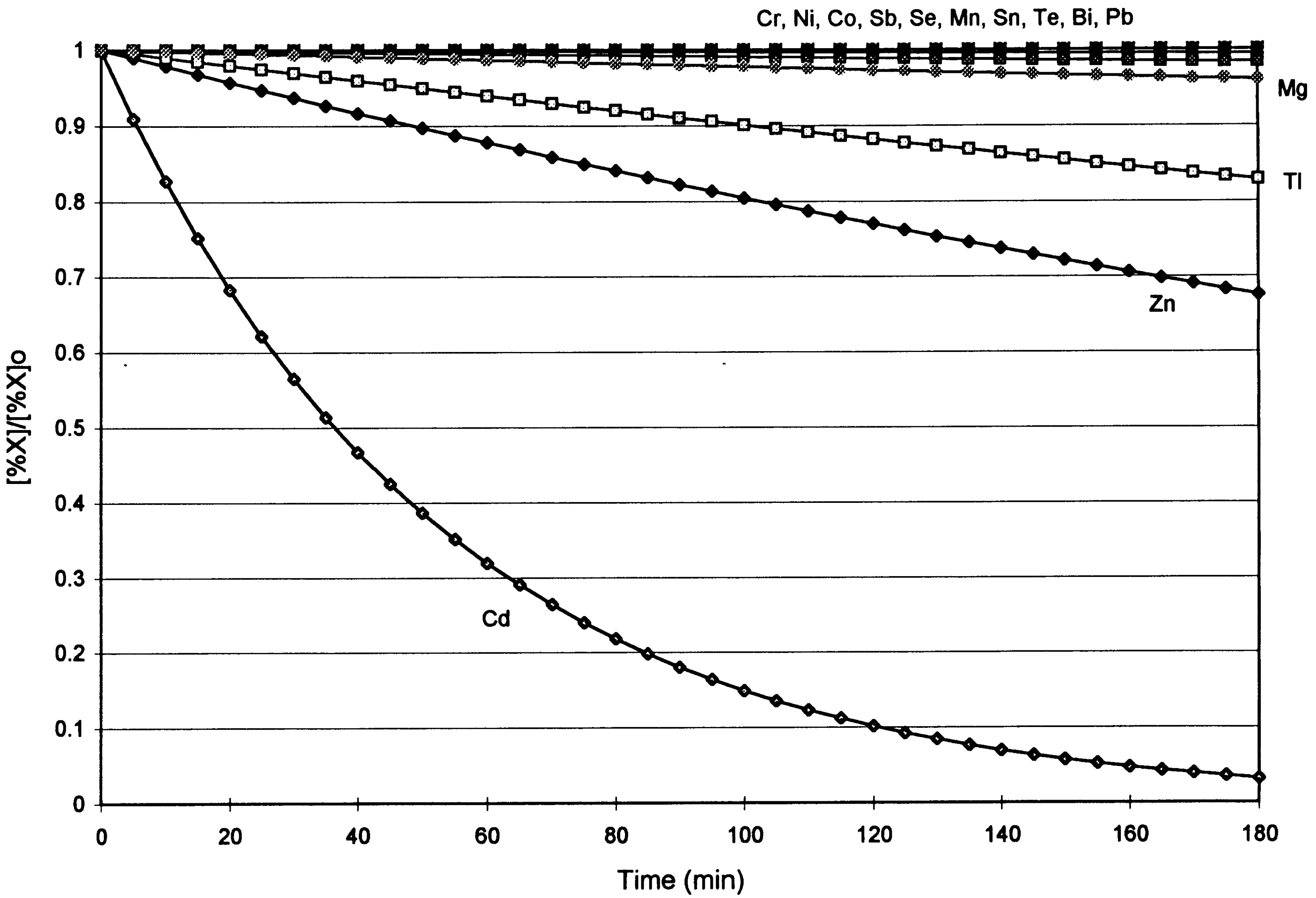

Figure 33. Evaporation of solutes from copper.
(T= 1473 K, Q=0.75 L/min, single 1/4" O.D. orifice)

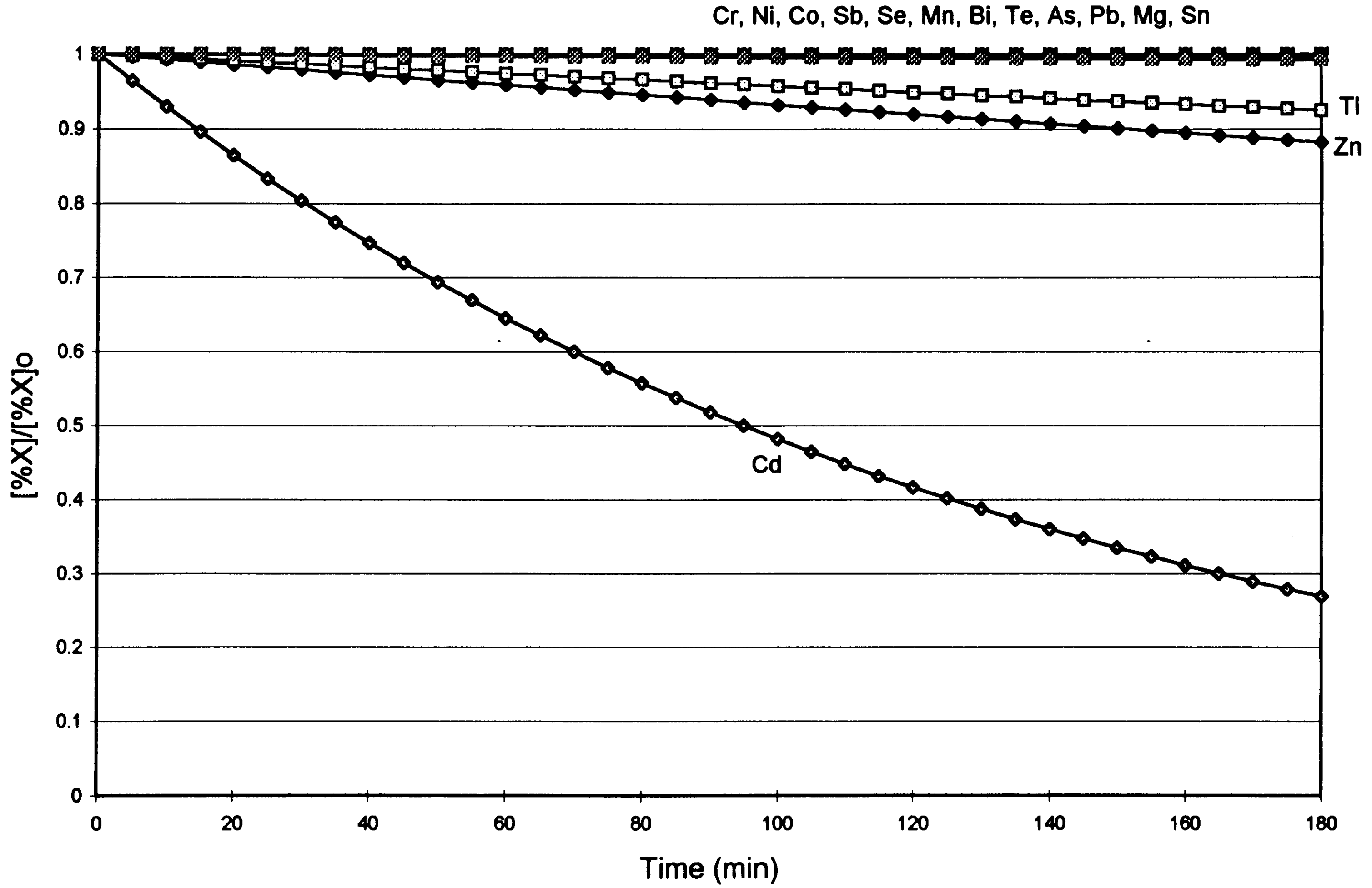

Figure 34. Evaporation of solutes from copper with a slag layer.
(T= 1473 K, Q=0.75 L/min, single 1/4" O.D. orifice)

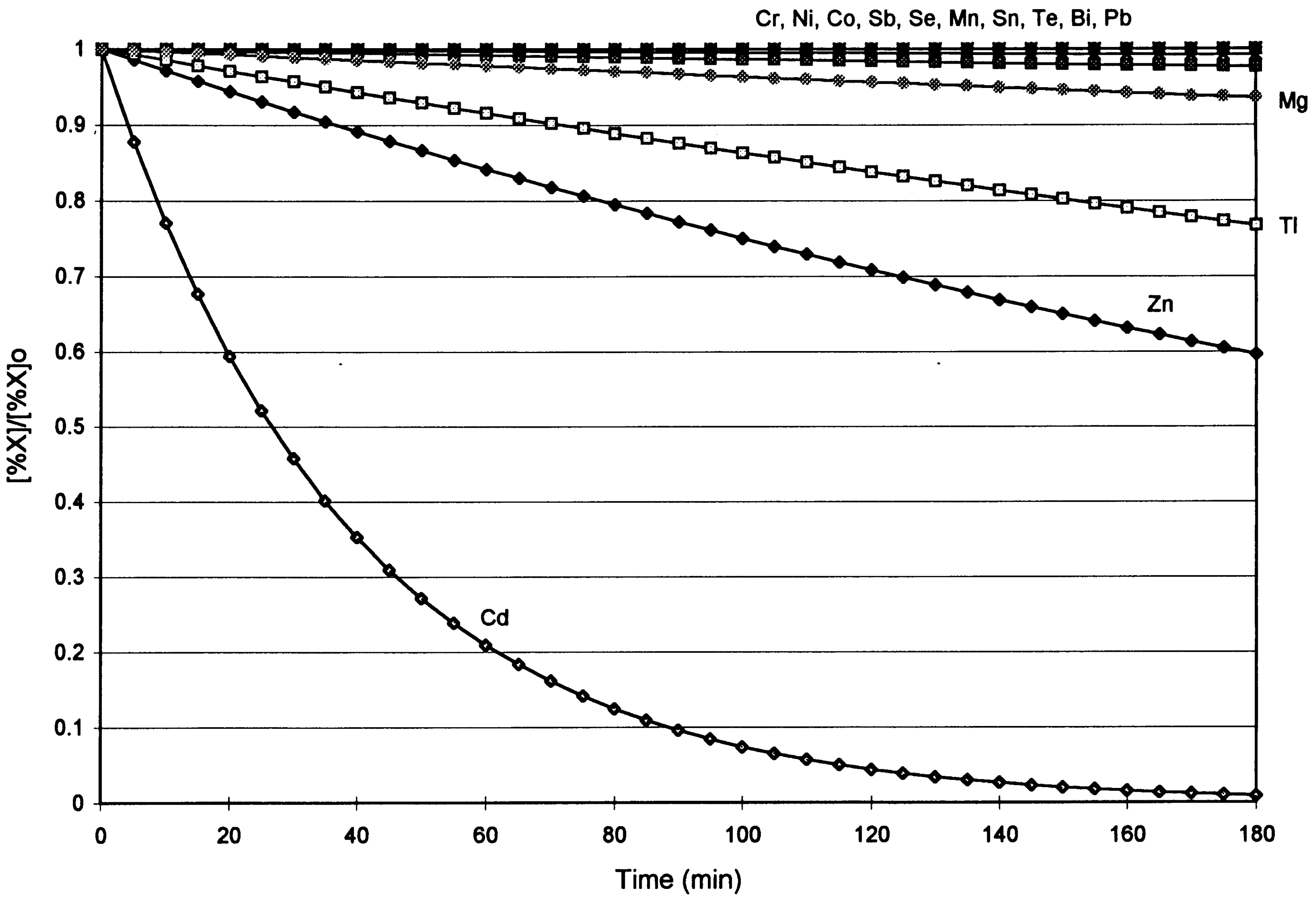

Figure 35. Evaporation of solutes from copper.
(T= 1473 K, Q=1.5 L/min, single 1/4" O.D. orifice)

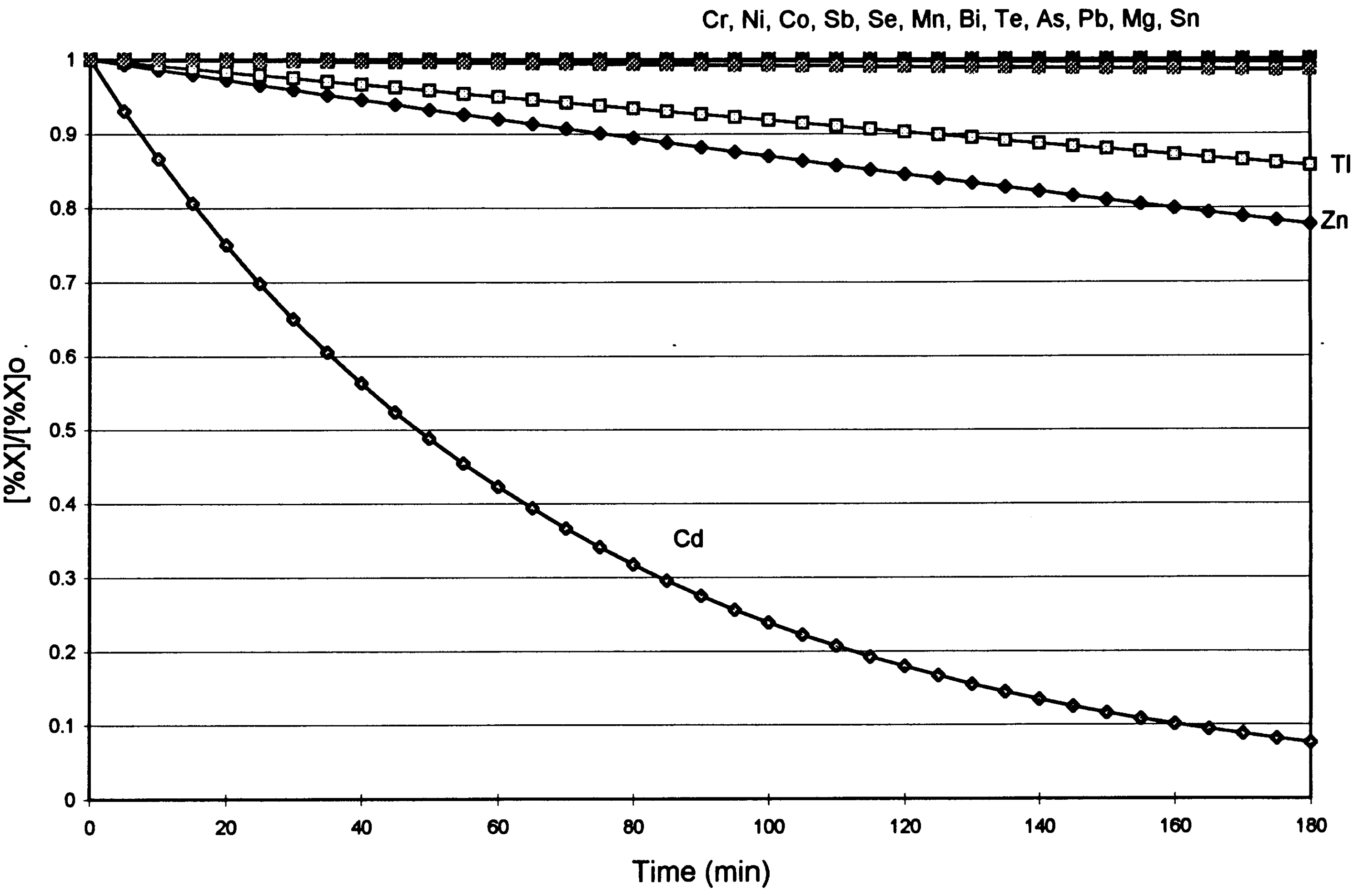

Figure 36. Evaporation of solutes from copper with a slag layer.
(T= 1473 K, Q=1.5 L/min, single 1/4" O.D. orifice)

### 3.2. Aerosol Formation Mechanisms

The aerosol leaving a melt is formed by entrainment and vaporization as shown schematically in Figure 37. The entrained particles are produced by the breakup of bubbles at the melt surface and range in size from 5 to 100 µm. Vaporized components may do any of the following within the aerosol:

1. condense on the surfaces of the entrained particles
2. nucleate to form condensate particles that can grow by coagulation to sizes in the range of 0.03 to 1 µm
3. escape as vapors

The magnitudes of these three routes can be altered by varying the cooling rate of the product gases and the total surface area of entrained particles. For example, nucleation of submicron particles is favored by fast cooling rates and low surface area of entrained particles.

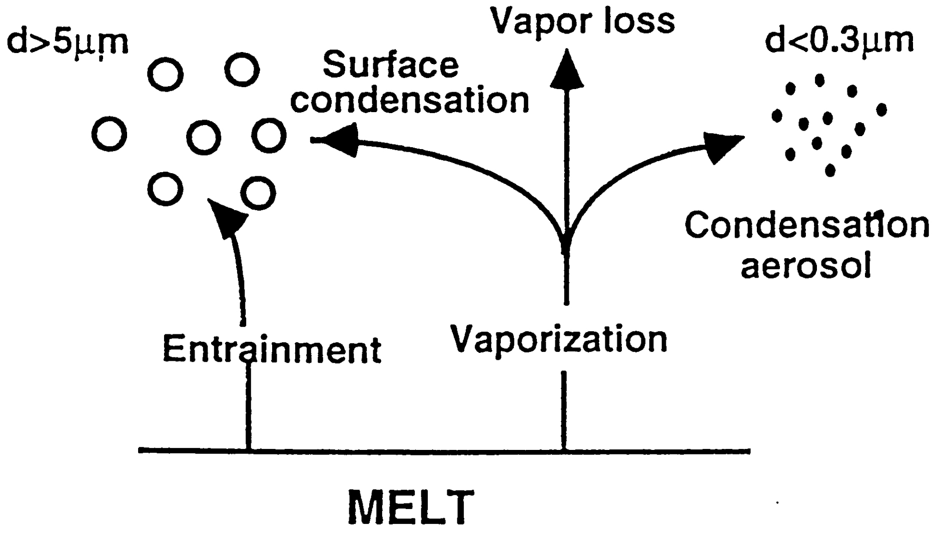

Figure 37. Possible aerosol formation mechanisms above a melt surface.

In our case, the aerosol leaving the melt is thought to form in the following way:

1. homogeneous nucleation of Cd particles at the sampling probe entrance (there is no time for significant condensation on the entrained Cu particles due to the fast quenching rate)
2. polydisperse coagulation between Cd particles and entrained Cu particles

The fact that there is negligible condensation on the entrained Cu particles is supported by the relative concentrations of Cd in +18 μm and +3.2/-18 μm particles. If there were only condensation, then the Cd concentrations would vary as the inverse of the squares of the particle diameters. This is because the surface area per unit volume and the mass transfer coefficient both vary as $1/d$, and the condensed Cd concentration depends on the product of the two, so it varies as $1/d^2$. Thus, the Cd concentration in the +18 μm particles should be about 25 times lower than that in the +3.2/-18 μm particles. However, it was experimentally found that the ratio was 1:1.5 to 1:2 instead of 1:25. Furthermore, the SEM micrographs shown in section 2.5.2 give evidence for coagulation between small Cd particles and large entrained particles. Therefore, it can be concluded that most of the Cd in the entrained particles is due to coagulation rather than condensation.

### 3.2.1. Calculation of the Diameter of Average Mass

In order to calculate an average diameter of the final aerosol, two assumptions were made:

1. the saturation ratio, defined as $S=P_{Cd}/P_{Cd,sat}$, is constant at a value of 10 (typical value for pure substances) [27]
2. the diameter of the large entrained particles does not change significantly during coagulation

The critical nucleus size is calculated from nucleation theory [27] as

$$d_p^* = \frac{4\sigma v_m}{k_B T \ln S} \tag{23}$$

where σ is the surface tension of the condensing substance and $v_m$ is its molecular (atomic) volume. Since it is considered that all available cadmium vapor nucleates homogeneously, the resulting number of particles can be calculated from

$$N_{Cd,o} = \frac{(mass\_output)\left(\frac{1}{\rho_{Cd}}\right)}{\pi \frac{\left(d_p^*\right)^3}{8}} \tag{24}$$

where *mass_output* is the total mass of cadmium collected per unit time. Analogous equations are used to obtain the number of entrained copper particles in the larger size ranges. With this data, the diameter of average mass of the aerosol after nucleation is given by

$$d_{p,o} = \left( \frac{\sum_i^N d_i^3}{N_o} \right)^{\frac{1}{3}} \tag{25}$$

where $N_o$ is the total number of particles (including entrained and nucleated ones).

The cadmium nuclei coagulate with each other and also with the entrained copper particles present in the system. This is modelled by a polydisperse coagulation process, and the final diameter of average mass of the aerosol is calculated by

$$d_p = d_{p,o}(1 + N_o \underline{K} t)^{1/3} \tag{26}$$

where $\underline{K}$ is the polydisperse coagulation coefficient for k different size ranges, calculated from

$$\underline{K} = \sum_{i=1}^{k} \sum_{j=1}^{k} K_{i,j} f_i f_j \tag{27}$$

where $f_i$ and $f_j$ are the fractions of the total number of particles in these ranges. Here $K_{i,j}$ is the coagulation coefficient between particles of size ranges i and j, and it determines the rate of decrease in the number of particles according to the Smoluchowski equation:

$$\frac{dN}{dt} = -KN^2 \tag{28}$$

Three size ranges are considered, namely +18 μm and +3.2/-18 μm, which contain entrained particles, and the size of the small condensed Cd particles.

To calculate $K_{i,j}$ for coagulation between the entrained particles and also between nucleated and entrained particles, thermal coagulation due to Brownian motion between particles is considered, assuming that every collision leads to coalescence. For these cases, $K_{i,j}$ is [28]

$$K_{i,j} = \pi(d_i + d_j)(D_i + D_j) \tag{29}$$

where $d$ is the average particle diameter and $D$ is the diffusion coefficient for particles in the respective size range.

For coagulation of the nucleated cadmium particles between themselves, a different expression for $K_{i,j}$ is used. It has been found that, for this small size range, particle collisions generally result in coalescence [26]. Since the particles considered are smaller than the mean free path of the gas ($d_p < 0.06$ μm), their coagulation rate (i.e. the decrease in particle number $N_{Cd}$, can be described using free molecule theory (or kinetic theory of gases) as [26]

$$\frac{dN_{Cd}}{dt} = -\frac{6}{5}k_{theory}f_v^{1/6}N_{Cd}^{\ 11/6} \tag{30}$$

In the above equation, $f_v$ is the particulate volume fraction (volume of particles per unit volume of gas), and $k_{theory}$ is given by free molecule theory as

$$k_{theory} = \frac{5}{12}\left(\frac{3}{4\pi}\right)^{1/6}\left(\frac{6k_BT}{\rho_p}\right)^{1/2} G\alpha \tag{31}$$

where $k_B$ is Boltzmann's constant, $\rho_p$ is the density of the particles, $G$ is a factor representing interparticle dispersion forces, and $\alpha$ reflects the variation in collision rates when different particle sizes are present. It is assumed that these particles are mostly spherical (thus $G = 2$), and that they are sufficiently small and the coagulation time is large so that a self-preserving size distribution applies (thus $\alpha = 6.55$).

Furthermore, $f_v$ is calculated as

$$f_v = (c)\left(\frac{1}{\rho_P}\right) = \left(\frac{mass\_output}{volume\_throughput}\right)\left(\frac{1}{\rho_P}\right) \tag{32}$$

where *mass_output* is the mass of the condensation aerosol particles entering the sampling probe per unit time and *volume_throughput* is the volume of gas flowed through the sampling probe per unit time. The *mass_output* is obtained by dividing the amount of particles collected that are smaller than 0.32 μm by the aerosol sampling time.

Combining equations (28) and (30), the coagulation coefficient for the cadmium particles coagulating with themselves is

$$K_{Cd,Cd} = \frac{-\frac{6}{5}k_{theory}f_v^{1/6}}{N_{Cd}^{\ 1/6}} \tag{33}$$

### 3.2.2. Results and Discussion

The results obtained from the above calculations are presented in Table 4. These calculations will be compared to the experimental results in section 4.2.

Table 4. Theoretical Diameter of Average Mass of Cu-Cd Aerosols

| Time at which sample was taken (min) | [% Cd] in melt | Diameter of Average Mass (μm) |
|---|---|---|
| RUN 1 | | |
| 7 | 0.1958 | 0.045 |
| 32 | 0.1007 | 0.028 |
| 94 | 0.0200 | 0.021 |
| 120 | 0.0100 | 0.018 |
| 140 | 0.0063 | 0.016 |
| RUN 2 | | |
| 63 | 0.1025 | 0.054 |
| 140 | 0.0235 | 0.029 |
| 175 | 0.0117 | 0.020 |
| 213 | 0.0056 | 0.014 |
| 256 | 0.0024 | 0.013 |
| RUN 3 | | |
| 60 | 0.2060 | 0.047 |
| 93 | 0.1020 | 0.038 |
| 121 | 0.0546 | 0.024 |
| 183 | 0.0146 | 0.026 |
| 218 | 0.0069 | 0.014 |
| 245 | 0.0038 | 0.009 |
| 306 | 0.0010 | 0.008 |

# 4. COMPARISON OF EXPERIMENTS AND THEORY

## 4.1. Evaporation Rates

The experimental and theoretical evaporation curves obtained are compared in Figures 38-42. The experimental data is most reliable in the two copper-cadmium cases, since several runs were done in each case. It is seen that the theoretical prediction matches very closely with the experimental findings. In the case of copper-cadmium at 0.75 L/min, theoretical and average experimental overall evaporation coefficients are 0.0190 and 0.0195 min$^{-1}$, while in the 1.5 L/min case they are 0.0260 and 0.0272 min$^{-1}$, respectively. These values are within 5% of each other.

The other experimental data is not as reliable, as only one run could be done in each case. This may be one of the reasons why a greater discrepancy with the model is observed. In the copper-zinc case at 0.75 L/min, theoretical and experimental $K_e$ 's are 0.0022 and 0.0046 min$^{-1}$, respectively, which results in a 35% difference in the concentration of zinc in the copper three hours after injection.

In the copper-zinc-slag experiment at 0.75 L/min, theoretical and experimental $K_e$'s are 0.0007 and 0.0017 min$^{-1}$, respectively. Thus, according to the experiment, 20% more zinc than predicted is evaporated after four hours. This draws attention due to the fact that the model considers that equilibrium is reached in the bubbles in this case, meaning that the predicted evaporation rate should be the highest thermodynamically achievable rate. However, the rate determined experimentally was higher than the predicted one. This might be due to the uncertainty in the experimental and analytical procedures, which is discussed below. Another reason might be that the slag height

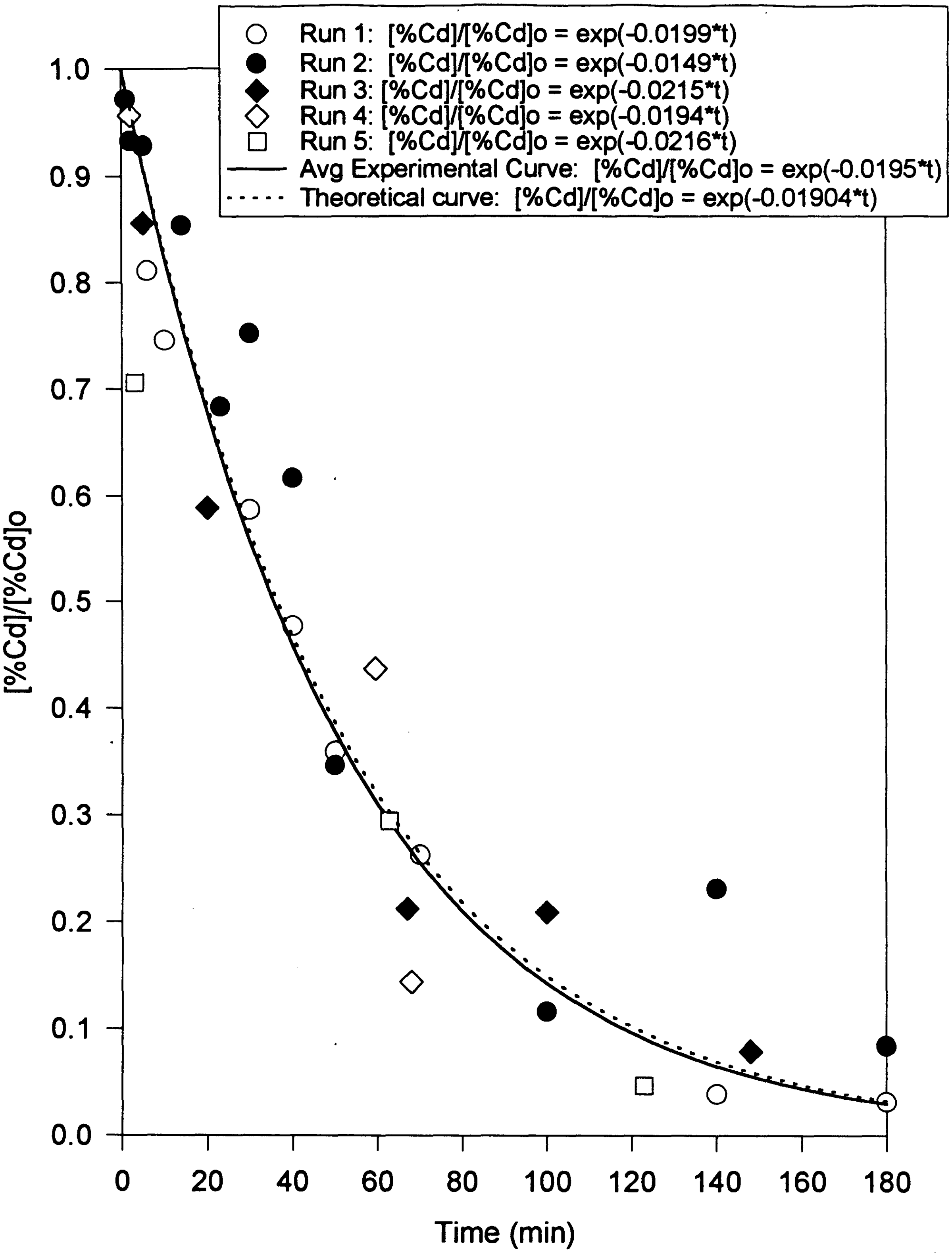

Figure 38. Evaporation of cadmium from copper.
(T=1473 K, gas flow = 0.75 L/min, single 1/4" OD gas lance)

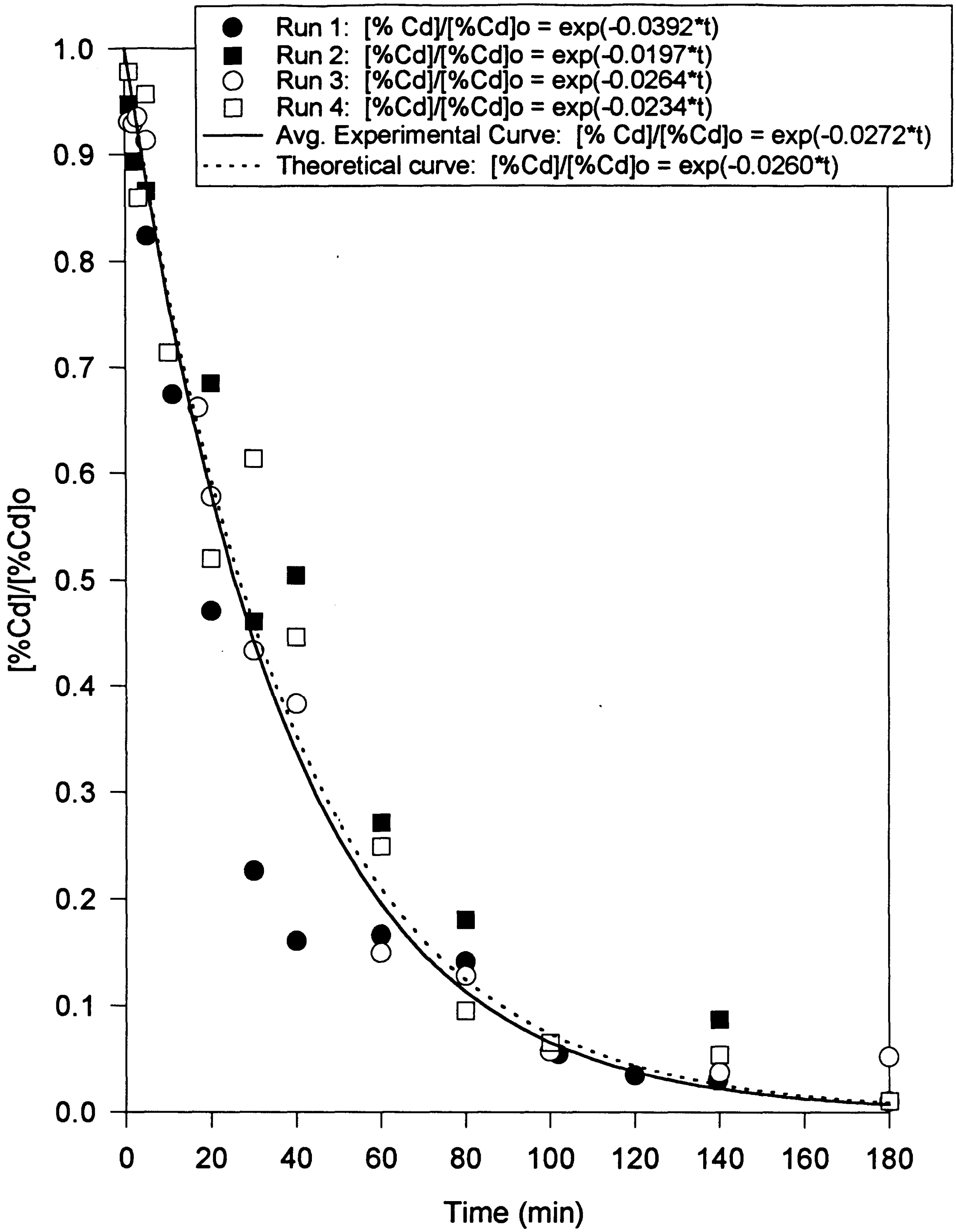

Figure 39. Evaporation of cadmium from copper.
(T=1473 K, gas flow = 1.5 L/min, single 1/4" OD gas lance)

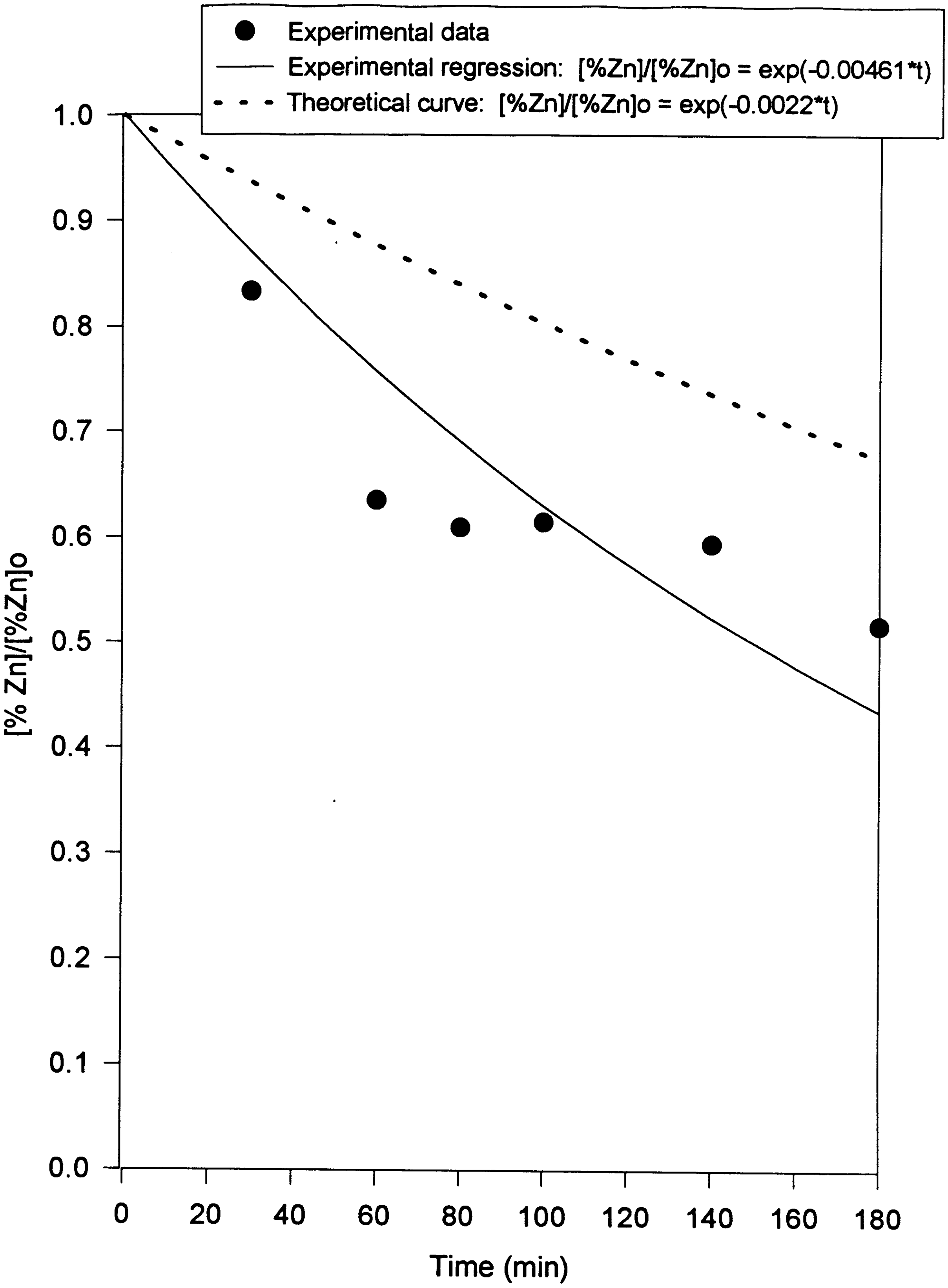

Figure 40. Evaporation of zinc from copper.
(T=1473 K, gas flow = 0.75 L/min, single 1/4" OD orifice)

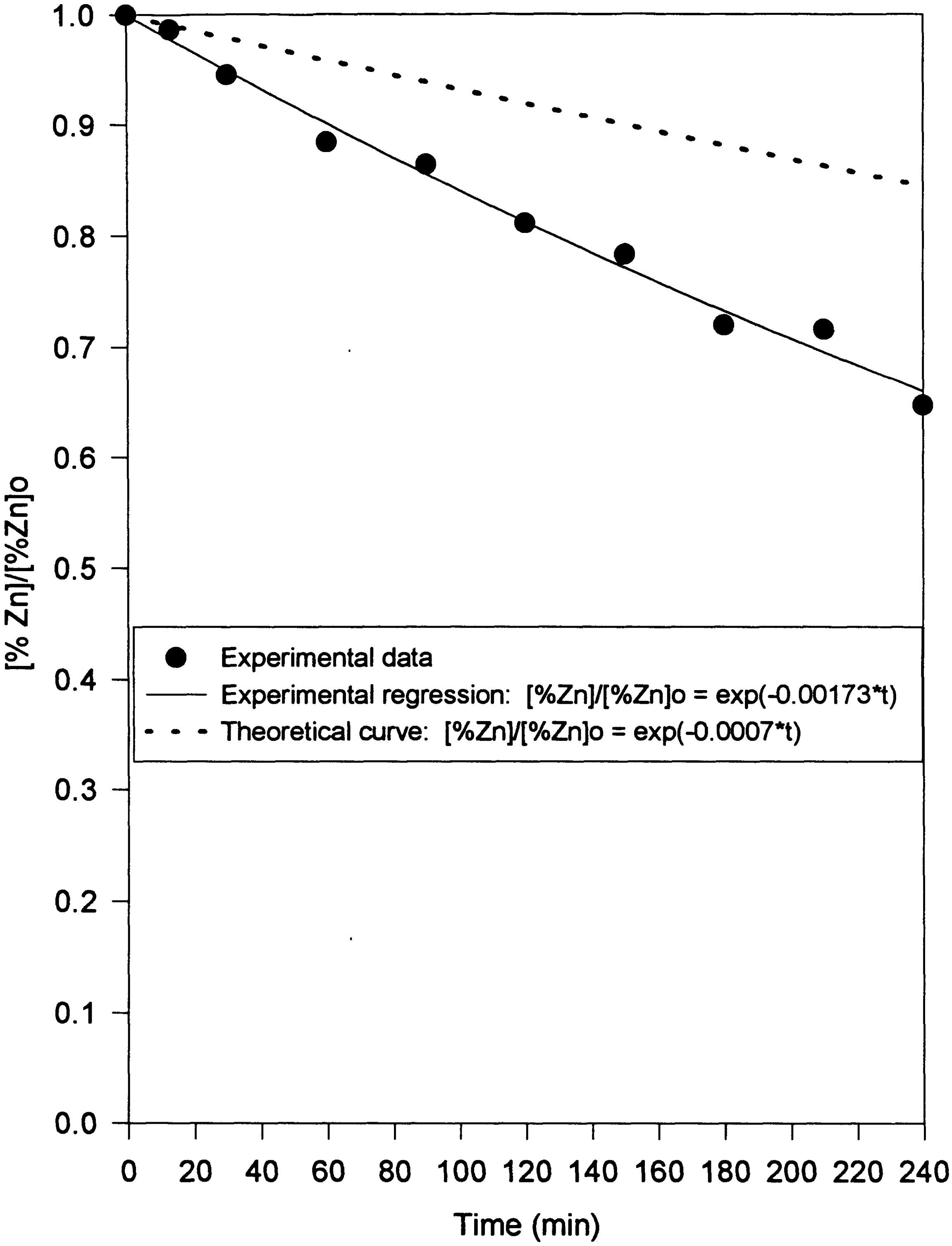

Figure 41. Evaporation of zinc from copper with a slag layer.
(T=1473 K, gas flow =0.75 L/min, single 1/4" OD orifice)

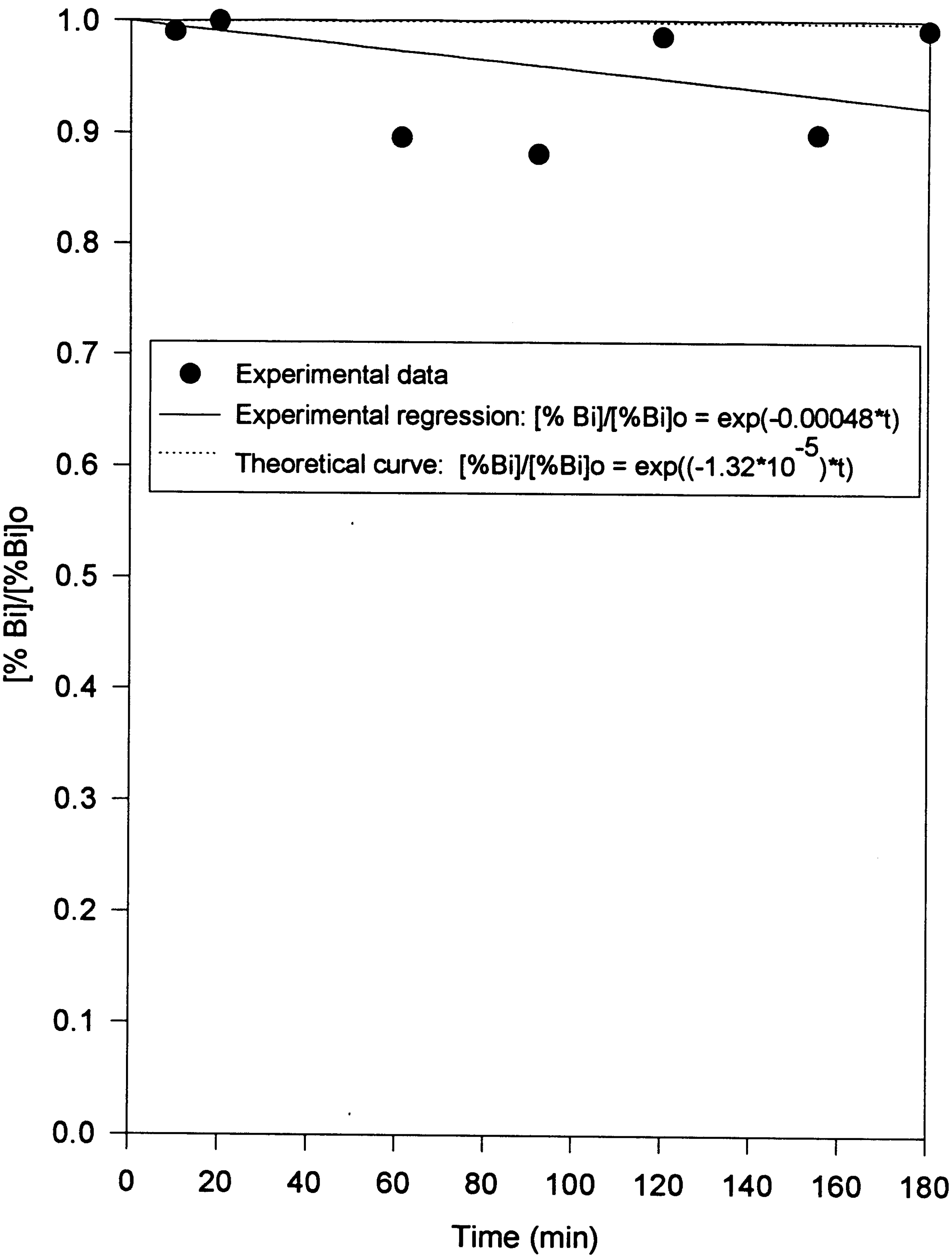

Figure 42. Evaporation of bismuth from copper with a slag layer. (T=1473 K, Q=0.75 L/min, single 1/4" OD orifice)

(about 4-5 cm) was not sufficient to totally eliminate evaporation from the top surface of the melt.

In the copper-bismuth-slag case, the theoretical $K_e$ was calculated as $1.3\text{x}10^{-5}$ $\text{min}^{-1}$, while the experimental value was found to be 0.00048 $\text{min}^{-1}$. This accounts for an 8% difference in the copper content of bismuth after three hours. As in the previous case, the experimental rate was found higher than the predicted one, and the same problem discussed in the copper-zinc-slag system applies. Since the evaporation coefficients are so low in this case, this experiment should be carried out for a longer period of time to get more reliable results.

Potential sources of error involved in the experimental process are the variations in gas flow rate and temperature. The ICP/MS analytical technique introduces an additional error of +/- 7% in the results. Together, these factors give a total uncertainty of +/- 10-20%, depending on the impurity involved. Also, bubbles are not evenly distributed throughout the melt and rise mainly in its center, close to where the lance is, so there is an uneven disruption of the thermal convection currents above the melt surface, which has been neglected in the model.

### 4.2. Aerosol Formation Mechanisms

In general, the experimental observation that the small particles collected become even smaller with time is consistent with the theoretical model. This occurs because, as *[% Cd]* in the melt decreases, less Cd nuclei are formed and thus there is less coagulation of Cd particles, which results in a smaller average diameter.

The diameter of average mass of each aerosol sample was calculated using equation (25) and compared to the theoretical predictions. The following table compares the results.

Table 5. Comparison of Theoretical and Experimental Diameters of Average Mass of Cu-Cd Aerosols

| Time at which sample was taken (min) | [% Cd] in melt | Theoretical Diameter of Average Mass (μm) | Experimental Diameter of Average Mass (μm) |
|---|---|---|---|
| RUN 1 | | | |
| 7 | 0.1958 | 0.045 | 0.043 |
| 32 | 0.1007 | 0.028 | 0.047 |
| 94 | 0.0200 | 0.021 | 0.029 |
| 120 | 0.0100 | 0.018 | 0.025 |
| 140 | 0.0063 | 0.016 | 0.024 |
| RUN 2 | | | |
| 63 | 0.1025 | 0.054 | 0.068 |
| 140 | 0.0235 | 0.029 | 0.055 |
| 175 | 0.0117 | 0.020 | 0.036 |
| 213 | 0.0056 | 0.014 | 0.038 |
| 256 | 0.0024 | 0.013 | 0.044 |
| RUN 3 | | | |
| 60 | 0.2060 | 0.047 | 0.076 |
| 93 | 0.1020 | 0.038 | 0.043 |
| 121 | 0.0546 | 0.024 | 0.038 |
| 183 | 0.0146 | 0.026 | 0.046 |
| 218 | 0.0069 | 0.014 | 0.031 |
| 245 | 0.0038 | 0.009 | 0.024 |
| 306 | 0.0010 | 0.008 | 0.022 |

As can be seen, the theoretical calculations range from being about 35-85% (average is 57%) of the experimental values, and they diverge more from the latter as *[% Cd]* in the melt decreases. Possible reasons for this discrepancy might be some or all of the following:

1. Condensation of cadmium on carbon or other particles in the +0.32/-1.8 μm range, of

which there is a small amount. This condensation would be much faster than that on the larger +3.2/-18 μm and +18 μm Cu particles. This would increase the final diameter of average mass.

2. Entrapment of particles on the walls of the sampling probe or the furnace. These particles would agglomerate with time and, when they are reentrained into the gas phase, would also increase the diameter of average mass.

3. Turbulence in the sampling probe caused by radial gas flow. This would enhance coagulation between the larger particles, and was not taken into account by the equations used, since they are derived for coagulation due to Brownian motion.

4. Existence of non-spherical particles, which coagulate more rapidly than spherical ones due to their higher surface area.

One interesting thing to note is that when the amount of entrained particles increases (as in Run 2), the total amount of cadmium collected (coagulated) on them increases, and the amount collected in the +0.32/-1.8 μm range decreases. This occurs because, since there is a greater total surface area of entrained particles, more cadmium particles will coagulate with them. Thus, fewer Cd particles are left to coagulate with themselves and thus fewer +0.32/-1.8 μm particles are formed. This indicates that these are competing mechanisms of aerosol formation.

## 5. CONCLUSIONS

The following conclusions can be drawn from the present study:

1. Metallic solutes evaporate with first-order kinetics with respect to their concentration in the melt, which thus decreases exponentially with time.

2. Of the solutes considered, cadmium evaporates from copper at 1200 °C (about 30-fold decrease in concentration in 3 hours). Zinc and thallium are also thought to evaporate preferentially, although at a significantly lower rate.

3. The evaporation coefficient for cadmium in molten copper at 1200 °C was found experimentally to be 0.0195 $\text{min}^{-1}$ for a bubbled argon flow rate of 0.75 L/min, and 0.0272 $\text{min}^{-1}$ for 1.5 L/min. The theoretically obtained values were 0.0190 and 0.0260 $\text{min}^{-1}$, respectively, which give almost identical evaporation curves.

4. Evaporation of the solutes occurs into the bubbles and through the melt surface. At 0.75 L/min of bubbling, the molten copper surface has a greater contribution to the overall evaporation rate. However, the bubbles become more important than the melt surface at 1.5 L/min.

5. In molten copper, the gas phase was found to control the evaporation rates of all solutes considered through the bubbles and the melt surface.

6. Evaporation from molten iron at 1600 °C was theoretically found to be very fast for Zn, Bi, and Pb (50-fold or greater decrease in concentration in about 1 hour) because of their very high $\gamma P_{vap}$ products. It is thought that, because of these high products, mass transfer resistance in the liquid phase will control the evaporation rates of these elements.

7. The diameter of average mass of the aerosol formed by cadmium vapor evaporating from molten copper was seen to decrease with decreasing concentration of cadmium in the melt. However, the relative amount of cadmium that adhered to the entrained copper particles remained constant.

8. Cadmium particles were seen to be between 0.016 and 0.3 μm in diameter, while entrained copper particles were from 3 to 100 μm in size. The former had spherical, hexagonal, or polygonal shapes (probably representing hexagons in different orientations), while the latter had very irregular shapes. SEM micrographs showed evidence of small cadmium particles adhering to large irregular particles.

9. It is thought that cadmium particles nucleate instantly upon quenching and then they grow by coagulation between themselves and the entrained copper particles. This model predicts a diameter of average mass ranging from 35-85% of the experimental values. Possible reasons for this discrepancy are thought to be condensation of cadmium on carbon or other particles in the +0.32/-1.8 μm range, entrapment of particles on the walls of the sampling probe or the furnace and their subsequent reentrainment, turbulence in the sampling probe caused by radial gas flow, and/or presence of non-spherical particles.

# Appendix A: Derivation of Overall Mass Transfer Rates

As said in section 3.1.2, the basic mass balance equation applying to the solute can be expressed as follows:

$$\begin{pmatrix} Mass\_flux \\ evaporating \\ from\_melt \end{pmatrix} = \begin{pmatrix} Mass\_flux \\ to\_bubbles \end{pmatrix} + \begin{pmatrix} Mass\_flux \\ through \\ melt\_surface \end{pmatrix} \tag{A.1}$$

Assuming that the metal bath is well mixed by bubbling and convective stirring so that the solute concentration in the bulk liquid is uniform, this equation translates to

$$\frac{-M_l d[\%X]}{100 MW_X dt} = \frac{K_{ol,b}\rho_l A_b([\%X]-[\%X]_{eq,b})}{100 MW_X} + \frac{K_{ol,ms}\rho_l A_{ms}([\%X]-[\%X]_{eq,ms})}{100 MW_X} \tag{A.2}$$

where $[\%X]_{eq}$ refers to the hypothetical solute concentration in the melt in equilibrium with the partial pressure $P_X$ in the bulk gas phase, and the subscripts "b" and "ms" refer to the bubbles and the melt surface, respectively. Each of the two terms on the right hand side of equation (A.2) will be treated separately in the next two sections.

## A.1. Evaporation Through the Bubbles

In order to facilitate the computation of the flux of X going to the bubbles, the pertinent term in equation (A.2) will be expressed as:

$$Q\left(\frac{P_X^{exit}}{P_{Ar}}\right) \tag{A.3}$$

where $Q$ is the flow rate of argon in mol/s and $P_x^{exit}$ is the solute partial pressure in the bubble when it bursts at the surface of the melt. Now an expression will be derived to relate $P_x^{exit}$ to $[\%X]$. If it is assumed that $P_X$ is uniform throughout the bulk gas in the bubble, and that only monatomic evaporation takes place, *[% X]$_{eq,b}$* can be related to it through the following relation:

$$P_X = K_{eq} f_X [\%X]_{eq,b} \tag{A.4}$$

The following equation, derived from Engh's [10] treatment, is set up to express $P_x$ in terms of the concentration of X in the melt. It states that the moles of X transferred per second to the bubbles in a control volume (a slice of the melt) are equal to the transfer of X to the bubbles in the control volume (see Figure A.1):

$$\frac{K_{ol,b}\rho_l \Delta A_b([\%X]-[\%X]_{eq,b})}{100 MW_X} = Q\,\Delta\left(\frac{P_X}{P_{Ar}}\right) \tag{A.5}$$

where $\Delta A_b$ is the bubble surface area within the control volume.

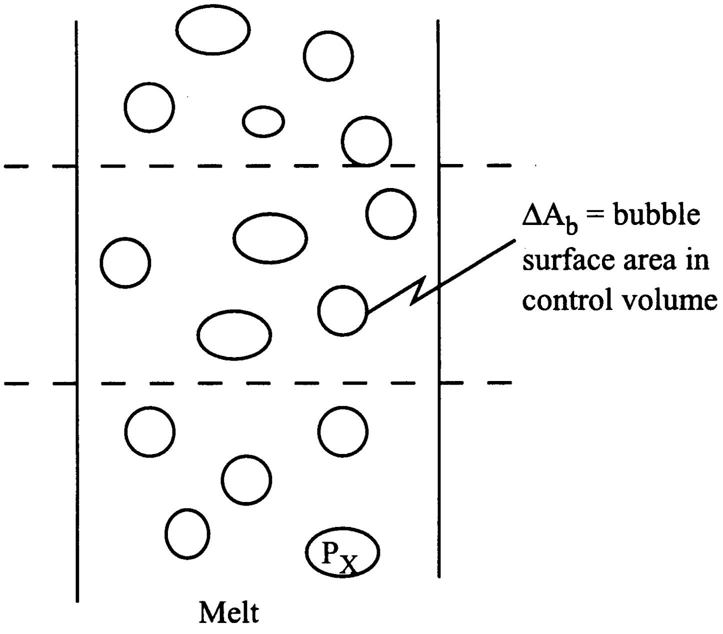

Figure A.1. Control volume in the molten metal.

Moving the terms that depend on $P_X$ to the right and using equation (A.4), the following integral is set up:

$$\frac{K_{ol,b}\rho_l A_b P_{Ar}}{100 MW_X Q} = \int_0^{P_X^{exit}} \frac{dP_X}{[\%X] - P_X / (f_X K_{eq})} \tag{A.6}$$

The total bubble surface area, $A_b$, is calculated as

$$A_b = \frac{3GH}{r_b U_b} \tag{A.7}$$

where $G$ is the volumetric gas flow rate, and $H$ is the height of the melt.

The solution to this integral is

$$\frac{K_{ol,b}\rho_l A_b P_{Ar}}{100 MW_X Q f_X K_{eq}} = \ln\left(\frac{[\%X]}{[\%X] - P_X^{exit} / (f_X K_{eq})}\right) \tag{A.8}$$

The left term of this equation is called the dimensionless contact area, $\phi_A$, which determines the extent to which equilibrium is reached in the bubbles [10].

$$\phi_A = \frac{K_{ol,b}\rho_l A_b P_{Ar}}{100 MW_x Q f_X K_{eq}} \tag{A.9}$$

When $\phi_A$ is 3 or more, it can be considered that the equilibrium partial pressure of the solute is reached in the bubbles. From $\phi_A$ the "efficiency of gas purging" can be determined by

$$Z = 1 - \exp(-\phi_A) = \frac{P_X^{exit}}{f_X [\%X] K_{eq}} \tag{A.10}$$

which is the ratio of the actual exit partial pressure of the solute to its equilibrium exit partial pressure in the bubble. Again, here it is assumed that only monatomic evaporation occurs. The justification for neglecting polyatomic evaporation will be presented in section A.3.

Inserting $Z$ into expression (A.3), the bubble evaporation term becomes

$$\frac{QZf_X K_{eq}[\%X]}{P_{Ar}} \tag{A.11}$$

For the cases when $P_X \ll P_{Ar}$, this expression can be evaluated easily by assuming $P_{Ar}=P_{tot}=1$ atm. For all other cases, such as those of bismuth, lead, and zinc evaporating from iron, $P_X$ has to be evaluated at each point in the bath by solving the following integral which is derived from equations (A.4) and (A.6):

$$\int_0^{P_X} \frac{dP}{(f_X K_{eq}[\%X]-P)(1-P)^2} = \frac{K_{ol,b}\rho_l A_b h}{100MW_X QHf_X K_{eq}} \tag{A.12}$$

Here $h$ is the distance from the bottom of the bath, assuming an even bubble distribution throughout the height of the melt, $H$. Thus, $[\% X]_{eq,b}$ varies with position of the bubble in the melt and also with time, because the concentration of X in the melt varies with time as well. This makes the mathematical analysis rather complicated, although it can be simplified by considering an average solute pressure in the bubble. This value is taken as the solute pressure in the bubbles in the middle of the melt (at $h=H/2$). This procedure requires that the values of $P_X$ ,. $[\% X]_{eq,b}$ , and $[\%X]$ be calculated at discrete time intervals in a stepwise manner using software such as Maple.

## A.2. Evaporation Through the Melt Surface

In the term

$$\frac{K_{ol,ms}\rho_l A_{ms}([\%X]-[\%X]_{eq,ms})}{100MW_X} \tag{A.13}$$

from equation (49), the only unknown quantity is $[\% X]_{eq,ms}$ . This is the hypothetical solute concentration in the melt that would be in equilibrium with the solute partial pressure $P_{X,top}$ in the bulk gas above the melt. As said before, it is assumed that this gas is so well stirred by the convection currents together with the bulk flow coming from the bursting bubbles that $P_{X,top}$ is uniform in the gas above the melt except for a small boundary layer over the melt surface. It has been found experimentally that the value of $P_{X,top}$ is very low and neglecting it increases the overall theoretical evaporation rate by about 3-5%, depending on the solute. However, the theoretical results remain within +/- 10% of the actual evaporation rates. Thus, $P_{X,top}$ (and so $[\%X]_{eq,ms}$) will be neglected when obtaining theoretical curves for all the solutes.

## A.3. Polyatomic Evaporation

Of the solutes considered, Bi, Sb, Se, and Te are known to evaporate polyatomically as follows:

Table A.1. Metallic Solutes That Evaporate Polyatomically

| Species | Evaporating Molecule |
|---|---|
| Bi | Bi, $Bi_2$ |
| Sb | Sb, $Sb_2$, $Sb_4$ |
| Se | Se, $Se_2$, $Se_3$, $Se_4$, $Se_5$ |
| Te | Te, $Te_2$ |

However, polyatomic molecules were found to represent a negligible amount of the evaporating species. As an example, in the cases of bismuth and antimony, the following results were obtained, assuming equilibrium between the polyatomic molecules is reached:

$$\left(\frac{P_{Bi_2}}{P_{Bi}}\right)_{eq} = 0.0044[\%Bi] \tag{A.14}$$

$$\left(\frac{P_{Sb_2}}{P_{Sb}}\right)_{eq} = 0.0046[\%Sb] \tag{A.15}$$

$$\left(\frac{P_{Sb_4}}{P_{Sb}}\right)_{eq} = 1.57x10^{-11}[\%Sb]^3 \tag{A.16}$$

Thus, in all calculations, polyatomic evaporation will be neglected.

## Appendix B: Derivation of Mass Transfer Coefficients

The three most important steps in the majority of mass transfer processes between liquid and gas phases are:

1. Diffusion of solute in the melt boundary layer
2. Interface reaction
3. Diffusion of solute in the gas boundary layer

The molar flux of solute X in these steps (for each evaporation mechanism) can be expressed as follows:

*Step 1. Diffusion of X in the melt boundary layer* ($X \rightarrow X_i$)*:*

The mass flow rate of X for this step can be written as:

$$N_{X(l)} = k_l\,(C_l - C_{li}) \tag{B.1}$$

where $C_l$ and $C_{li}$ are the concentrations of the species X in the melt and at the melt boundary, respectively, and $k_l$ is the liquid phase mass transfer coefficient.

*Step 2. Interface (evaporation) reaction* ($X_i \rightarrow X_i\,(g)$)*:*

The molar flux of X in this step can be expressed by the Hertz-Knudsen-Langmuir equation [1] :

$$N_{X(c)} = \frac{\alpha}{\sqrt{2\pi RTMW_x}}\,(P_{li} - P_{gi}) \tag{B.2}$$

where $MW_x$ is the molecular weight of X, $T$ is the temperature, $R$ is the gas constant, and $P_{li}$ and $P_{gi}$ are the partial pressures of X at the boundary of the melt and gas phase, respectively. The parameter $\alpha$ is a condensation (sticking) coefficient which is approximately 1, as evaporating molecules are assumed to be evacuated sufficiently quickly from the melt/gas interface so as to prevent their condensation back into the melt. $P_{li}$ is equal to the partial pressure of X which would be in equilibrium with the concentration of X at the melt interface, $C_{li}$:

$$P_{li} = P_x^{\circ} \gamma_x X_x = P_x^{\circ} \gamma_x \frac{MW_l}{\rho_l} C_{li} \tag{B.3}$$

$P_X^o$ is the vapor pressure of pure X at temperature T, $\gamma_X$ is the activity coefficient of X, and $\rho_l$ is the density of the melt.

This flux is important for low pressure operation, but its contribution to the overall mass transfer process at higher pressures is negligible. This is because at higher pressures the mean free path of the evaporating atoms is small (6.3 x $10^{-8}$ m for argon at 1 atm), rendering the interface reaction resistance insignificant as compared to the resistance in the gas boundary layer. Therefore, it will be assumed that the concentrations of X in the liquid and gas phases at the interface are in equilibrium.

*Step 3. Diffusion of X(g) through the gas boundary layer* $(X_i(g) \rightarrow X(g))$:

The molar flux of X in the gas phase boundary layer can be expressed as:

$$N_{X(g)} = \frac{D_{X-g}}{\delta_g} (C_{gi} - C_g) \tag{B.4}$$

where $C_{gi}$ is the concentration of X in the gas phase at the boundary, $C_g$ is the concentration of X in the bulk gas, $D_{X\text{-}g}$ is the diffusion coefficient of X in the gas, and $\delta_g$ the thickness of the gas boundary layer.

## B.1. Estimation of the Overall Mass Transfer Coefficients

In this section, an expression for an overall mass transfer coefficient ($K_{ol}$), to be used with an overall mass transfer equation using liquid phase concentrations, will be derived. This expression will be valid both for evaporation of X into the bubbles and from the melt surface.

With reference to Figure 17, equations (B.1) and (B.4) can be rewritten as:

$$N_{X(l)} = \frac{k_l \rho_l}{MW_l}(x_X - x_{Xi}) \tag{B.5}$$

$$N_{X(g)} = k_g \frac{P_{tot}}{RT}(y_{Xi} - y_X) \tag{B.6}$$

where $y_X$ and $x_X$ are the mole fractions of X in the gas phase and melt, respectively, and $P_{tot}$ is the total pressure of the gas. $k_g$ and $k_l$ are the gas and liquid phase mass transfer coefficients, respectively. For the reasons outlined above, the flux at the interface will not be considered in the calculation of $K_{ol}$.

An overall flux of species X can also be described by the equation:

$$N_X = K_{ol} \frac{\rho_l}{MW_l}(x_X - x_X^*) \tag{B.7}$$

where $x^*_x$ is the mole fraction of X in the melt that would be in equilibrium with the bulk concentration of X in the gas phase, and $K_{ol}$ is the overall mass transfer coefficient based on the solute concentrations in the liquid phase. From this equation we get:

$$\frac{1}{K_{ol}} = \frac{\rho_l (x_X - x_X^*)}{MW_l N_X} = \frac{\rho_l}{MW_l}\left[\frac{(x_X - x_{Xi})}{N_X} + \frac{(x_{Xi} - x_X^*)}{N_X}\right] \tag{B.8}$$

Defining an equilibrium distribution coefficient as

$$K_{d,eq} = \left( \frac{y_X}{x_X} \right)_{eq} \tag{B.9}$$

we can write

$$x_X^* = \frac{y_X}{K_{d,eq}} \tag{B.10}$$

and assuming equilibrium between the gas phase and the melt at the interface:

$$x_{Xi} = \frac{y_{Xi}}{K_{d,eq}} \tag{B.11}$$

Equations (B.8), (B.10), and (B.11) can be combined to give

$$\frac{1}{K_{ol}} = \frac{\rho_l (x_X - x_{Xi})}{MW_l N_X} + \frac{\rho_l}{MW_l} \left[ \frac{\left( \frac{y_{Xi}}{K_{d,eq}} \right) - \left( \frac{y_X}{K_{d,eq}} \right)}{N_X} \right] \tag{B.12}$$

Furthermore, at steady state, the fluxes through each part of the system must be equal:

$$N_{X(g)} = N_{X(l)} = N_X \tag{B.13}$$

and using (B.5), (B.6), and (B.13) the final relation for $K_{ol}$ is obtained:

$$\frac{1}{K_{ol}} = \frac{1}{k_l} + \left( \frac{\rho_l / MW_l}{\frac{P_{tot}}{RT}} \right) \frac{1}{K_{d,eq} k_g} \tag{B.14}$$

The first term on the right hand side represents the liquid phase mass transfer resistance, while the second represents the gas phase mass transfer resistance. If we define $k_g'$ as

$$k_g' = \left( \frac{P_{tot}/RT}{\rho_l/MW_l} \right) K_{d,eq} k_g \qquad \text{(B.15)}$$

then $1/k_g'$ is the gas phase mass transfer resistance, which is analogous to the liquid side resistance.

To get $K_{d,eq}$, the following equilibrium constant for the process *X (% in liquid)* → *X(g)* is used, considering atmospheric pressure:

$$K_{eq} = \frac{P_X}{f_X(\%X)} = \frac{y_X(1\ atm)}{f_X(\%X)} = \frac{y_X}{f_X(\%X)} = \exp\left( -\frac{\Delta G^o}{RT} \right) \qquad \text{(B.16)}$$

where $f_X$ is the Henrian activity coefficient and

$$\Delta G^o = \Delta G^o{}_{\underline{X(\%)}\rightarrow X_l} + \Delta G^o_{X_l \rightarrow X_g} = RT \ln\left( \frac{100 MW_x}{\gamma_x MW_l} \right) + \Delta G^o_{X_l \rightarrow X_g} \qquad \text{(B.17)}$$

The calculation of the activity coefficients $\gamma_x$ for the case of an iron-carbon melt will be shown in section B.2.

After converting weight percent to mole fraction of X the following expression for $K_{d,eq}$ is obtained:

$$\mathrm{K}_{d,eq} = \left( \frac{y_X}{x_X} \right)_{eq} = \frac{100 K_{eq} MW_X f_X}{MW_l} \qquad \text{(B.18)}$$

and $k_g'$ now becomes:

$$k_g' = \left( \frac{100 P_{tot} K_{eq} MW_X f_X}{\rho_l RT} \right) k_g \qquad \text{(B.19)}$$

To calculate $K_{ol}$ using equation (B.14), values of $\gamma_x$ , $k_l$ , and $k_g$ are needed. The expressions used to obtain these values are presented below. In the calculation of $k_g$, different physical situations lead to different expressions ($k_{g,b}$ and $k_{g,ms}$) in the cases of evaporation of X into the bubbles and from the melt surface, respectively. Thus, there will be two expressions for $K_{ol}$, which will be referred to as $K_{ol,b}$ and $K_{ol,ms}$ .

## B.2. Estimation of Activity Coefficients in an Fe-C Melt

The activity coefficient of solute X in a multicomponent solution of N solutes (numbered 1, 2, ...... N) can be expressed as [29]

$$\ln \gamma_X = \ln \gamma_L + \ln \gamma_X^o + \varepsilon_{X1} x_1 + \varepsilon_{X2} x_2 + \varepsilon_{X3} x_3 \tag{B.20}$$

where $\varepsilon_{ij}$ is the interaction coefficient between "i" and "j" based on mole fraction, $\gamma_X{}^o$ is the Raoultian activity coefficient of the solute at infinite dilution (when $X_{\text{solvent}} \sim 1$), and $\gamma_L$ is the activity coefficient of the melt (solvent) given by

$$\ln \gamma_L = -\frac{1}{2} \sum_{j=1}^{N} \sum_{k=1}^{N} \varepsilon_{jk} x_j x_k \tag{B.21}$$

Sigworth and Elliott [16] compiled data on the interaction coefficients in liquid iron. The values of interaction coefficients based on weight percent ($e_{ij}$) are taken from these compilations. In order to convert $e_{ij}$'s to $\varepsilon_{ij}$'s, the following relationship is used:

$$\varepsilon_{ij} = 230 \, \frac{MW_j}{MW_i} e_{ij} + \frac{MW_i - MW_j}{MW_i} \tag{B.22}$$

## B.3. Estimation of the Liquid Phase Mass Transfer Coefficient

A very important variable in the determination of $k_l$ is $D_{X\text{-}l}$ , which can be approximated by two means:

1. Hayduk-Minhas equation [30] (valid for non-polar solvents):

$$D_{X-l} = \frac{1.55x10^{-8}\ T^{1.29}\left(\dfrac{\sigma_l^{0.25}\ MW_l}{\rho_l}\right)^{0.5}}{\mu_l^{0.92}\ V_l^{0.23}\left(\dfrac{\sigma_X^{0.25}.\ MW_X}{\rho_X}\right)^{0.42}} \tag{B.23}$$

where $\sigma_l$ and $\sigma_X$ are the surface tension of the molten metal and the solute, respectively, and $\mu_l$ is the viscosity of the molten metal.

2. Tyn-Calus equation [31] (also valid for non-polar solvents):

$$D_{X-l} = 8.93x10^{-8}\,\frac{TV_X^{1/6}}{\mu_l V_l^{1/3}}\left(\frac{\dfrac{\sigma_l^{0.25} MW_l}{\rho_l}}{\dfrac{\sigma_X^{0.25} MW_X}{\rho_X}}\right)^{0.6} \tag{B.24}$$

where $V_l$ and $V_X$ are the molar volumes at the boiling point of the molten metal and the solute, respectively.

The bubble diameter, $d_b$, is estimated using the formulas described below. The average values are used in the calculations for $k_l$.

1. Sano and Mori [32] derived the following equation by considering the widely accepted concept that the outer diameter of the lance orifice should be used in the estimation of $d_b$

when liquid metals do not wet the lance material. In this case, the gas lance is made of alumina, which is not wetted by liquid metals, so this equation will apply.

$$d_b = \left[ \left( \frac{6\sigma_l d_{orif.}}{\rho_l g} \right)^2 + 0.0242 \left( G^2 d_{orif.} \right)^{0.867} \right]^{1/6} \tag{B.25}$$

where $d_{orif}$ is the lance orifice diameter, $g$ is the acceleration of gravity, and $G$ is the volumetric gas flow rate.

2. Wraith and Kakutani [33] modified the equation originally derived by Davidson-Schuler considering the velocity potential and pressure field around the growing bubble. It was found that the relative pressure at the orifice reaches a maximum when the distance from the orifice to the bubble center becomes 1.5 times the equivalent radius of the bubble. This is taken to be the criterion for the cut-off of the gas supply to the bubble by closing off the neck between the orifice and the bubble. With the definitions of maximum bubble frequency ($f$) and the bubble volume ($V_b$) as given below, the bubble diameter, $d_b$ can be estimated by equation (31):

$$f = 13.4\, r_{orif.}^{-0.5} = \frac{G}{V_b} \tag{B.26}$$

$$\Rightarrow V_b = 0.075\, r_{orif.}^{1/2.}\, G \tag{B.27}$$

$$\Rightarrow d_b = 2 \left( \frac{3V_b}{4\pi} \right)^{1/3} \tag{B.28}$$

where $r_{orif}$ is the radius of the lance orifice in cm.

The bubble velocity, $U_b$, is also estimated using several methods, which are given below. Again, the average value found is used in the calculations for $k_l$.

1. The motion of gas bubbles in liquids is characterized by the following dimensionless parameters: Eotvos number, $N_{eo}$ (equation (B.29)), Morton number, $N_M$ (equation (B.30)), and Reynolds number, *Re*. From a study of the available data on the velocity of rise of bubbles and their shapes, a generalized correlation linking $N_{eo}$ and $N_M$ to *Re* was obtained and plotted by Grace [34] for Newtonian liquids. Thus, an approximate value of $U_b$ can be calculated from the *Re* obtained from this plot, which is shown in Figure B.1.

$$N_{eo} = \frac{g d_b^2 (\rho_l - \rho_b)}{\sigma_l} \tag{B.29}$$

$$N_M = \frac{g \mu_l^4}{\rho_l \sigma_l^3} \tag{B.30}$$

2. Assuming that the steady-state rising velocity of gas bubbles occurs when the buoyant force equals the drag force on the bubbles, Mandelson and Maneri [35] reported the following equation for bubbles with $d_b > 1.4$ mm:

$$U_b = \sqrt{\left( \frac{2\sigma_l g_c}{d_b \rho_l} + \frac{g_c d_b}{2} \right)} \tag{B.31}$$

where $g_c = 32.174$ is a unit conversion factor.

3. For $1000 < Re < 200{,}000$, $U_b$ for low-viscosity fluids can be estimated from Newton's law [36]

$$U_b = 1.75 \sqrt{\left( \frac{g d_b (\rho_l - \rho_g)}{\rho_l} \right)} \tag{B.32}$$

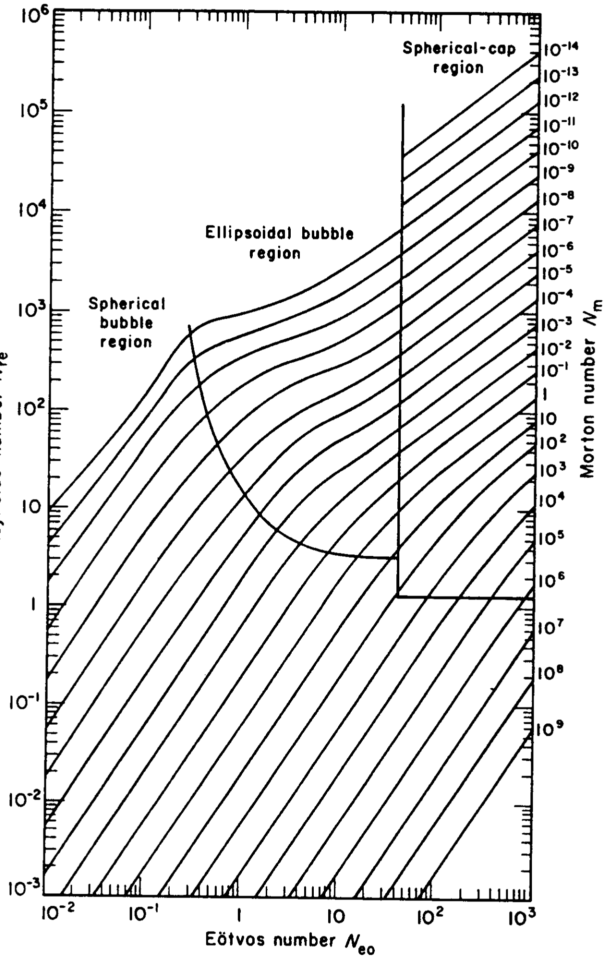

Figure B.1. Generalized correlation of Reynolds number versus Eotvos number for single bubbles in Newtonian liquids [34].

## B.4. Estimation of the Gas Phase Mass Transfer Coefficient for the Bubbles

Combining equations (B.4) and (B.6), the gas phase mass transfer coefficient for the bubbles is:

$$k_{g,b} = \frac{D_{X-g}}{\delta_{g,b}} \tag{B.33}$$

Since the gas used is argon, $D_{X\text{-}g}$ is really $D_{X\text{-}Ar}$ , which can be predicted by applying the Chapman-Enskog theory [37]. For ideal monatomic gases,

$$D_{X-Ar} = \frac{0.001858\ T^{3/2}}{P_{tot}\left(\sigma_{X-Ar}\right)^2 \Omega_{X-Ar}} \sqrt{\frac{1}{MW_X} + \frac{1}{MW_{Ar}}} \tag{B.34}$$

where $P_{tot}$ is the total gas pressure, $\sigma_{X\text{-}Ar} = 0.5(\sigma_X + \sigma_{Ar})$ is the collision diameter, and $\Omega_{X\text{-}Ar}$ the collision integral for an X-Ar mixture at the dimensionless temperature ($T^*$) for the Lennard-Jones potential. $\sigma_X$ and $\sigma_{Ar}$ are the collision cross sections for X and argon, respectively. In order to evaluate the collision integral, $(\varepsilon/\kappa_B)$ values must be calculated by the following equations:

$$\left(\frac{\varepsilon}{\kappa_B}\right)_{X-Ar} = \sqrt{\left(\frac{\varepsilon}{\kappa_B}\right)_{Ar}\left(\frac{\varepsilon}{\kappa_B}\right)_X} \tag{B.35}$$

$$\left(\frac{\varepsilon}{\kappa_B}\right)_X = 1.15\ T_b \qquad \left(\frac{\varepsilon}{\kappa_B}\right)_{Ar} = 1.92\ T_m \qquad \text{and} \tag{B.36}$$

$$T^* = \left(\frac{\kappa_B}{\varepsilon}\right)_{X-Ar} T \tag{B.37}$$

where $T_b$ and $T_m$ are boiling and melting points, respectively. Then, the collision integral can be obtained from plots of $\Omega_{X\text{-}Ar}$ vs. $T^*$ available in the literature [37].

The calculation of $\delta_{g,b}$ was outlined in section 3.1.3.2.

## B.5. Estimation of the Gas Phase Mass Transfer Coefficient for the Melt Surface

To model the mass transfer aided by thermal convection currents above the melt surface, McAdams [14] recommends the following equation for the laminar range (the calculated Grashof number was on the order of $10^5$) :

$$Nu = 0.54(Gr\,\mathrm{Pr})^{1/4} \tag{B.38}$$

Since $Pr$ and $Sc$ were found to be similar for argon at 1323 K, ($Pr \approx 0.7$ and $Sc \approx 1$), the thermal and mass transfer boundary layer thicknesses can be considered equal, which implies that $Sh = Nu$. This temperature was considered because it is the average gas temperature between the copper melt and the top plate, as will be explained later. For the case of an iron melt $Pr$ and $Sc$ were also similar at 1623 K ($Pr \approx 0.8$ and $Sc \approx 1$).

Thus,

$$Sh = \frac{k_{g,ms}L}{D_{X-Ar}} = 0.54(Gr\,\mathrm{Pr})^{1/4} = 0.54\left(\frac{L^3\rho_{Ar}^2 g\beta_{Ar}(T_{Ar,hot} - T_{Ar,cold})}{\mu_{Ar}^2}\frac{C_{p,Ar}\mu_{Ar}}{k_{Ar}}\right)^{1/4} \tag{B.39}$$

where $L$ is taken as 9/10 of the average diameter of the furnace interior, $C_{p,Ar}$ is the heat capacity of the gas, $k_{Ar}$ its thermal conductivity, $\beta_{Ar}$ its thermal coefficient of volume expansion, $\rho_{Ar}$ its density, and $\mu_{Ar}$ is its viscosity. All gas properties are taken at T = $0.5(T_{Ar,hot} - T_{Ar,\,cold})$. From this equation, the gas phase mass transfer coefficient for the melt surface ($k_{g,ms}$) can be readily calculated.

# Nomenclature

| | | |
|---|---|---|
| $A_b$ | Interfacial contact area between bubble and melt | (cm$^2$) |
| | or Area of bubble | (cm$^2$) |
| $A_{ms}$ | Area of melt surface | (cm$^2$) |
| $d_b$ | Bubble diameter | (cm) |
| $d_{orif.}$ | Diameter of orifice | (cm) |
| $G$ | Volumetric gas flow rate | (cm$^3$/sec) |
| $g$ | acceleration due to gravity | (981 cm/sec$^2$) |
| $\Delta G^o$ | Standard Gibbs free energy change | (J/mol) |
| $\Delta G^o_{\underline{x(\%)}\rightarrow x(l)}$ | Standard Gibbs energy for solution of X to 1 mass % solution in melt | (J/mol) |
| $\Delta G^o_{x(l)\rightarrow x(g)}$ | Standard Gibbs energy change for solute evaporation | (J/mol) |
| $\Delta G$ | Change of Gibbs free energy | (J/mol) |
| $f_x$ | Henrian activity coefficient | |
| $H$ | Height of the melt | (cm) |
| $h$ | Vertical distance between the bubble and bottom of the melt | (cm) |
| $K_b$ | Mass transfer coefficient to bubbles | (cm/sec) |
| $K_e$ | Overall evaporation coefficient | (cm/sec) |
| $k_e$ | Interface mass transfer coefficient | (cm/sec) |
| $k_g$ | Gas phase mass transfer coefficient | (cm/sec) |
| $k'_g$ | Normalized gas phase mass transfer coefficient | (cm/sec) |
| $k_l$ | Liquid phase mass transfer coefficient | (cm/sec) |
| $K_{ms}$ | Overall mass transfer coefficient for the melt surface | (cm/sec) |
| $M_x$ | Mass of the solute | (g) |
| $M_l$ | Mass of the melt | (g) |
| $MW_x$ | Molecular weight of the solute | (g/gmol) |
| $MW_l$ | Molecular weight of the melt | (g/mol) |
| $N_x$ | Overall molar flux of solute $X$ | (mol/cm$^2$sec) |
| $N_{x(c)}$ | Molar flux of solute $X$ in the interface | (mol/cm$^2$sec) |
| $N_{x(g)}$ | Molar flux of solute $X$ in gas phase | (mol/cm$^2$sec) |
| $N_{x(l)}$ | Molar flux of solute $X$ in liquid phase | (mol/cm$^2$sec) |
| $P$ | Pressure | (atm or Pa) |
| $P^o_x$ | Vapor pressure of solute | (atm or Pa) |
| $P_x$ | Partial pressure of solute | (atm or Pa) |
| $P^{eq}_x$ | Equilibrium partial pressure of solute | (atm or Pa) |
| $P^{exit}_x$ | Exit partial pressure of solute | (atm or Pa) |
| $Q$ | Molar gas flow rate | (mol/sec) |
| $R$ | Radius of bubble or | (cm) |
| | universal gas constant | (J/mol-K) |
| $T$ | Temperature | (K) |
| $t$ | time | (sec) |
| $U_t$ | Bubble rise velocity | (cm/sec) |
| $V_b$ | Volume of bubble | (cm$^3$) |
| $\rho_l$ | Density of melt | (g/cm$^3$) |

| | | |
|---|---|---|
| $\rho_x$ | Density of solute | (g/cm$^3$) |
| $\rho_g$ | Density of gas | (g/cm$^3$) |
| $\sigma_l$ | Surface tension of melt | (dyn/cm) |
| $\sigma_x$ | Surface tension of solute | (dyn/cm) |
| $\mu_g$ | Viscosity of solute | (g/cm sec) |
| $\mu_l$ | Viscosity of melt | (g/cm sec) |

# Bibliography

[1] Feizollahi, F., et. al., "Integrated Thermal Treatment System Study--Phase 1 Results", Idaho National Engineering Laboratory, Report # EGG-MS-11211, Contract # DE-AC07-761D01570, Idaho Falls (1994).

[2] Ozberk, E. and Guthrie, R.I.L, Mat. Sci. and Tech., 1, 12 (1985).

[3] Ohno, R., Met. Trans. B, 22B, 447 (1991).

[4] Ward, R.G, and Aurini, T.D., J. Iron and Steel Inst., 920 (Sept 1966).

[5] Ward, R., JISI, 201, 11 (1963).

[6] Ito, K., Kishimoto, M., and Mori, K., Tetsu to Hagane, 9, 1441 (1992).

[7] Barin, I., and Modigell, M., Erzmetall 39, 12 (1986), p. 618.

[8] Hino, M., Wang, S., Nagasaka, T., and Ban-Ya, S., ISIJ, 34, 491 (1994).

[9] Richardson, F.D., "Review Paper: Kinetics of Reactions Between Gases and Liquid Metal", Imperial College, London.

[10] Engh, T.A., *Principles of Metal Refining*, Oxford (1992).

[11] Higbie, R., Trans. Inst. Chem. Eng, 31, 365 (1935).

[12] Yim, P., "The Role of Surface Oxidation in the Break-Up of Laminar Liquid Metal Jets", Ph.D. Thesis, Dept. of Mechanical Eng., Massachusetts Institute of Technology, 1996.

[13] Drysdale, C.V., Geddes, A.E.M., et. al., "The Mechanical Properties of Fluids; A Collective Work", 2nd ed., Blackie & Son, Ltd., 1946.

[14] McAdams, W.H., *Heat Transmission*, 3rd ed., McGraw-Hill, New York (1954).

[15] *CRC Handbook of Chemistry and Physics*, 50th ed., (1970).

[16] Sigworth, G., and Elliott, J., Can. Met. Q., 13, 455 (1974).

[17] Sigworth, G., and Elliott, J., Metal Science, 8 (1974).

[18] Hultgren, R., Desai, P., Hawkins, D., Gleiser, M., and Kelley, K., "Selected Values of the Thermodynamic Properties of the Elements", ASM (1973).

[19] Kubaschewski, O, and Alcock, C.B., *Metallurgical Thermochemistry*, 5th ed., Pergamon (1979).

[20] Turkdogan, E.T., *Physical Chemistry of High Temperature Technology*, Academic Press (1980).

[21] HSC Chemistry (software program), ver. 2.03, Outokumpu Research Oy, Finland (1994).

[22] Li, L., Tu, S., and Janke, D., Steel Research, 66, 188 (1995).

[23] Ozberk, E. and Guthrie, R.I.L., Met. Trans. B, 17B, 87 (1986).

[24] Harris, Met. Trans. B, 15B, 251 (1984).

[25] Harris, R., Can. Met. Q., 27, 169 (1988).

[26] Haynes, B.S., "Soot and Hydrocarbons in Combustion", in *Fossil Fuel Combustion: A Source Book*, ed. by W. Bartok and A. Sarofim, Wiley & Sons, New York (1991).

[27] Friedlander, S. K., *Smoke, Dust, and Haze*, Wiley & Sons (1977).

[28] Hinds, W. C., *Aerosol Technology: Properties, Behavior, and Measurement of Airborne Particles*, Wiley & Sons, (1982).

[29] Pelton, A., and Bale, C., Met. Trans A, 17A, 1211 (1986).

[30] Tyn, M.T. and Calus, W.F, J. Chem. Data, 20, 106 (1975).

[31] Hayduk, W. and Minhas, B.S., Can. J. Chem. Eng., 60, 295 (1982).
[32] Sano and Mori, Trans. JIM, 17, 344 (1976).
[33] Wraith, K., and Kakutani, T., Chem. Eng. Sci, 29, 1 (1974).
[34] Grace, J., Trans. Inst. Chem. Eng, 51, 116 (1973).
[35] Maneri, C.C., and Mendelson, H.D., AIChE J., **14**, 295 (1968).
[36] McCabe, W., Smith, J., and Harriott, P., *Unit Operations of Chemical Engineering*, 4th ed., McGraw-Hill (1985).
[37] Geiger, G., and Poirier, D., *Transport Phenomena in Metallurgy*, Addison-Wesley (1973).